Defense Nuclear Agency
Alexandria, VA 22310-3398

DNA-TR-89-6

Inviscid Dynamics of Unstable Shear Layers

A. Kuhl, et al.
R&D Associates
P.O. Box 9695
Marina del Rey, CA 90295

April 1990

Technical Report

CONTRACT No. DNA 001-88-C-0046

Destroy this report when it is no longer needed. Do not return to sender.

PLEASE NOTIFY THE DEFENSE NUCLEAR AGENCY, ATTN: CSTI, 6801 TELEGRAPH ROAD, ALEXANDRIA, VA 22310-3398, IF YOUR ADDRESS IS INCORRECT, IF YOU WISH IT DELETED FROM THE DISTRIBUTION LIST, OR IF THE ADDRESSEE IS NO LONGER EMPLOYED BY YOUR ORGANIZATION.

Director
Defense Nuclear Agency
ATTN: TITL
Washington, DC 20305-1000

Director
Defense Nuclear Agency
ATTN: TITL
Washington, DC 20305-1000

REPORT DOCUMENTATION PAGE

1a REPORT SECURITY CLASSIFICATION UNCLASSIFIED	1b. RESTRICTIVE MARKINGS
2a. SECURITY CLASSIFICATION AUTHORITY N/A since Unclassified	3. DISTRIBUTION/AVAILABILITY OF REPORT Approved for public release: distribution is unlimited.
2b DECLASSIFICATION/DOWNGRADING SCHEDULE N/A since Unclassified	
4 PERFORMING ORGANIZATION REPORT NUMBER(S) RDA-TR-161604-006	5. MONITORING ORGANIZATION REPORT NUMBER(S) DNA-TR-89-6
6a. NAME OF PERFORMING ORGANIZATION R&D Associates 6b. OFFICE SYMBOL (If applicable)	7a. NAME OF MONITORING ORGANIZATION Defense Nuclear Agency
6c ADDRESS (City, State, and ZIP Code) P.O. Box 9695 Marina del Rey, CA 90295	7b. ADDRESS (City, State, and ZIP Code) 6801 Telegraph Road Alexandria, VA 22310-3398
8a NAME OF FUNDING/SPONSORING ORGANIZATION 8b. OFFICE SYMBOL SPSP/ Castleberry	9. PROCUREMENT INSTRUMENT IDENTIFICATION NUMBER DNA 001-88-C-0046
8c. ADDRESS (City, State, and ZIP Code)	10. SOURCE OF FUNDING NUMBERS

PROGRAM ELEMENT NO.	PROJECT NO.	TASK NO.	WORK UNIT ACCESSION NO
61715H	RD	RC	DH880046

11 TITLE (Include Security Classification)
Inviscid Dynamics of Unstable Shear Layers

12 PERSONAL AUTHOR(S)
Kuhl, A.; Chien, K. Y.; Ferguson, R. E.; Glaz, H. M.; Colella, P.

13a TYPE OF REPORT	13b. TIME COVERED	14. DATE OF REPORT (Year, Month, Day)	15 PAGE COUNT
Technical	FROM 870801 TO 880801	900401	76

16 SUPPLEMENTARY NOTATION
This work was sponsored by the Defense Nuclear Agency under RDT&E RMC Code B4632D RD RC 00001 DFPR 1900A 25904D.

17 COSATI CODES			18. SUBJECT TERMS (Continue on reverse if necessary and identify by block number)
FIELD	GROUP	SUB-GROUP	
20	4		Free Shear Layers; Mean-flow Profiles; Wall Boundary Layers; Fluctuating Flow Profiles; Wall Jets
20	4		

19 ABSTRACT (Continue on reverse if necessary and identify by block number)

Numerical simulations are described for three idealized shear layer problems typical of shock reflection flow fields: free shear layers (corresponding to a slip line emanating from a triple point), a wall shear layer (approximating a boundary layer behind a shock), and a wall jet (similar to those found in precursor and double-Mach-stem flows). The dynamic evolution of the shear layers was followed by means of numerical solutions of the inviscid conservation laws of gasdynamics. The inviscid shear layer discontinuity was de-singularized by initializing the flowfield with a Tanh(y) velocity profile that, in effect, allows one to resolve the shear layer on the computational mesh. The inflow velocity profile was then perturbed with the fundamental frequency (from linear

20 DISTRIBUTION/AVAILABILITY OF ABSTRACT	21. ABSTRACT SECURITY CLASSIFICATION	
☐ UNCLASSIFIED/UNLIMITED ■ SAME AS RPT ☐ DTIC USERS	UNCLASSIFIED	
22a. NAME OF RESPONSIBLE INDIVIDUAL Bennie F. Maddox	22b. TELEPHONE (Include Area Code) (703) 325-7042	22c OFFICE SYMBOL DNA/CSTI

19. ABSTRACT (Continued)

stability analysis) and its subharmonics. The macroscopic features of the calculations (e.g., the formation and growth of large-scale rotational structures, the visual spreading rates, and the mean flow profiles) agree quantitatively with the available experimental data. The fluctuating flow components agree qualitatively (e.g., the peak velocity fluctuations can be 1.5 to 2 times larger than the data, because of the two-dimensional flow approximation). These calculations demonstrate that the fluctuating, time-dependent flow variations observed in such problems are caused by the dynamic evolution of unstable shear layers, and that the dynamics is dominated by inviscid effects for such large-Reynolds-number flows.

PREFACE

The authors would like to thank Professor Anatol Roshko (California Institute of Technology) and Dr. Heinz Reichenbach (Ernst Mach Institute, FRG) for supplying the photographs used in Figures 4 and 8, respectively. Lively discussions with Dr. Harold Mirels (Aerospace Corp.) stimulated the investigation of the mean and fluctuating flow profiles. Finally, we would like to thank Ms. Vivian Fox (RDA) for her diligent typing of the manuscript.

CONVERSION TABLE

Conversion factors for U.S. customary
to metric (SI) units of measurement

To Convert From	To	Multiply By
angstrom	meters (m)	1.000 000 X E-10
atmosphere	kilo pascal (kPa)	1.013 25 X E+2
bar	kilo pascal (kPa)	1.000 000 X E+2
barn	meter^2 (m^2)	1.000 000 X E-28
British Thermal unit (thermochemical)	joule (J)	1.054 350 X E+3
calorie (thermochemical)	joule (J)	4.184 000
cal (thermochemical)/cm^2	mega joule/m^2(MJ/m^2)	4.184 000 X E-2
curie	giga becquerel (GBq)*	3.700 000 X E+1
degree (angle)	radian (rad)	1.745 329 X E-2
degree Fahrenheit	degree kelvin (K)	T_K=(t°f + 459.67) 1.8
electron volt	joule (J)	1.602 19 X E-19
erg	joule (J)	1.000 000 X E-7
erg/second	watt (W)	1.000 000 X E-7
foot	meter (m)	3.048 000 X E-1
foot-pound-force	joule (J)	1.355 818
gallon (U.S. liquid)	meter^3 (m^3)	3.785 412 X E-3
inch	meter (m)	2.540 000 X E-2
jerk	joule (J)	1.000 000 X E+9
joule/kilogram (J/Kg) (radiation dose absorbed)	Gray (Gy)**	1.000 000
kilotons	terajoules	4.183
kip (1000 lbf)	newton (N)	4.448 222 X E+3
kip/inch^2 (ksi)	kilo pascal (kPa)	6.894 757 X E+3
ktap	newton-second/m^2 (N-s/m^2)	1.000 000 X E+2
micron	meter (m)	1.000 000 X E-6
mil	meter (m)	2.540 000 X E-5
mile (international)	meter (m)	1.609 344 X E+3
ounce	kilogram (kg)	2.834 952 X E-2
pound-force (lbf avoirdupois)	newton (N)	4.448 222
pound-force inch	newton-Ometer (N.m)	1.129 848 X E-1
pound-force/inch	newton/meter (N/m)	1.751 268 X E+2
pound-force/foot^2	kilo pascal (kPa)	4.788 026 X E-2
pound-force/inch^2 (PSI)	kilo pascal (kPa)	6.894 757
pound-mass (lbm avoirdupois)	kilogram (kg)	4.535 924 X E-1
pound-mass-foot^2 (moment of inertia)	kilogram-meter2 (kg.m^2)	4.214 011 X E-2
pound-mass/foot^3	kilogram/meter3 (kg/m^3)	1.601 846 X E+1
rad (radiation dose absorbed)	Gray (Gy)**	1.000 000 X E-2
roentgen	coulomb/kilogram (C/kg)	2.579 760 X E-4
shake	second (s)	1.000 000 X E-8
slug	kilogram (kg)	1.459 390 X E+1
torr (mm Hg, 0°C)	kilo pascal (kPa)	1.333 22 X E-1

*The becquerel (Bq) is the SI unit of radioactivity; Bp = 1 event/s.

**The Gray (Gy) is the SI unit of absorbed radiation.

TABLE OF CONTENTS

Section		Page
	PREFACE	iii
	CONVERSION TABLE	iv
	FIGURES	vi
	TABLES	ix
1	INTRODUCTION	1
2	FORMULATION	3
	2.1 GOVERNING EQUATIONS.	3
	2.2 NUMERICAL METHODS.	3
	2.3 TIME-STEP CONTROL.	4
	2.4 INTERFACE DYNAMICS.	4
	2.5 INITIAL CONDITIONS.	5
	2.6 BOUNDARY CONDITIONS.	7
3	FREE SHEAR LAYER CALCULATIONS	8
	3.1 FORCED SHEAR LAYERS.	8
	3.2 SPREADING SHEAR LAYER.	10
	3.3 SUMMARY.	24
4	WALL SHEAR LAYER CALCULATIONS	25
	4.1 SHOCK TUBE EXPERIMENT.	25
	4.2 FORMULATION.	25
	4.3 RESULTS.	29
	4.4 TRIPPED FLAT PLATE CASE.	41
	4.5 SUMMARY.	46
5	WALL JET CALCULATION	48
	5.1 FORMULATION.	48
	5.2 RESULTS.	49
	5.3 SUMMARY.	58
6	CONCLUSIONS AND GENERALIZATIONS	59
7	LIST OF REFERENCES	62

FIGURES

Figures		Page
1	Schematic of the free shear layer calculations: (a) computational grid; (b) Tanh(y) streamwise velocity profile; (c) Tanh(y) density profile ...	6
2	Numerical simulation of the forced shear layer experiments of Ho and Huang (λ = 0.31,r = 0.53, ϵ = 0.01). Material interface plots: (a) Mode I response (ω_1 only); (b) Mode II response ($\omega_1 + \omega_2$); (c) Mode III response ($\omega_1 + \omega_3$); (d) Mode IV response ($\omega_1 + \omega_4$)	9
3	Numerical simulation of the spreading shear layer experiment of Brown and Roshko (λ = 0.451, r = 0.378, ρ_2/ρ_1 = 7)	12
4	Flowfield of the spreading shear layer calculation at t = 5013: (a) material interface; (b) shadowgraph from the Brown and Roshko experiment (Figure 3); (c) density contours; (d) vorticity contours (solid lines denote negative values and dashed lines correspond to positive values that are baroclinicly generated); (e) overpressure contours (solid lines denote positive values)	17
5	Flow field along the center line (y = 0.5) of the spreading shear layer calculation at t = 5013: (a) density; (b) streamwise velocity; (c) overpressure; (d) dynamic pressure	18
6	Mean-flow profiles of the spreading shear layer calculation: (a) streamwise velocity profiles; (b) density profiles. Symbols □, ○, and Δ denote stations at x = −100, 200, and 400, respectively. Shaded area denotes the experimental data band from Brown and Roshko (1974)	20
7	Time-averaged fluctuating flow profiles from the spreading shear layer calculations: (a) streamwise velocity: (b) transverse velocity: (c) shear stress: (d) density (shaded region corresonds to the experimental data band of Konrad [1977]); (e) pressure. Symbols □, ○, and Δ denote stations at x = 100, 200, and 400, respectively. Dashed curves denote the data of Oster and Wygnanski (1982) for an unforced shear layer (their Region 1).	21
8	Tracing of a shadow-schlieren photograph of the waves induced by the boundary layer behind a Mach M_s = 1.7 shock wave. Acoustic waves radiate from the foot of the shock. Density structures are formed in the wall boundary layer (Courtesy of Dr. H. Reichenbach, Ernst Mach Institute FRG.)	26
9	Schematic of the shock tube wall-shear-layer calculation: (a) and (b) shock wave and boundary layer in stationary and shock-fixed coordinates, respectively; (c) computational grid: (d), (e) and (f) wall shear layer profiles of velocity energy and pressure, respectively	28

FIGURES (Continued)

Figures		Page
10	Calculated flow field of the development of a wall shear layer behind a shock (t = 3075): (a) Overpressure contours showing the radiation of acoustic waves from the foot of the shock (x=y=o): (b)-(f) material interface plots demonstrating the rollup of the shear layer	31
11	Expanded view of the flowfield from Figure 10 near the end of the grid: (a) material interface, showing the rollup of the layer; (b) density contours; (c) overpressure contours (solid lines correspond to positive values); (d) vorticity contours	32
12	Flow field along the wall of the shock tube wall-shear-layer calculation at t = 3075: (a) density; (b) streamwise velocity; (c) overpressure; (d) dynamic pressure	33
13	Mean-flow profiles of the shock tube wall-shear-layer calculation: (a) streamwise velocity profile; (b) density profile. (Symbols □, ○, Δ, and + denote stations at x = 400, 600, 800 and 950, respectively.) ...	34
14	Time-averaged fluctuating flow profiles from the shock tube wall-shear-layer calculation: (a) streamwise velocity; (b) transverse velocity; (c) shear stress; (d) density; (e) pressure. (Symbols □, ○, Δ and + denote stations at x = 400, 600, 800 and 950, respectively.)	36
15	Mean-flow velocity profiles of the shock tube wall-shear-layer calculation, demonstrating the Law of the Wall behavior (straight lines) and the wake region (dashed curve, Eq. 34) of the profiles. (Symbols □, ○, Δ and + denote stations at x = 400, 600, 800 and 950, respectively.) The double-chain-dashed curve denotes the n = 7 power function profile for a flat plate. The triple-chain-dashed curve represents a boundary layer profile with an adverse pressure gradient, as measured by Schubauer and Spangenberg (1960)	39
16	Flow field of the tripped flat plate calculation (t = 3617): (a), (b), (c) are material interface plots showing the rollup of the layer; (d), (e) and (f) represent contour plots of density, overpressure and vorticity, respectively	42
17	Mean-flow velocity profiles of the tripped flat plate case. Symbols □, ○, Δ, and ◇ denote calculation stations at x = 400, 600, 800 and 950, respectively. The chain-dashed curve represents the n = 7 power function profile (Eq. 41). The dashed curves denote the Coles function fits of the tripped flat plate data of Wieghardt and Tillmann (1944); symbols ● and ◆ denote data stations at x = 79 cm (profile 1400–10) and x = 499 cm (profile 1400-26), respectively	44
18	Time-average fluctuating flow profiles from the tripped flat plate calculation: (a) streamwise velocity; (b) transverse velocity; (c) shear stress: (Symbols □, ○, Δ, and + denote stations at x = 400, 600, 800 and 950,respectively). Dashed curves represent the data of Klebanoff (1955)	45

FIGURES (Concluded)

Figures		Page
19	Schematic of the wall jet calculation.	48
20	Numerical simulation of a wall jet (λ = -1, r = ∞, λ_ρ = 0). The figures depict the evolution of the material interfaces over one period of the flow. Vortices forming on the free shear layer are labeled sequentially with cardinal numbers, while those forming on the wall layer are denoted by capital letters	50
21	Flow field of the wall jet calculation at t = 1722: (a) material interfaces; (b) vorticity contours (solid lines correspond to positive values, while dashed lines denote negative values); (c) overpressure contours (solid lines correspond to positive values)	55
22	Mean-flow velocity profiles of the wall jet calculation: (a) streamwise component; (b) transverse component. (Symbols □ and ○ denote stations at x = 85 and 170, respectively.)	56
23	Time-averaged fluctuating flow profiles from the wall jet calculation: (a) streamwise velocity; (b) transverse velocity; (c) shear stress. (Symbols □ and ○ denote stations at x = 85 and 170, respectively.)	57

TABLES

Table		Page
1	Comparison of Peak Fluctuating Quantities	23
2	Shock Conditions (M_S = 1.70, γ = 1.4)	27
3	Boundary Layer Parameters for the Shock Tube Case	38
4	Boundary Layer Parameters for the Tripped Flat Plate Case	46

SECTION 1

INTRODUCTION

Flow fields associated with shock reflections often times contain embedded shear layers. Typical examples are slip lines from triple points, wall boundary layers, and wall jets associated with double-Mach reflections. Because the Reynolds numbers associated with these flows are very large (typically 10% per centimeter or even larger), such shear layers are essentially inviscid tangential velocity discontinuities.

It has been known for more than 100 years that certain types of subsonic shear layers are inviscidly unstable. Lord Rayleigh (1880) proved a necessary condition and later Tollmien (1935) proved a sufficient condition for the unstable growth of perturbations in shear layers. This is summarized by the Rayleigh-Tollmien Inflection Point Theorem which states that: solutions of the inviscid momentum equation are unstable to small perturbations if (and only if) the initial shear layer profile contains an inflection point (Schlichting, 1968).

The late-time consequence of such flow instabilities is that perturbed shear layers eventually roll up into large-scale vortex structures. Today, there is ample experimental evidence that shear layers evolve according to this mechanism. One of the most famous examples is the experimental work of Brown and Roshko (1974) which demonstrates that shear layers roll up into organized rotational structures,[1] and that the largest-scale structures are essentially independent of the flow Reynolds number (although the micro-scale mixing within the large structures remains Reynolds number dependent). About the same time, Winant and Browand (1974) demonstrated that the growth of the mixing layer is governed by the pairing mechanism of these vortical structures. Many other examples of coherent vortex behavior may be found in M. Van Dyke's *Album of Fluid Motion* (1982).

Recently, Monkewitz and Huerre (1982) performed a linear spatial stability analysis of the inviscid momentum equation, and established the most amplified frequency (w_1) and its *nth* subharmonics ($w_n = w_1/n$) for a shear layer with a Tanh(y) velocity profile. Ho and Huang (1982) confirmed experimentally the effectiveness of these subharmonic forcing frequencies in modifying the dynamics and spreading rate of the shear layer. Our calculations will utilize both results.

Many shear layer computations involving discretizations of the Navier-Stokes equations are available. These include finite-difference methods (e.g., Corcos and Sherman [1984], McInville et al. [1985], and Davis and Moore [1985]), spectral methods (Riley and Metcalfe, 1980), and vortex methods (e.g., Ashurst [1979], Leonard [1980], and Ghoniem, Chorin and Oppenheim [1982]), Oppenheim [1986]). These calculations succeed in resolving small-scale flowfield structures and are of high quality. However, modeling of the viscous terms imposes computational inefficiencies because viscous length scales

1. Apparently Brown and Roshko were not the first to observe such effects. Michel (1932) photographed organized rotational structures in an acoustically perturbed free shear layer.

must be resolved on the mesh. This either severely restricts the time step or leads to implicit time differencing and resultant numerical diffusion. The random vortex method (Chorin [1973] and [1986]) avoids these problems at the expense of introducing a statistical error, and the limitation that the flow must be incompressible.

Described here is an alternative, large-Reynolds-number approach[2] that is based on the nonsteady solution of the inviscid conservation laws of gas dynamics. In contrast with the vortex methods, there is no large-Mach-number limit with this approach and the baroclinic generation of vorticity is automatically included. In contrast with the implicit finite difference solutions of the Navier-Stokes equations, the present approach focuses on an accurate, nondiffusive evaluation of the convective derivatives which seem to control the dynamics of the large-scale structures. Hence, molecular diffusion effects (i.e., diffusion of vorticity and passive scalars across stream-lines) are neglected during the time-scale of the calculation. The disadvantages of this inviscid approach are that calculations of small-Mach-number flows are expensive, and shear at wall boundaries must be programmed into the calculation as an initial condition.

Numerical results were obtained by means of an explicit second-order Godunov algorithm (Colella and Glaz [1985a]) which gives nondiffusive solutions for gas dynamics. This algorithm has produced accurate laminar solutions to a variety of blast wave reflection problems (Colella et al. [1985b] and Glaz et al. [1985]). Often the shear layers embedded in these flows roll up into large-scale vortex structures (Kuhl et al. 1987). One of the questions explored here is: How accurate are these nonsmooth (i.e., fluctuating) portions of the flow, as predicted by the numerical solutions of the inviscid conservation laws? Illustrative calculations are presented for three classes of problems typical of shock reflection flow fields: free shear layers, wall boundary layers and a wall jet. By design, they are limited to nonsteady calculations of two-dimensional shear layers that are steady in the mean or time-averaged sense. The objectives of this work were to demonstrate that the dynamic evolution of these "steady" shear layers can be predicted by a nonsteady solution of the inviscid conservation law of gas dynamics, and also to evaluate the accuracy of such solutions by comparing the results with experimental data.

The numerical formulation of the calculations is described in Section 2. A detailed discussion of the results for the free shear layer, wall shear layer and wall jet calculations are presented in Sections 3, 4 and 5, respectively. Conclusions and generalizations drawn from these results are offered in Section 6.

2. This inviscid approach is also being used with the "Flux-Corrected Transport" codes (Grinstein et al., 1986) and in the inviscid vortex dynamics calculations of Inoue (1985, 1987).

SECTION 2

FORMULATION

2.1 GOVERNING EQUATIONS.

The time-dependent flow field is governed by the conservation laws for mass, momentum and total energy. Considered here is an inviscid gas dynamics approximation valid for large Reynolds number flows; hence, molecular viscosity and heat conduction, as well as gravitational forces are neglected. For a computational volume V with boundary jV, the equations of gas dynamics may be written in strong conservation form as:

$$\frac{\partial}{\partial t}\int_V W dV = -\oint_{\partial V} W\underline{u}\cdot d\underline{A} + \oint_{\partial v} \underline{\underline{\sigma}}\cdot d\underline{A} \quad (1)$$

where

$$W \equiv \begin{Bmatrix} \rho \\ \rho\underline{u} \\ \rho E_T \end{Bmatrix} \quad \underline{\underline{\sigma}} \equiv \begin{Bmatrix} o \\ -\underline{n}p \\ -\underline{n}p\underline{u} \end{Bmatrix}$$

$$E_T \equiv e + 1/2\ \underline{u}\cdot\underline{u}$$

$$p = (\gamma - 1)\ \rho e$$

In the above, $\underline{u}$ denotes the gas velocity, while p, ρ and $\bar{e}$ represent the gas pressure, density and internal energy, respectively. For convenience, the specific heat ratio is assumed here to be constant: $\gamma = 1.4$.

Eq. (1) may be formally integrated over a time $\Delta t = t^{n+1} - t^n$ to evaluate new cell-averaged values of the conserved variables W:

$$(WV)^{n+1} = (WV)^n - \int_o^{\Delta t}\oint_{\partial V} W\,\underline{u}\cdot d\underline{A}\,dt + \int_o^{\Delta t}\oint_{\partial V} \underline{\underline{\sigma}}\cdot d\underline{A}\,dt \quad (2)$$

The objective of a numerical algorithm is to evaluate the above integrals as accurately as possible.

2.2 NUMERICAL METHODS.

The computations are two-dimensional and performed in Cartesian coordinates. A rectangular mesh, aligned with the mean flow (i.e., the upstream splitter plate or bottom wall), is used. Variable mesh spacing is utilized in order to concentrate the computational effort in regions of interest and minimize any adverse effects of the artificial outflow boundary conditions. All computations are operator split. The temporal approximation of, say, an x sweep for Eq. (2) may be written in conservation form:

$$(WV)_{i\,j}^{n+1} = (WV)_{i\,j}^{n} - \left[F_{i+1/2,j}^{n+1/2} - F_{i-1/2,j}^{n+1/2}\right] + \left[P_{i+1/1/2,j}^{n+1/2} - P_{i-1/2,j}^{n+1/2}\right] \quad (3)$$

where the cell interface fluxes, F, and pressure-work terms, P, are given by:

$$F^{n+1/2}_{i+1/2,j}$$

$$= W^{n+1/2}_{i+1/2,j}\ \underline{u}^{n+1/2}_{i+1/2,j} \cdot \underline{A}_{i+1/2,j}\ \Delta t$$

$$P^{n+1/2}_{i+1/2,j} = \underline{\underline{\sigma}}^{n+1/2}_{i+1/2,j} \cdot \underline{A}_{i+1/2,J}\ \Delta t$$

$$\underline{A}_{i+1/2,j} = \underline{A}(\underline{x}_{i+1/2,j})$$

These interface fluxes and pressures are evaluated by the second-order Godunov technique (Colella and Glaz, 1985). First, piecewise-linear subgrid interpolant functions are used to define the environment everywhere within the computational cell at the initial time level, t^n. Second, the slopes of the interpolants are limited to maintain monotonicity of the solution. Starting at each cell boundary (e.g., i+1/2,j) at time $t^{n+1/2}$, the three gas dynamic characteristics are traced back to time level t^n where the Riemann variables are evaluated. Beginning with these values, the Riemann equations are then integrated along the characteristic curves to evaluate the flow field at the cell interface at the half time level $t^{n+1/2}$. Finally, the interface fluxes and pressures based on this solution are used in the conservative difference scheme of Eq. (3) to update the cell-averaged values of mass, momentum and energy.

2.3 TIME-STEP CONTROL.

The above represents an explicit scheme for solving a system of hyperbolic conservation laws, hence the time step is limited by the Courant-Friedrichs-Lewy condition:

$$\Delta t = C\Delta x/(a + |u|) \qquad (4)$$

where Δx denotes the mesh spacing, and $a = \sqrt{\gamma p/\rho}$ represents the local sound speed. The Courant number used in these calculations was C = 0.95.

This numerical method is most appropriate for nonsteady compressible flows of gas dynamics. It can also be used to provide inviscid solutions of nonsteady small Mach-number flows, but one must either compromise the computational efficiency or violate similitude in Mach number. For example, the Mach numbers typical of many shear layer experiments are on the order of M ~ 0.01, and it would take approximately one hundred time steps to convect a fluid particle through one computational cell with an explicit scheme. Note that there is nothing theoretically wrong with this approach. In fact, it can be viewed as a very accurate (albeit expensive) time integration scheme. To save computing costs, however, the sound speed in such small Mach-number problems was modified so that flow Mach number was typically M ~ 0.2. In such cases the density and velocity ratios across the shear layer were preserved, but similitude in Mach number was violated. For low speed flows, however, compressibility or Mach number effects are generally not important, and this Mach number compromise was found to be worth the improvement in computational efficiency.

2.4 INTERFACE DYNAMICS.

To clearly illustrate the dynamics of shear layers, it was necessary to accurately track material interfaces (or lines in 2-D). Such lines were discretized by a series of connected points $\underline{x}_k(t)$ which moved with the local material velocity, i.e.:

$$\frac{d}{dt}\underline{x}_k = \underline{u}(\underline{x}_k) \qquad k = 1, 2 \ldots\ldots K \qquad (5)$$

The initial spacing between points was assumed to be one-tenth the computational

cell size. The location of each material point was updated according to a finite difference approximation to Eq. (5), namely:

$$\underline{x}_k^{n+1/2} = \underline{x}_k^n + \underline{u}^n(\underline{x}_k(t^n))\Delta t/2$$
$$\underline{x}_k^{n+1} = \underline{x}_k^{n+1/2} + \underline{u}^n(\underline{x}_k(t^{n+1/2}))\Delta t/2 \quad (6)$$

where $\underline{u}^n$ represents a velocity that is linearly interpolated from the four nearest computational cells surrounding point $\underline{x}_k$. Note that for both steps in Eq. (6), the velocity field is based on time t^n (because the numerical algorithm is operator split); only the interpolation point changes: i.e., $\underline{x}_k^n$ versus $\underline{x}_k^{n+1/2}$. When the distance between neighboring points $||\underline{x}_k - \underline{x}_{k+1}||$ exceeded twice the initial spacing, a new marker was inserted at their midpoint to maintain numerical resolution. The number of marker points was allowed to increase to a maximum of 75,000 (which would double the computational time), after which no further points would be inserted over the last 60 percent of the grid. Marker points that passed outside the fine-grid region were deleted, and then the entire system was renumbered.

2.5 INITIAL CONDITIONS.

The calculations were performed on a two-dimensional Cartesian grid. A typical example for the free shear layer problems is shown in Figure 1. A fine-zoned region, covering the domain:

$$0 \leq x \leq X_F$$
$$-Y_F \leq y \leq Y_F$$

was centered on the centerline of the layer. An expanding grid was used (above, below, and to the right of the fine-grid region) to place the boundaries of the mesh far away from the layer and thereby minimize any boundary influences on the free shear layer development.

The shear layers were modeled or approximated by a Tanh(y) velocity profile. This approach not only allows one to resolve the shear layer on the computational grid, it also removes what would otherwise be an inviscid velocity discontinuity—thereby regularizing the inviscid problem. In effect, viscosity is allowed to act on the flow for a long enough time to spread the shear over a finite thickness of fluid; this solution is then mapped onto the grid, and thereafter the effects of molecular viscosity are eliminated.

The following Tanh(y) velocity profile was used to initialize the flowfield:

$$u(x, y, o) = f(y)$$
$$v(x, y, o) = o \quad (7)$$

where

$$f(y) = U_m[1 + \lambda\ Tanh\ (\ 2y/\delta - y_o\ )] \quad (8)$$

$$U_m = (U_1 + U_2)\ /\ 2 \quad (9)$$

$$\lambda = (U_1 - U_2)\ /\ (U_1 + U_2) \quad (10)$$

In the above, U_1 and U_2 denote the free stream velocity at $y = \pm\infty$ respectively; U_m represents the mean flow velocity; λ is the shear parameter; y_o denotes the centerline of the layer; while δ is the maximum-slope thickness of the layer, typically 2 cells. In most of the results to be presented, the lengths have been normalized by $\delta/2$.

In some free shear layer problems, the density of the two streams is different. In these cases a Tanh(y) profile was also used to approximate the density distribution

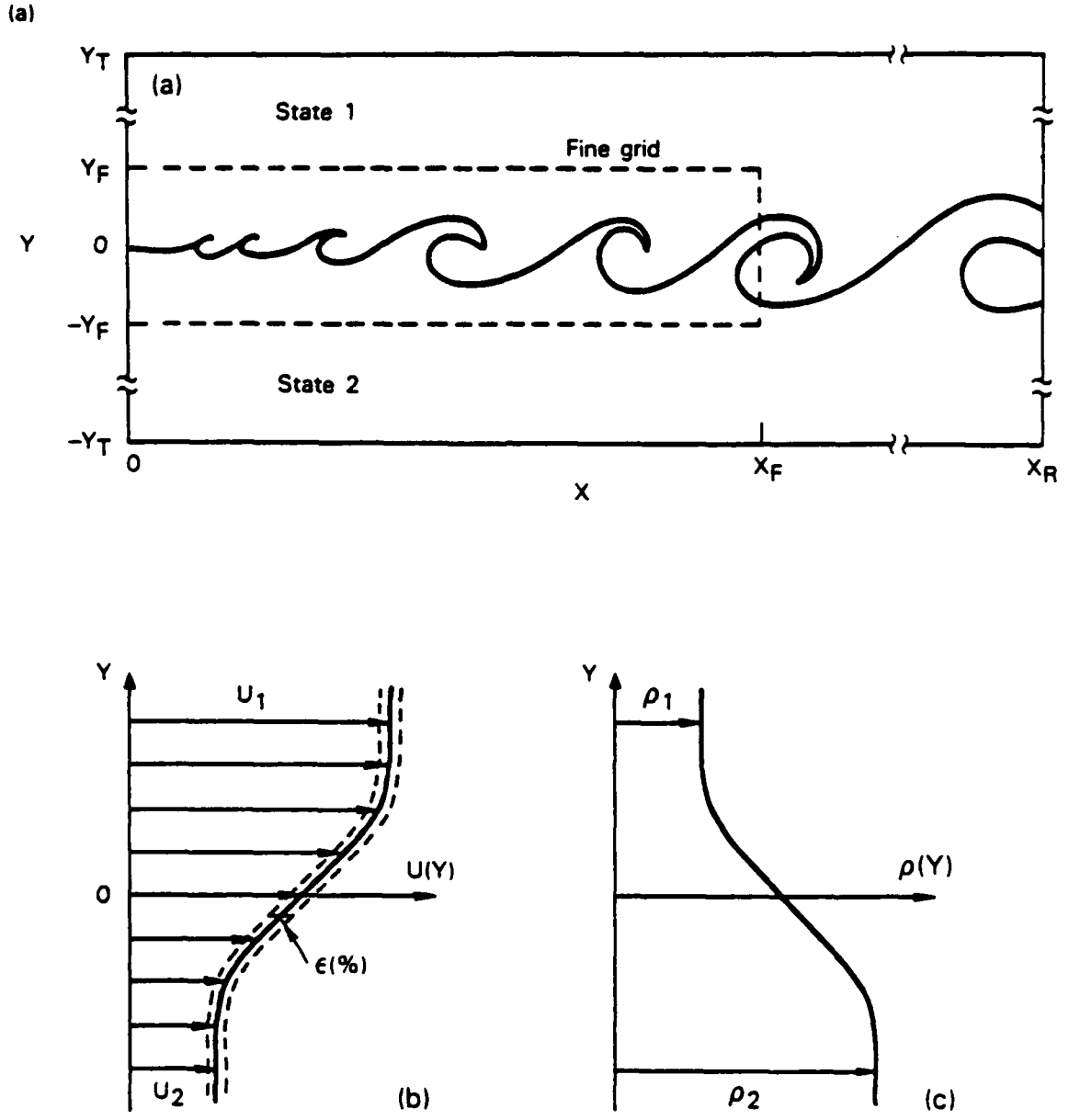

Figure 1. Schematic of the free shear layer calculations: (a) computational grid; (b) Tanh(y) streamwise velocity profile; (c) Tanh(y) density profile.

across the molecular diffusion region, namely:

$$\rho(x, y, o) = h(y) \tag{11}$$

where

$$h(y) = \rho_m [1 + \lambda \rho \ Tanh \ (2y/\delta - y_o)] \tag{12}$$

$$\rho_m = (\rho_1 + \rho_2) \ / \ 2 \tag{13}$$

$$\lambda\rho = (\rho_1 - \rho_2) \ / \ (\rho_1 + \rho_2) \tag{14}$$

In the above ρ_1 and ρ_2 represent the free stream densities at $y = \pm \infty$, respectively; ρ_m denotes the mean density of the layer; and λ_ρ is the density parameter.

2.6 BOUNDARY CONDITIONS.

The left boundary of the mesh was driven by the same Tanh(y) profiles but with a sinusoidal time perturbation on the streamwise velocity component:

$$u(o, y, t) = u(x, y, o) \cdot g(t)$$

$$v(o, y, t) = o \tag{15}$$

$$\rho(o, y, t) = h(y) \tag{16}$$

where

$$g(t) = 1 + \sum_{n=1}^{N} \epsilon_n \sin \omega_n t \tag{17}$$

The perturbation frequencies (ω_n) and amplitudes (ϵ_n) were taken from the linear stability analysis for Tanh(y) shear layers of Monkewitz and Huerre (1982):

$$\omega_1 = 0.219 \text{ and } \omega_n = \omega_1/n$$

$$\epsilon_1 = 0.01, \ \epsilon_2 = 0.75\epsilon_1,$$

$$\epsilon_3 = 0.55\epsilon_1, \ \epsilon_4 = 0.44\epsilon_1, \tag{18}$$

$$\text{and } \epsilon_n = 1.7 \ \epsilon_1/n \text{ for } n \geq 5 \tag{19}$$

From the above, that the maximum perturbation amplitude used in this study was one percent ($\epsilon_1 = 0.01$). Note that the above disturbances can be viewed as modeling the spectrum of perturbations which arise naturally in the flow (e.g., molecular fluctuations which are amplified to a macroscopic scale by means of linear stability mechanisms).

The implementation of boundary conditions was straightforward for the calculations presented here. Dirichlet conditions are imposed at the upstream side [using eqs. (15) - (17) and, for the free shear layer problems, at the top and bottom (using free stream values)]. The downstream side is treated with standard outflow conditions for all variables. Wall boundary layers are treated by reflection, thereby allowing inviscid slip.

SECTION 3

FREE SHEAR LAYER CALCULATIONS

3.1 FORCED SHEAR LAYERS.

The purpose of these calculations was to investigate the dynamic response of a shear layer to particular perturbation frequencies, and to compare the results with experimental data. To that end, the shear layer parameters were chosen to correspond to the forced shear layer experiments of Ho and Huang (1982):

$$U_1 = 1.31 \quad , \quad U_2 = 0.69 \quad , \quad U_m = 1.0$$

$$\lambda = 0.31 \text{ and } r = U_2/U_1 = 0.53$$

$$\rho_1 = \rho_2 = 1 \quad , \quad \lambda\rho = o$$

In the above, the velocity components have been normalized by the average velocity of the two streams, and the density by the ambient value. The layers were initialized with uniform thermodynamic properties:

$$e_1 = e_2 = 44.63, \quad p_1 = p_2 = 17.86,$$

$$a_1 = a_2 = 5.0, \quad \gamma = 1.4$$

Note that by this choice of sound speed, the mean flow Mach number is $M_m = 0.2$. The fine-grid region consisted of 300 x-cells by 60 y-cells; the overall mesh covered a domain of 8600 by 3000. The initial shear layer width was 2 cells based on the maximum slope thickness, or say $\delta_o = 6$ cells based on the 99 percentile change in velocity. A one percent perturbation amplitude was used for each frequency. The dynamics of the flow was elucidated by tracking a material line that was embedded in the initial center line (i.e., inflection point) of the shear layer. Each calculation was run for 2000 cycles. The final interface shapes are depicted in Figure 2.

In the Mode I calculation (Fig. 2a), only the fundamental frequency ω_1 was used to perturb the layer. Undulations in the shear layer are first noticeable at $x \approx 24$, while the first cusp in the material line appears at $x \approx 75$. At larger distances, Figure 2 shows that the layer rolled up into discrete vortices that had a constant wavelength $L_1 = 3\delta_o$ corresponding to the fundamental frequency ω_1 (where $\delta_o = 6$). The width of the mixing region was about 18_o. For this Mode I response, the vortices continued to maintain their own identity, and no merging occurred for $x \lesssim 300$. There was, however, some "rebraiding effects," where material from the outer bottom edge of one vortex structure is drawn aft and down, thus forming the lower edge of the trailing vortex structure. In a similar fashion, material from the top of the trailing vortex is drawn forward, up and over the leading vortex — thereby again covering the braid region between vortices.

In the Mode II calculation, the first and second frequencies (ω_1 and ω_2) were used to perturb the layer. Initially, vortices formed at the fundamental wavelength L_1. Soon, however, pairs of vortices began interacting. The trailing vortex of each pair was drawn up and over and then entrained into the leading vortex — thus forming a larger-scale structure. Subsequently, these structures maintained their identity, and no further merging occurred for $x \lesssim 300$. The

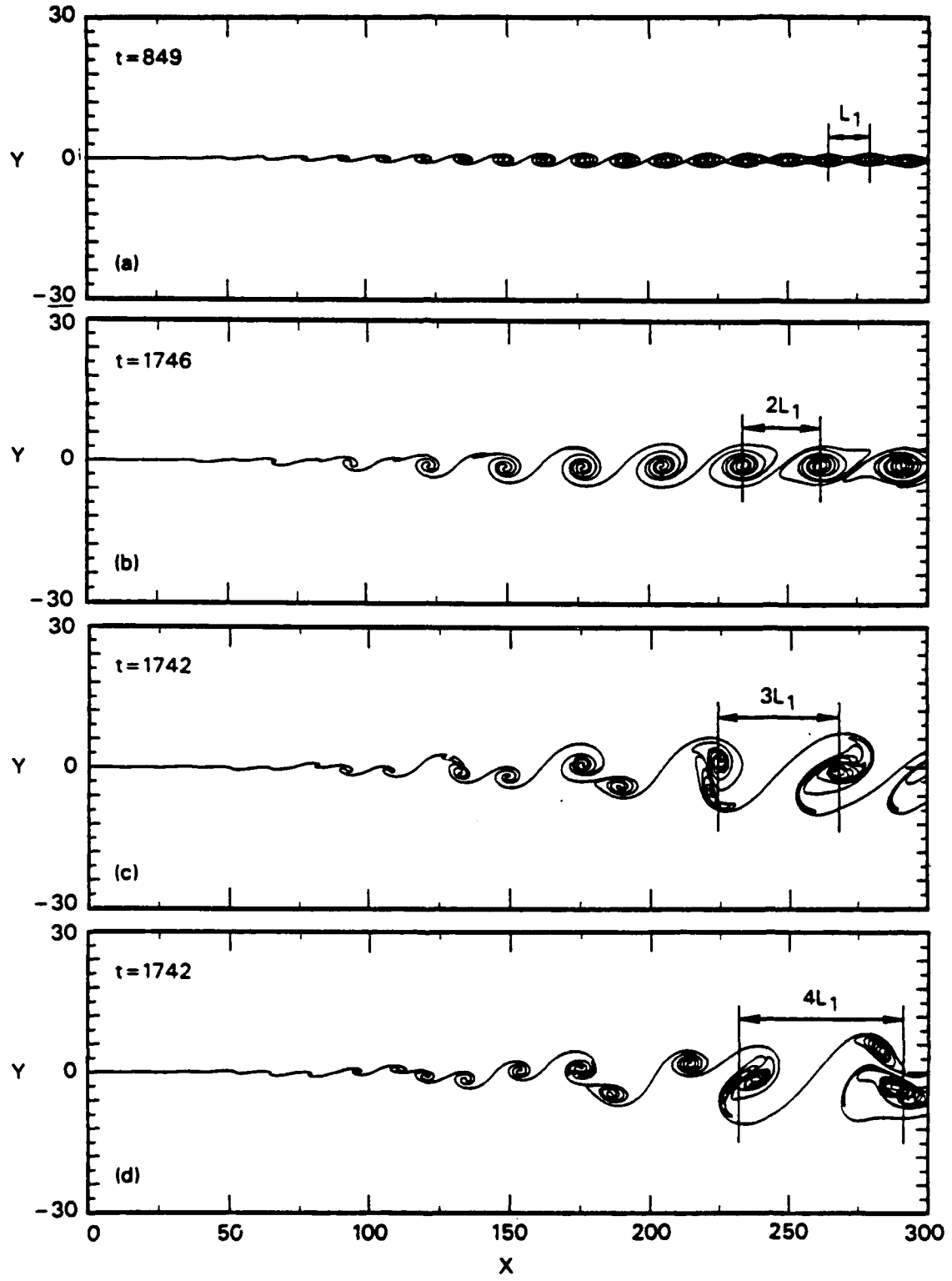

Figure 2. Numerical simulation of the forced shear layer experiments of Ho and Huang ($\lambda = 0.31, r = 0.53, \epsilon = 0.01$). Material interface plots: (a) Mode I response (ω_1 only); (b) Mode II response ($\omega_1 + \omega_2$); (c) Mode III response ($\omega_1 + \omega_3$); (d) Mode IV response ($\omega_1 + \omega_4$).

merged wavelength was twice the fundamental value ($L_2 = 2L_1 = 6\delta_o$), corresponding to the second frequency, $\omega_2 = \omega_1/2$. The final width of the mixing region was constant at about $2.5\delta_o$. The rollup of the material line in the merged structures was quite smooth and basically elliptical; five complete rotations of the central cusp can be observed. The start of rebraiding effects are visible near the right edge of the grid.

In the Mode III calculation, the first and third frequencies (ω_1 and ω_3) were used to perturb the layer. Just as before, vortices initially formed at the fundamental wavelength, L_1. Soon, however, vortices began interacting in groups of three, and a more complex merging pattern developed.

The third (or last) vortex was drawn up and over and entrained into the middle vortex, forming a stronger vortex pair. This pair attracted the leading vortex which was then entrained from below. The wavelength of the final merged structures was three times the fundamental value ($L_3 = 3L_1 = 9\delta_o$), corresponding to the third frequency, $\omega_3 = \omega_1/3$. The final width of the mixing region was constant at about $5\delta_o$. Rebraiding or further merging did not occur for $x \leq 300$. The rollup of the material line in the large structures was quite complicated in this case, due no doubt to the nonuniform distribution of vorticity created by the merging of three vortices.

In the Mode IV calculation, the first and fourth frequencies (ω_1 and ω_4) were used to perturb the layer. Again, vortices formed at the fundamental wavelength, L_1. Soon, however, vortices began interacting in groups of four, and a very complex merging pattern developed. First, the middle two vortices merged; then they entrained the leading vortex from below; finally, the last vortex was drawn up and over and entrained into the main structure. The merged wavelength was approximately four times the fundamental value ($L_4 = 4L_1 = 12\delta_o$). The computational grid was too short to establish the asymptotic vortex pattern and mixing region width. As in Mode III, the rollup of the material line in the merged structures was very complicated due to the nonuniform distribution of vorticity created by the merging of four vortices.

The above-described dynamic response duplicates the experimental results found by Ho and Huang (1982) in their forced shear layer experiments for all modes that they studied Modes I through IV).

These results indicate that the dynamic response of a shear layer is *deterministically* related to the perturbation frequencies. If only the fundamental frequency (ω_1) and one subharmonic (ω_n) perturbations are used, the vortices merge to form periodic large-scale structures with a constant wavelength $L_n = nL_1$. No further merging occurs, and the width of the mixing region remains constant at a value of about $2.5(n-1)\delta_o$. Hence, continued growth of the mixing region requires the addition of smaller and smaller frequency (i.e. longer and longer wavelength) perturbations. Preliminary calculations supporting these conclusions were reported in Chien et al. (1987).

3.2 SPREADING SHEAR LAYER.

A variety of perturbation frequencies are present in most actual shear layers, and the mixing width of the shear layer continues to grow with increasing distance. This section describes a numerical simulation of just such a situation, namely, the fundamental shear layer experiments of Brown and Roshko (1974). The particular case

considered was that of a 5 m/s helium flow (state 1) over a 1.89 m/s nitrogen flow (state 2); expressed in terms of the shear layer parameters, these become:

$$U_1 = 1.451, \quad U_2 = 0.549, \quad U_m = 1.00$$

$$\lambda = 0.451, \quad r = U_2/U_1 = 0.378$$

$$\rho_1 = 1 \quad , \rho_2 = 7 \quad , \lambda_\rho = -0.75$$

In the above, the velocity components have been nondimensionalized by the average velocity of the two streams, and the density by ρ_1. By design, the dynamic pressure of the two streams are equal.

The calculation was performed on a grid with a fine-zoned region of 500 x-cells by 100 y-cells ($\Delta x = \Delta y = 1$); the complete grid covers a domain of 8800 by 3000. Again, the initial shear layer width was $\delta_o = 6$ cells (based on the 99 percentile change in velocity). The flow field was initialized by a Tanh(y) profile for both the velocity (Eq. 8) and density field (Eq. 12), and a uniform pressure: $p_1 = p_2 = 17.86$. The pressure was selected so that the mean flow Mach number was $M_m = 0.4$ (while $M_1 = M_2 = 0.29$). Only the velocity field was perturbed on the left boundary (according to Eq. 15). For the first thousand cycles only the fundamental perturbation frequency ω_1 was used so that the mixing started gradually; thereafter (cycles 1,000 to 10,000) the first ten modes were used to model the natural growth of a spectrum of small perturbations present in most experiments. A material line (initially on the center line of the shear layer) was tracked to follow the distortion of the interface.

The dynamic evolution of the shear layer is depicted in Figure 3 by means of material interface plots at various times. The first cusp or kink in the material line appears at x = 65. Clockwise-rotating vortex structures form initially at the fundamental wavelength L_1; but these rapidly merge to form larger-scale structures. In this way, the mixing width continues to grow with increasing streamwise distance.

The response of the shear layer was approximately periodic. Figure 3 depicts the evolution of the interface over one such period from frame a (t = 4035) to frame s (t = 5013)|; frame t shows that this interface shape reappears again at t = 6018, thus the period of the overall flow is Δt = 1000. The following is a detailed description of the development of the large-scale structures depicted in frame s (t = 5013). The individual vortex structures are labeled sequentially with cardinal numbers. Considered first is the formation of the largest-scale structure, of frame s, structure 6-12. Vortices 6, 7 and 8 merge (frames d through g) in a Mode III response to form structure 6-8. Vortices 9 and 10 pair and merge (frames g through j) in a Mode II response; vortices 11 and 12 also pair and merge (frames h through j). Finally, structures 6-8 and 9, 10 and 11, 12 interact and merge to form the largest-scale structure 6-12 shown in frame s.

In the meantime, structure 13-18 has been developing. Vortices 13, 14 and 15 merge (frames i through l) in a Mode III response; vortices 16, 17 and 18 also merge (frames j through l) in a Mode III response. Then structure 13-15 pairs and merges with structure 16-18 (frames n through p) in a Mode VI response, resulting in the large-scale structure 13-18.

At the same time, structure 19-24 has been developing. Vortices 19, 20 and 21 merge (frames k through m) in a Mode III response; vortices 22, 23 and 24 also merge (frames m through o) in a Mode III response. Finally, structure 19–21 pairs

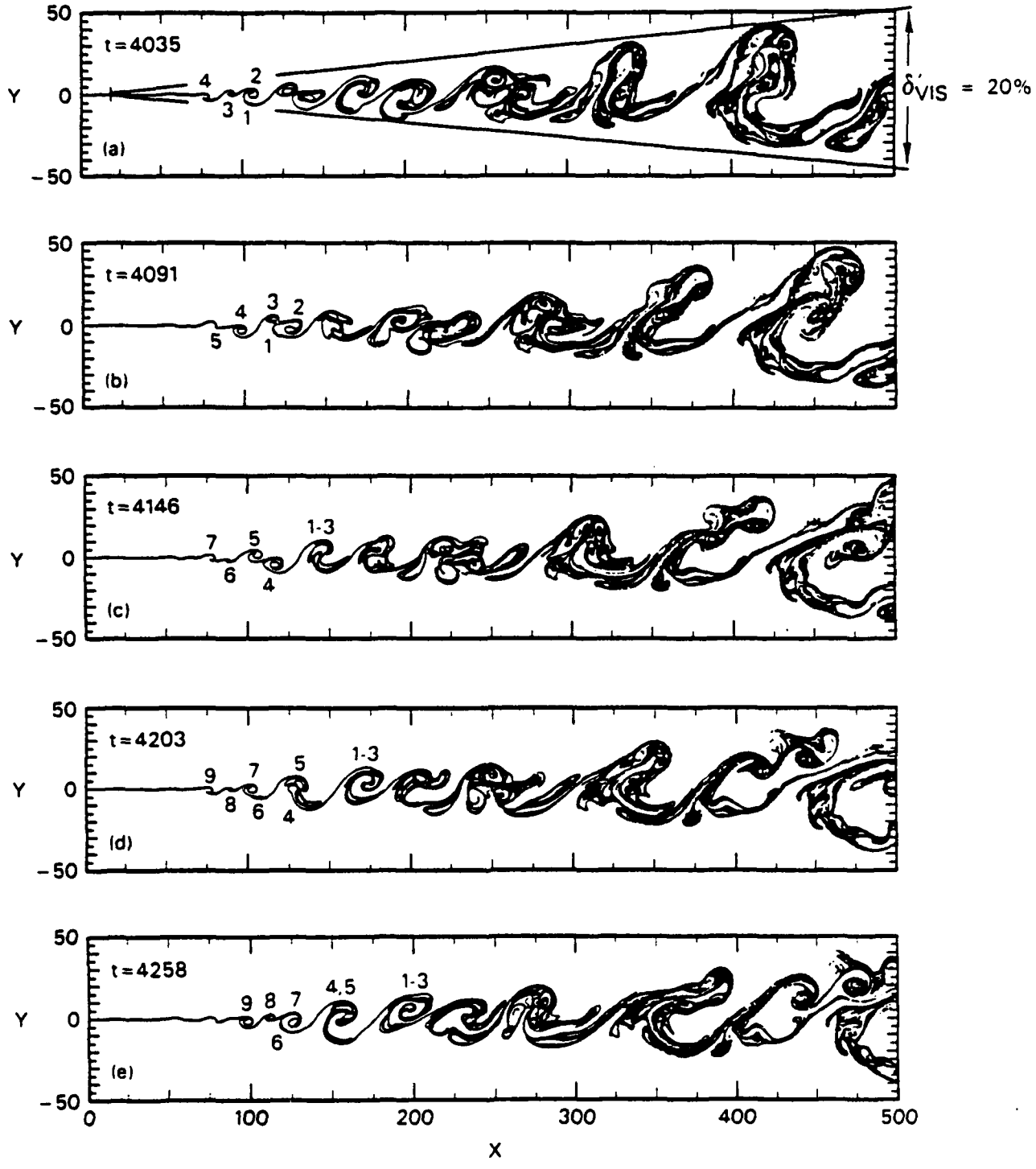

Figure 3. Numerical simulation of the spreading shear layer experiment of Brown and Roshko (λ = 0.451, r = 0.378, ρ_2/ρ_1 = 7).

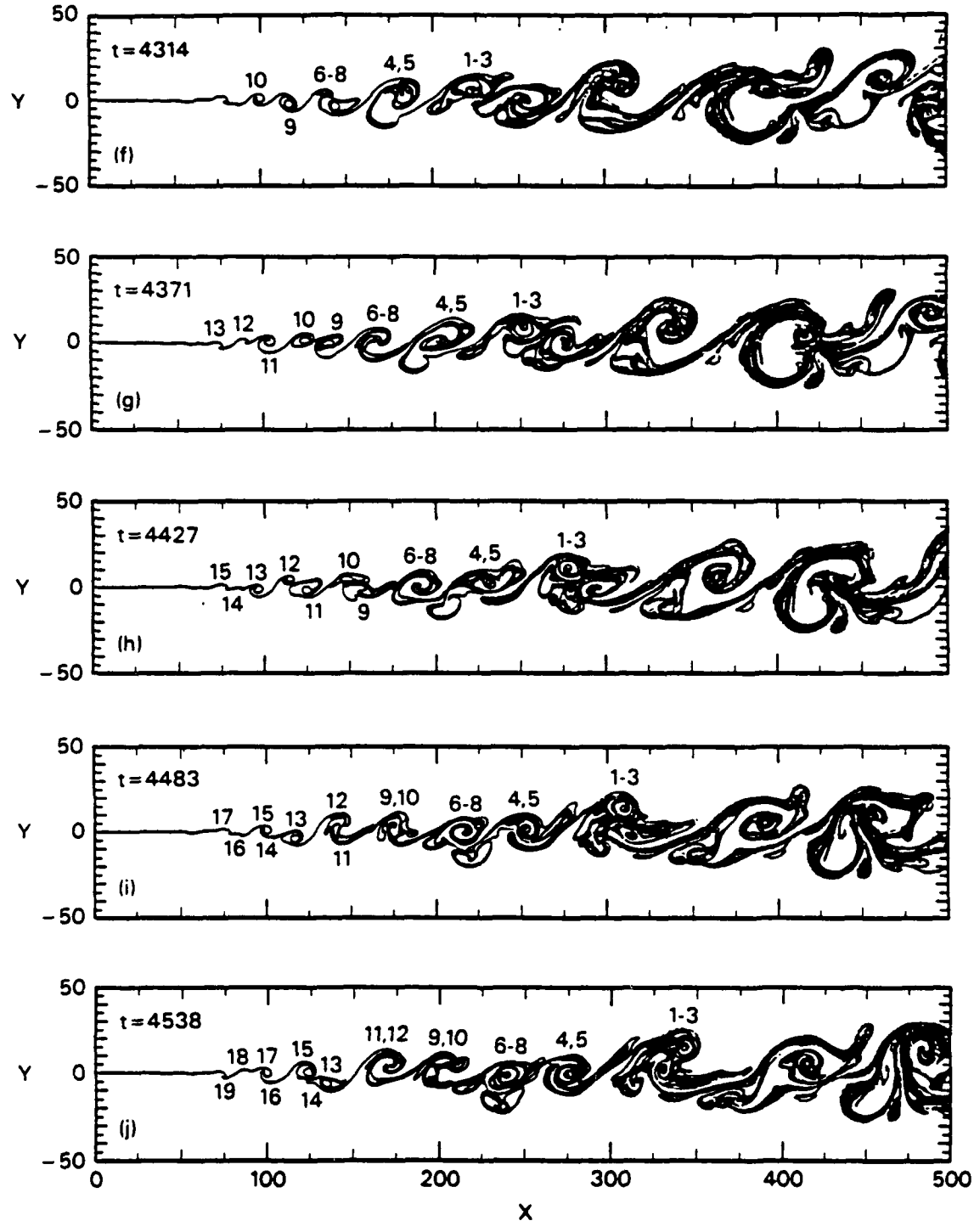

Figure 3. Numerical simulation of the spreading shear layer experiment of Brown and Roshko (λ = 0.451, r = 0.378, ρ_2/ρ_1 = 7) (Continued).

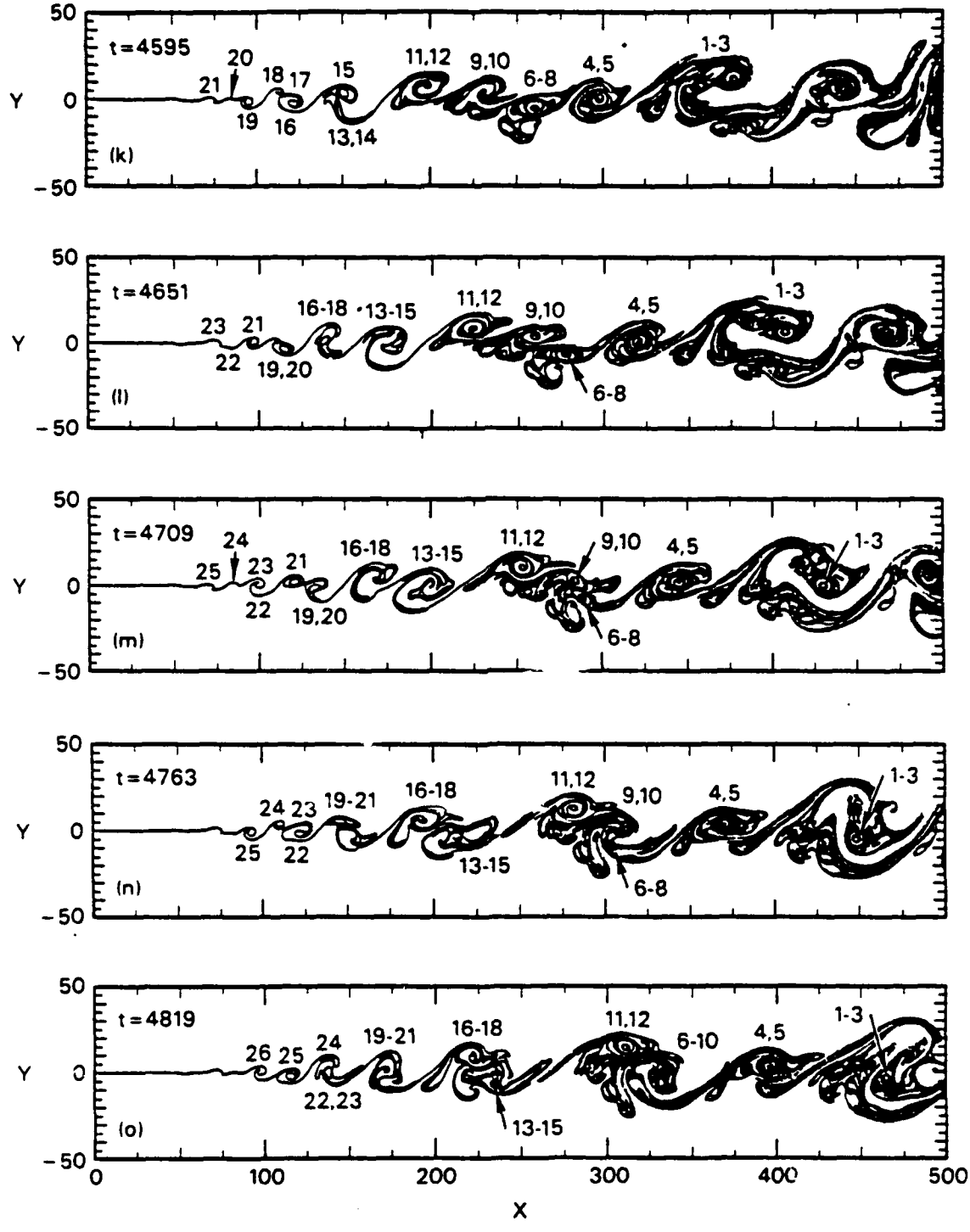

Figure 3. Numerical simulation of the spreading shear layer experiment of Brown and Roshko (λ = 0.451, r = 0.378, ρ_2/ρ_1 = 7) (Continued).

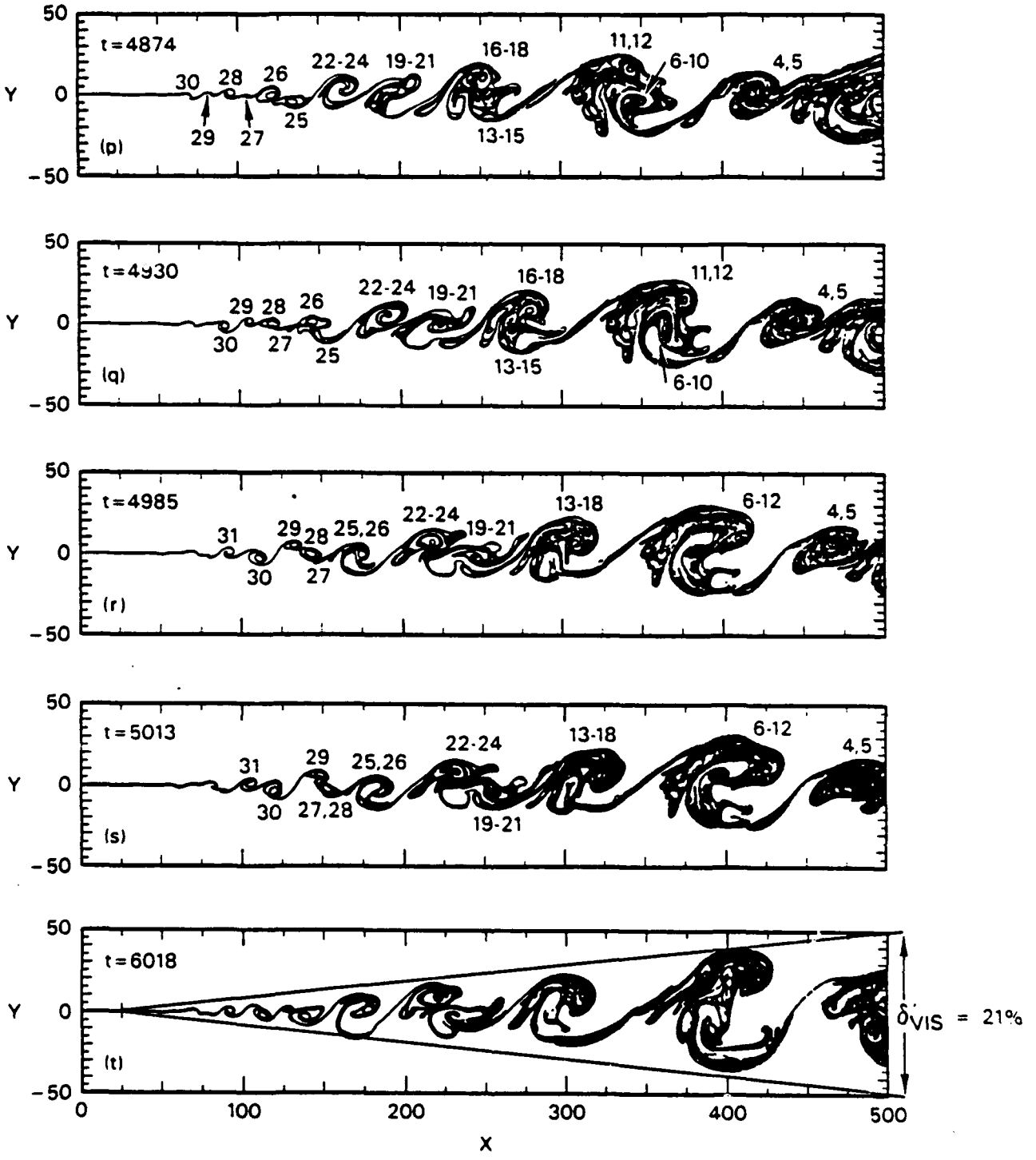

Figure 3. Numerical simulation of the spreading shear layer experiment of Brown and Roshko (λ = 0.451, r = 0.378, ρ_2/ρ_1 = 7) (Concluded).

with structure 22-24 (frames r and s) in a Mode VI response, resulting in structure 19-24 as shown in frame s.

In summary, the large-scale structures are created by Mode II, III and VI merging processes. Interface shapes periodically reappear every $\Delta t = 1000$.

The material interface in Figure 3 is actually represented by unconnected dots or tracer points. Initially the interface contained 5,000 such points (ten points per Δx). The number of tracers rapidly increased during the calculation to a maximum of 75,000 points due to the large strain in the braid regions between structures. The length of the interface increased by at least a factor of 15 due to the continued vortex-merging process.

The initial material interface fluid seems to cover a significant fraction of the cross-sectional area of the large structures. This is a consequence of mixing by an inviscid, nondiffusive folding of the material interface. Hence, regions of essentially pure helium are interleaved with regions of pure nitrogen. This effect is visible in experimental photographs to be shown next.

Figure 4(a) depicts the calculated material interface at t = 5013. For comparison, Figure 4(b) presents a shadowgraph picture of the helium-nitrogen interface recorded during the shear layer experiments (Brown and Roshko, 1974; Fig. 3d). Similarities between the calculated and experimental interface are remarkable. The calculated spreading rate varied between 18 and 22 percent, which is in excellent agreement with visual spreading rate of $\delta'_{vis} = 21$ percent observed in the experiment. The shape and wavelength of the large-scale structures are quite similar. The fine white and black lines on the large structures of the experiment may now be understood, in light of Fig. 4a, as folded or interleaved regions of pure helium or pure nitrogen.

Also included in Figure 4 are the corresponding density, vorticity and overpressure contours. The shape of the large structures as deduced from the density contours agrees with the material interface shape, indicating little numerical diffusion. It is interesting to note that vorticity is created near the braid regions and entrained into the structures. Approximately circular low pressure regions are found in each large structure, and this generates a radial pressure gradient. As the helium-nitrogen interface is entrained obliquely through this pressure gradient, vorticity is generated by the baroclinic $|\nabla (1/\rho) \times \nabla p|$ mechanism. The magnitude of the baroclinicly-generated vorticity reaches about minus one half of the inflow vorticity, hence it must have an effect on the flow. Indeed, close inspection of the material interface reveals some smaller-scale vortices rotating in the counterclockwise direction. This causes the merging patterns to be considerably more complex and less regular than in Figure 2.

Figure 5 depicts the flow field near the center line (i.e., y = 0.5) at t = 5013. Large fluctuations are evident in the velocity, density and dynamic pressure. In fact, densities corresponding to pure helium and to pure nitrogen are seen near the center line; similarly, the velocity fluctuates between values corresponding to approximately U_1 and to U_2. Overpressure fluctuations are small (between +1.5 to -4.0 percent of ambient), which is quite comforting in light of the Mach number compromise ($0.29 \leq M \leq 0.4$) used for this calculation.

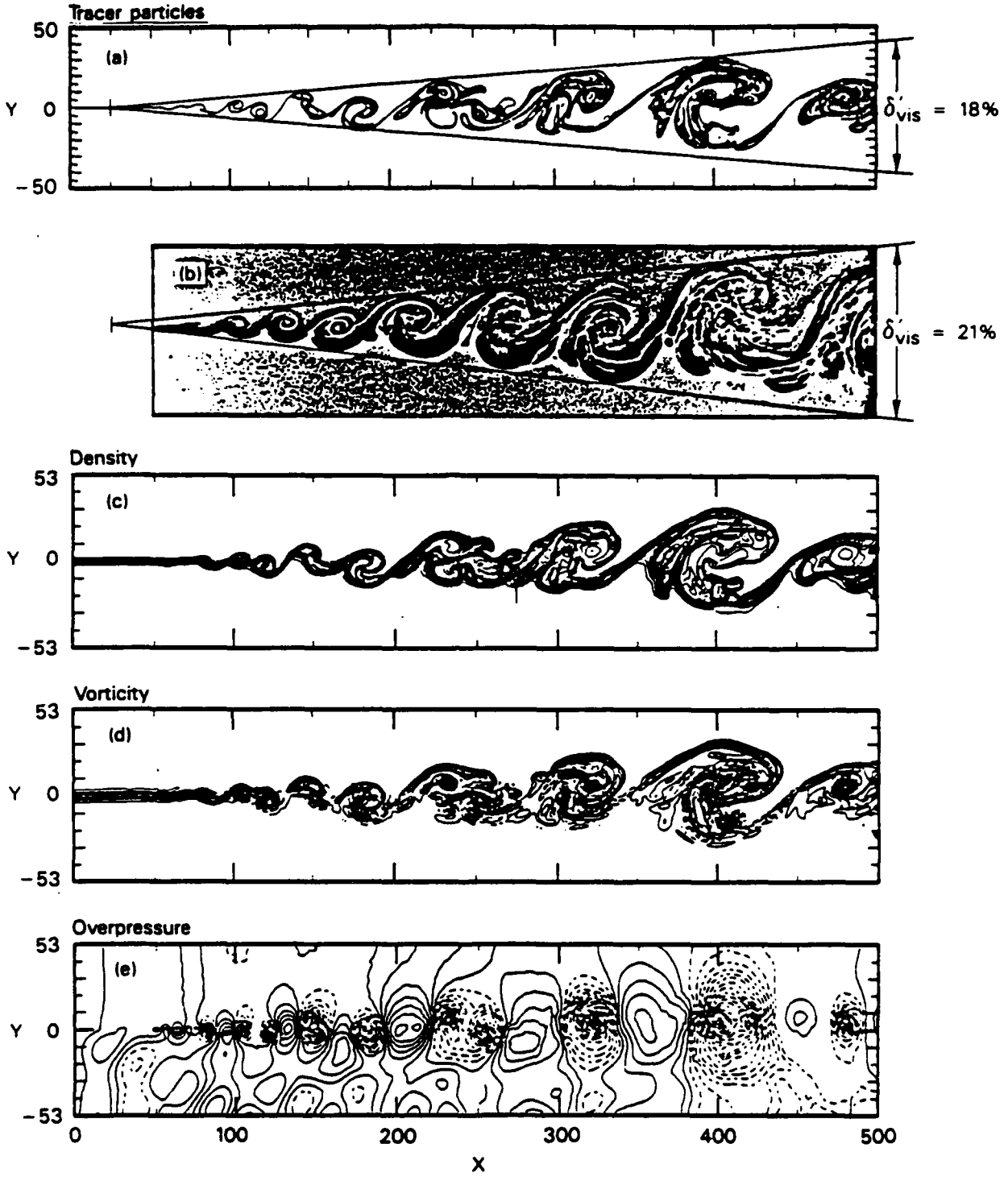

Figure 4. Flowfield of the spreading shear layer calculation at t = 5013: (a) material interface: (b) shadowgraph from the Brown and Roshko experiment (Figure 3): (c) density contours; (d) vorticity contours (solid lines denote negative values and dashed lines correspond to positive values that are baroclinicly generated): (e) overpressure contours (solid lines denote positive values).

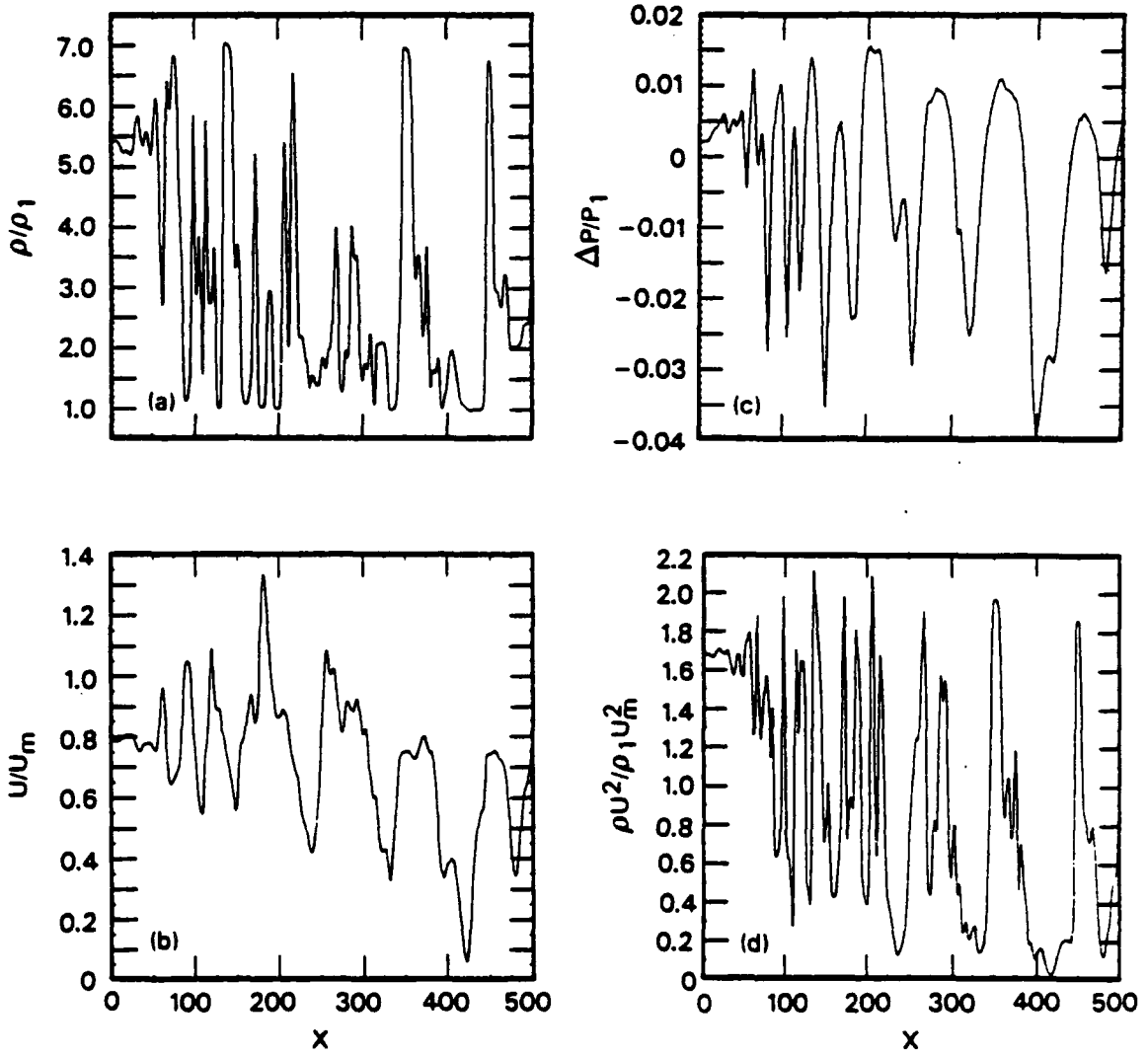

Figure 5. Flow field along the center line (y = 0.5) of the spreading shear layer calculation at t = 5013: (a) density; (b) streamwise velocity; (c) overpressure: (d) dynamic pressure.

Monitoring stations located at x = 100, 200, and 400 were used to store the flow field time histories. These were then integrated in time over the last 2000 cycles of the calculation (about 6 periods of the large-scale structures at x = 400) to establish the mean shear layer profiles. The mean velocity and density profiles are depicted in Figure 6. The three stations are compared by means of the scaling variable:

$$\eta_{SL} = y \;/\; (x - x_o) \qquad (20)$$

where x_o denotes the effective origin of the breakdown of the shear layer (x_o = 25, according to Fig. 5). The profiles seem to collapse reasonably well with this scaling. The shear layer is resolved across approximately 10, 25 and 50 computational cells at the first, second and third stations, respectively.

The shaded curves in that figure denote the mean profiles as measured by Brown and Roshko (1974). The calculated density profiles are in excellent agreement with the experimental profiles — even to such detailed features as multiple inflection points and plateau regions (e.g., near η = 0.05). Agreement between the calculated and measured mean velocity profiles is also good, considering the accuracy of evaluating the velocities from pitot tube measurements for flows with large density variations.

The mean transverse velocities lie in the range:

$$\bar{v}/U_1 \cong \begin{cases} 0.016 \;\; (\text{for } \eta_{SL} > 0.05) \\ 0 \;\; (\text{for } \eta_{SL} = o) \\ -0.008 \;\; (\text{for } \eta_{SL} < -0.05) \end{cases}$$

indicating that the mixing creates an outward displacement of the streamlines on either side of the shear layer. The mean pressure profile was constant and equal to the ambient value.

Figure 7 presents the fluctuating flow profiles corresponding to the mean flow depicted in Figure 6. These were calculated as root-mean-square time averages about the mean values using the last 2000 cycles. There, u′ and v′ represent the streamwise and transverse velocity fluctuations, $\overline{u'v'}$ denotes the fluctuating shear stress, while ρ' and p' represent the density and pressure fluctuations, respectively. The fluctuating flow profiles are reasonably smooth, except for $\overline{u'v'}$ which probably requires a longer time average to achieve convergence. The profiles are remarkably similar, considering that the rotational structures at x = 400 are much more complex than at x = 100. The shaded region in Figure 7d denotes the fluctuating density profile measured by Konrad (1977) for the same shear layer that was studied by Brown and Roshko. The calculated density profiles are in excellent agreement with this data — even the detailed features such as the peak values and the plateau region near η_{SL} = 0.07 agree quite well.

The dashed curves in Figure 7 represent the r.m.s. velocity fluctuations as measured by Oster and Wygnanski (1982; their Figs. 6a, 7b and 7c) for a constant density shear layer with a different velocity ratio. Our calculated profiles are only qualitatively similar to their profiles. For example, they find only single-peaked profiles, while our calculated profiles of u' and $\overline{u'v'}$ have a central peak and side lobes, the latter being caused by the large density in our problem.

The peak values of the fluctuating quantities are compared with other shear layer studies in Table 1. The present results agree quite well with the peak values obtained from the 2D, inviscid, vortex

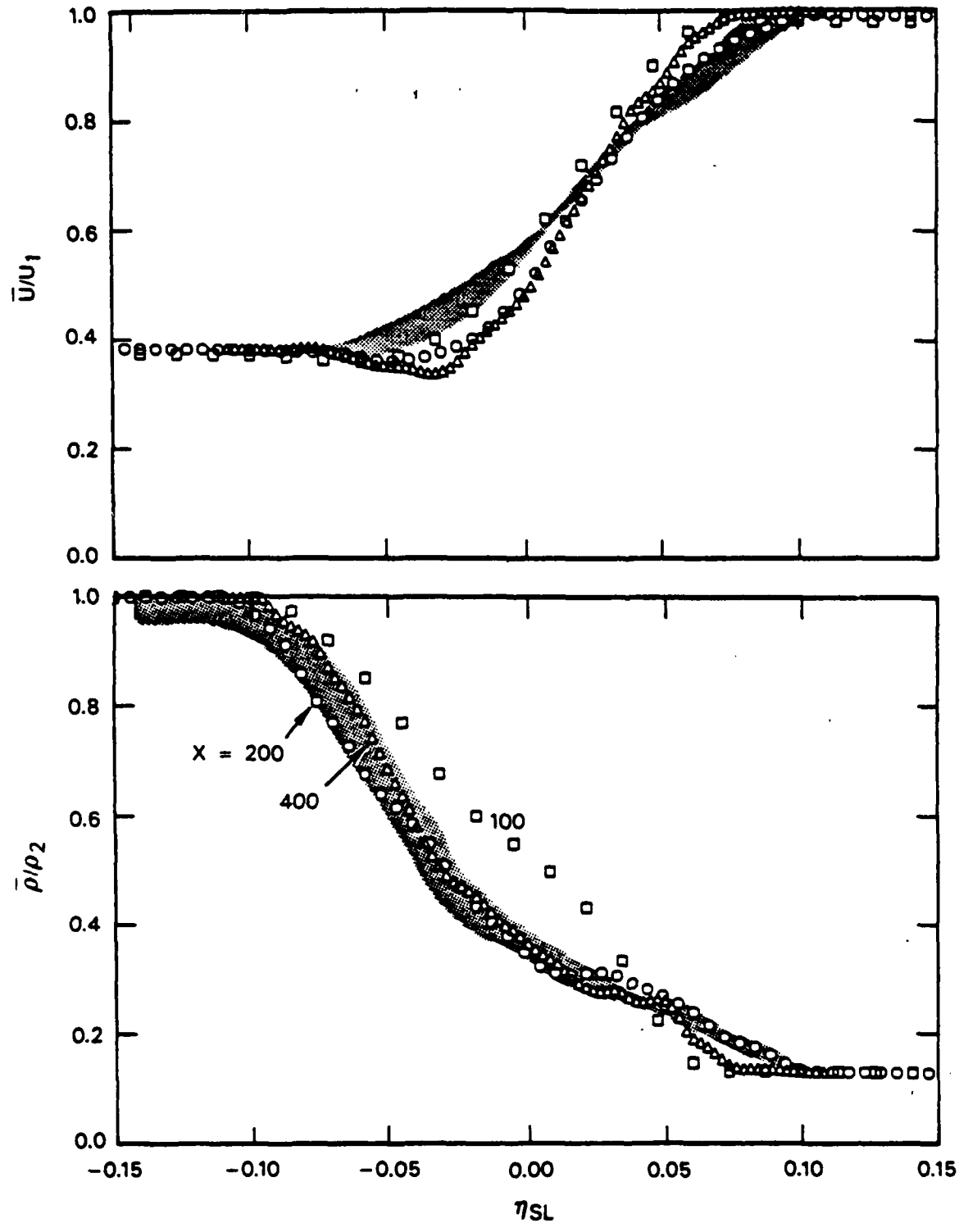

Figure 6. Mean-flow profiles of the spreading shear layer calculation: (a) streamwise velocity profiles; (b) density profiles. Symbols □, ○ and Δ denote stations at x = 100, 200 and 400, respectively. Shaded area denotes the experimental data band from Brown and Roshko (1974).

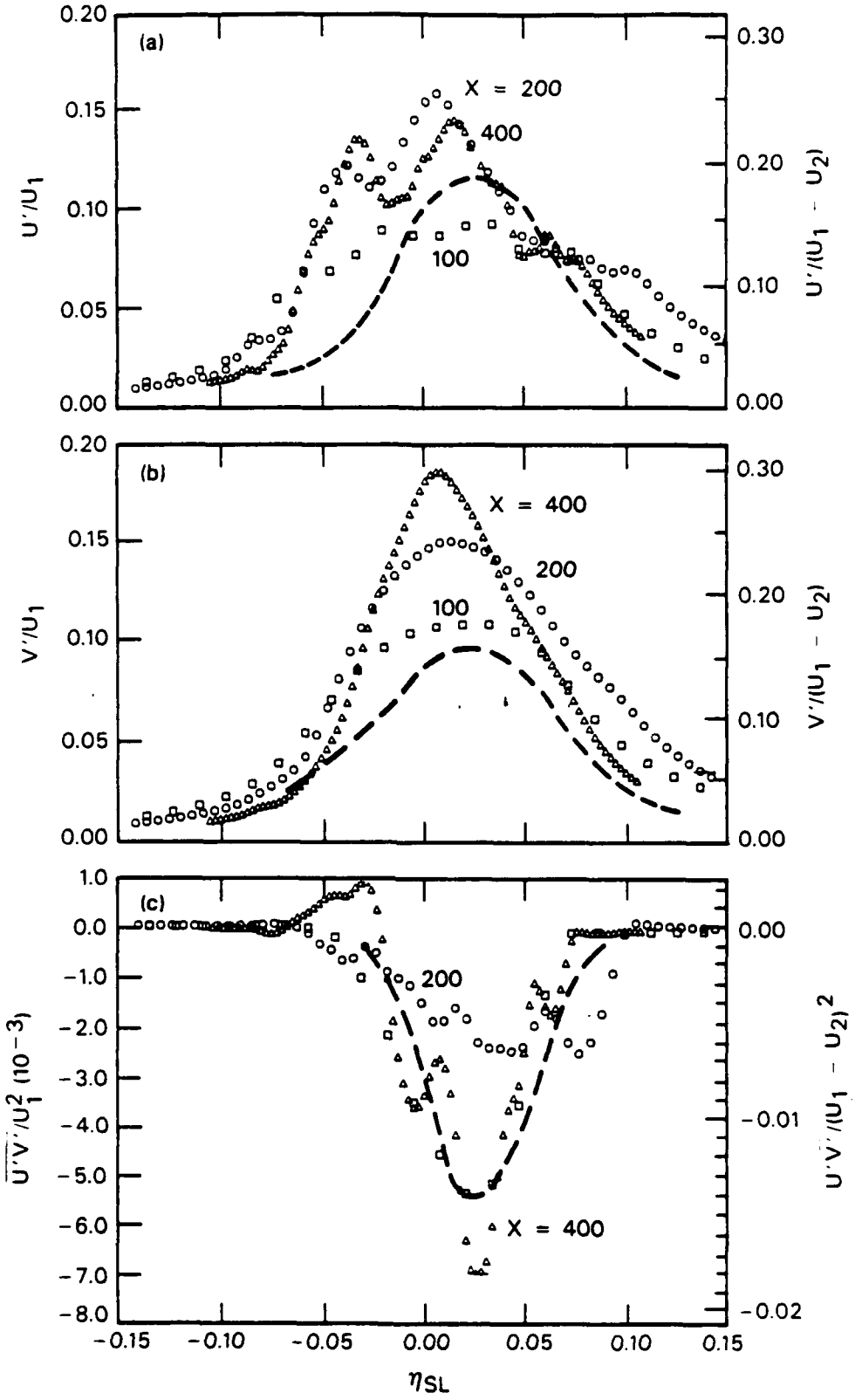

Figure 7. Time-averaged fluctuating flow profiles from the spreading shear layer calculations: (a) streamwise velocity; (b) transverse velocity; (c) shear stress; (d) density (shaded region corresponds to the experimental data band of Konrad [1977]); (e) pressure. Symbols □, ○ and Δ denote stations at x = 100, 200 and 400, respectively. Dashed curves denote the data of Oster and Wygnanski (1982) for an unforced shear layer (their Region 1).

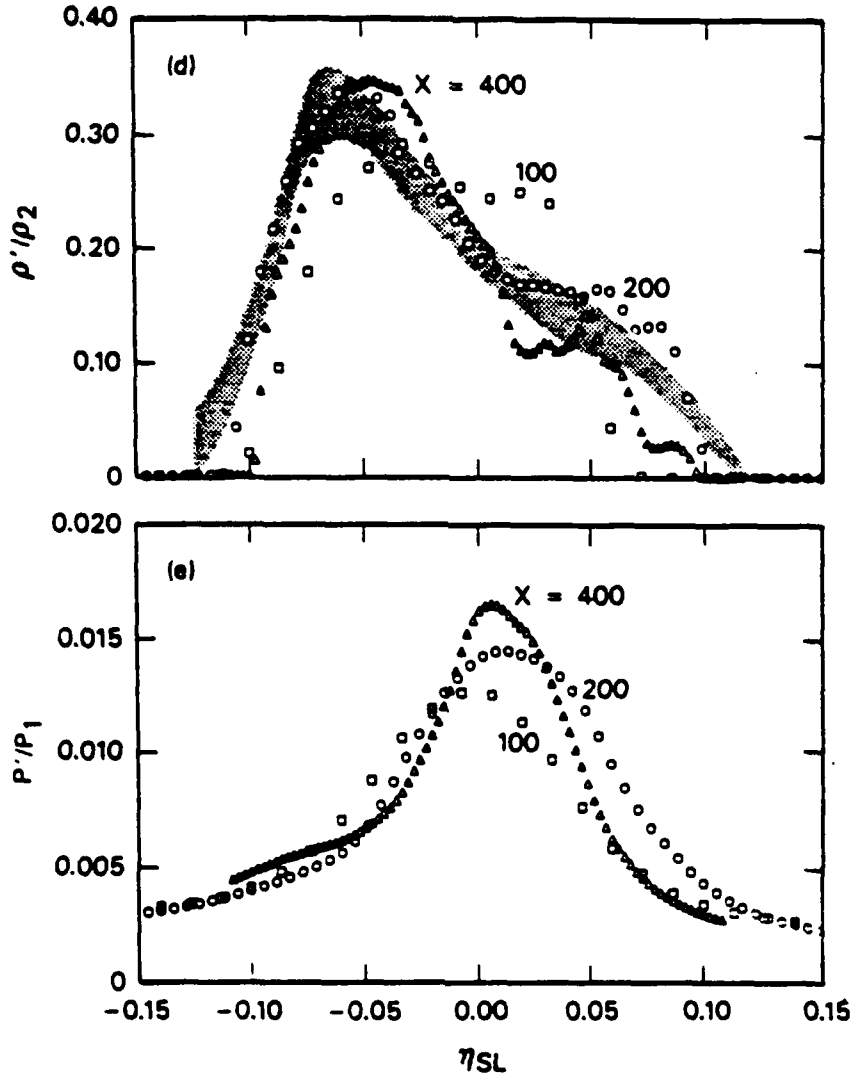

Figure 7. Time-averaged fluctuating flow profiles from the spreading shear layer calculations (Concluded).

Table 1. Comparison of Peak Fluctuating Quantities.

Case	Conditions			Peak Values (10^{-2})					
FREE SHEAR LAYERS	λ	r	λ_ρ	u'/U_1	v'/U_1	w'/U_1	$-\overline{u'v'}/U_1^2$	ρ'/ρ_2	p'/p_1
Vortex Dynamics Calc (Inoue, 1985)	0.25	0.6	0	13	9.3	--	0.32-0.38	--	--
Oster and	0.25	0.6	0	7.2	6.1	5.8	0.21	--	--
Wygnanski (1982)	0.45	0.38	0	11.2[a]	9.5[a]	9.0[a]	0.50[a]	--	--
Present Calculations	0.45	0.38	-0.75						
x = 100				9.4	11.2	--	0.54	29	1.3
x = 200				15.9	15.4	--	0.25	35	1.5
x = 400				14.5	18.8	--	0.69	35	1.7
WALL SHEAR LAYERS	λ	r	λ_e	u/U_∞	v'/U_∞	w'/U_∞	$-\overline{u'v'}/U_\infty^2$	ρ'/ρ_∞	p'/p_∞
Shock Tube Case									
x = 400	-0.39	2.27	0.20	19	10	--	0.13	11	8
x = 600				26	12	--	0.16	13	9
x = 800				29	14	--	0.12	12	10
x = 950				31	15	--	0.059	10	11
Owen et al. (1975)				--	--	--	--	10	--
Tripped Flat Plate Case	1	0	0						
x = 400				18.5	7.26	--	0.0531	0.169	0.212
x = 600				18.1	7.36	--	0.0259	0.156	0.191
x = 800				17.6	7.25	--	0.0226	0.144	0.175
x = 950				17.1	7.15	--	0.0186	0.135	0.162
Klebanoff (1955)				8.75	4.0	6.4	0.138[b]	--	--
WALL JET	λ	r	λ_ρ	u'/U_J	v'/U_J		$\overline{u'v'}/U_J^2$	ρ'/ρ_J	p'/p_J
Present Calculations	-1	∞	0						
x = 85 (5H)				23	28	--	1.85	0.75	1.0
x = 170 (10H)				25-28	33	--	4.5	0.83	1.1
Bajura and Catalano (1975)	-1	∞	0						
x = 10H				0.7	--	--	--	--	--
x = 20H				2.0	--	--	--	--	--

[a]Scaled values, based on $\Delta U/U_1 = 0.622$.
[b]Evaluated from Eq. 38

dynamics calculations of Inoue (1985). The present peak values are 1.5 to 2 times larger than the experimental data of Oster and Wygnanski (1982). Of course, there are differences in the problems considered (e.g., different λ and λ_ρ), and the experimental data certainly includes the effects of viscous diffusion and dissipation, but the latter effects should be small because of the large Reynolds number of the flow. Probably the main reason why the calculated peaks (especially u′ and v′) are larger than the data is that the calculations are two dimensional while the experimental data contained three dimensional fluctuations — that is, some of the fluctuating kinetic energy is stored in the third dimension.

3.3 SUMMARY.

These results indicate that the dynamic response of a disturbed shear layer is basically independent of the initial shear layer profile, and independent of the perturbing frequency as long as a spectrum of frequencies are available to the flow. Small perturbations cause the shear layer to roll up into periodic vortices. Subharmonic perturbations cause these vortices to merge — forming successively larger-scale rotational structures. The dynamics of the large-scale structures determines the mixing of the two streams and controls the fluctuations. The present inviscid numerical simulations agree rather well with experimental data — not only for such macroscopic features like the spreading rate ($\delta'_{vis} \approx 0.21$) and the shape and wavelength of the large-scale structures, but also in mean flow profiles such as density and velocity. Even the time-averaged fluctuating flow profiles such as density agree with the data. Hence, we conclude that the dynamic evolution of the large-scale structures is dominated by inviscid effects that are well approximated by nonsteady solutions of the conservation laws of gas dynamics.

The present large-Reynolds-number approach (i.e., the direct solution of the nonsteady conservation laws of gas dynamics) offers then one technique for extending the numerical simulations of fluctuating shear layers to the compressible flow regime. The next section presents an example of just such a case.

SECTION 4

WALL SHEAR LAYER CALCULATIONS

4.1 SHOCK TUBE EXPERIMENT.

Considered next is the evolution of a wall shear layer (i.e., a boundary layer) behind a shock wave in a shock tube. The key physical aspects of the problem are depicted in Figure 8. This is a tracing of a shadow photograph provided by Dr. H. Reichenbach (Ernst Mach Institut, FRG). A planar, constant velocity shock (Mach number M_S = 1.7) is shown propagating to the left. The test section floor consisted of a smooth steel plate (roughness height less than 1 μm), while the roof consisted of a smooth, porous plate (ceramic Filtrokelit; roughness height less than 30 μm). Periodic acoustic waves emanate from the point where the shock front intersects the floor or roof. These waves have a constant spacing of about 1 mm. Scanning-electron-microscope photographs of the surface show that even such nominally smooth surfaces are still rough on length scales which are large compared to the shock front thickness. Hence, a shock wave cannot propagate with uniform velocity very near the surface. It reflects from the front face of each roughness element, thereby enhancing its strength, and as it propagates down the backside of each roughness element, it loses strength. Therefore, near the surface the shock front velocity must oscillate, even though it propagates with a constant velocity at large distances from the surface.

Figure 8 also depicts periodic density structures in the roof and floor boundary layer. (The wall boundary layer gas is cooler and denser than the free-stream flow, and therefore, detectable by schlieren or shadowgraph techniques). These organized structures are inclined to the flow at an angle of approximately 45°. Their wavelength is regular and constant at about 1 mm, which is similar to the acoustic wave spacing and, of course, much longer than any wall roughness wavelengths. Similar organized structures have been reported by Spina and Smits (1987) for turbulent boundary layers in steady, compressible flow (while Prandtl [1933], Bergh [1958] and Gad-el-Hak et al. [1984] have reported the existence of organized structures in steady, incompressible boundary layers). Hence, we postulate that the oscillations in the shock front velocity trip the wall boundary layer, which rolls up into periodic vortex structures and thereby generates acoustic waves that radiate away from the foot of the shock front.

The auxiliary scale in Figure 8 depicts the Reynolds number based on distance behind the shock front. The flow reaches a critical Reynolds number of 3×10^5 at a distance of only 15 mm behind the shock, hence, essentially the entire boundary layer may be characterized as large Reynolds number, turbulent flow.

The flow conditions across the M_S = 1.70 shock front are listed in Table 2. In stationary coordinates, states 1 and 2 denote conditions ahead and behind the shock front, respectively.

4.2 FORMULATION.

A numerical simulation of this shock tube experiment was performed in the same spirit as the simulation of the Brown and Roshko shear layer case. Namely, we test

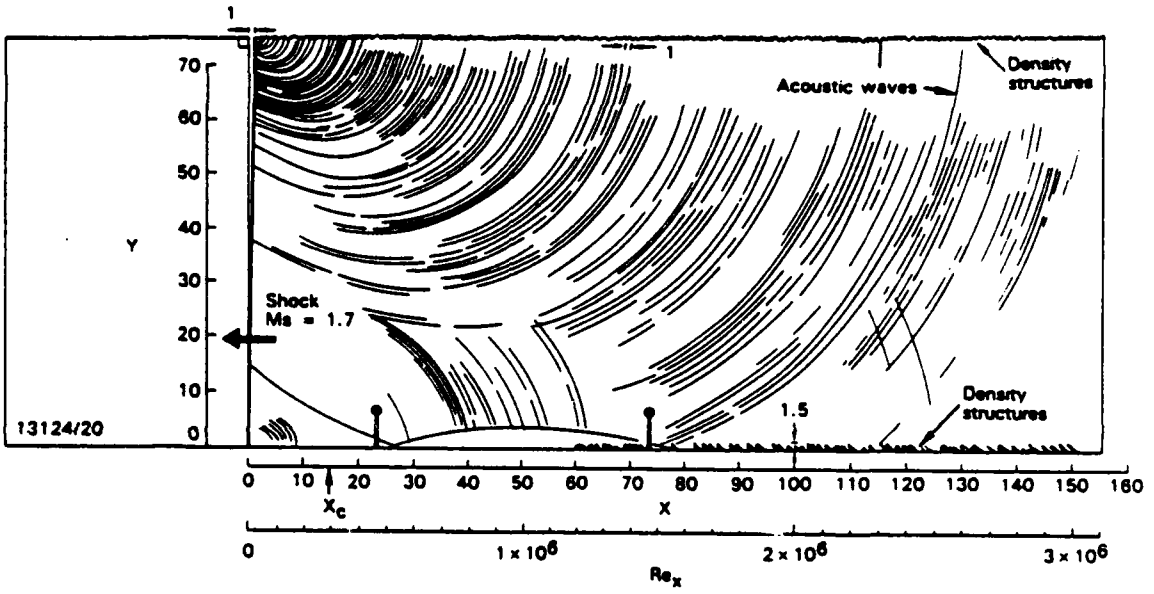

Figure 8. Tracing of a shadow-schlieren photograph of the waves induced by the boundary layer behind a Mach M_s = 1.7 shock wave. Acoustic waves radiate from the foot of the shock. Density structures are formed in the wall boundary layer. (Courtesy of Dr. H. Reichenbach, Ernst Mach Institute FRG.)

Table 2. Shock Conditions (M_s = 1.70, γ = 1,4).

Flow Field	Stationary Coordinates		Shock-Fixed Coordinates	
	State 1	State 2	Wall (y=0)	Edge (y=∞)
p/p_1	1	3.2	~3.2	3.2
ρ/ρ_1	1	2.2	3.2	2.2
e/e_1	1	1.46	1.0	1.46
a/a_1	1	1.21	1.0	1.21
u/a_1	0	0.94	1.70	0.77
u/a (local)	0	0.77	1.70	0.64

the postulate that the dynamics of this wall boundary layer flow is dominated by two-dimensional inviscid flow effects by comparing the calculated results with boundary layer data.

The calculation was performed in shock-fixed coordinates with the shock located at x = o. similar to those used by Mirels (1956). In these coordinates, the gas velocity varies between the value u_e at the edge of the boundary layer (y = ∞)

$$u_e/a_1 = (w_s - u_2)/a_1 = 0.77$$

to a maximum value u_w on the wall (y = o)

$$u_w/a_1 = w_s/a_1 = 1.70$$

where the gas moves with the shock velocity, the latter being precisely the no-slip condition in shock-fixed coordinates. The temperature varies between the edge value of 430 K, to the wall value of 294 K, with the latter corresponding to an ambient temperature wall boundary condition. Other flow variables are listed in Table 2.

The calculation was performed on a grid with a fine-zoned region consisting of 500 x-cells (Δx = 2) by 60 y-cells (Δy = 1), as shown schematically in Figure 9. Expanding cells were used above and to the right of the fine-zoned region to cover a total domain of 17600 by 3000.

The laminar boundary layer behind the shock was approximated by a Tanh(y) profile for the streamwise velocity and internal energy:

$$u(x, y, o)/a_1 = M_s\, f(y)$$
$$v(x, y, o) = 0 \qquad (21)$$

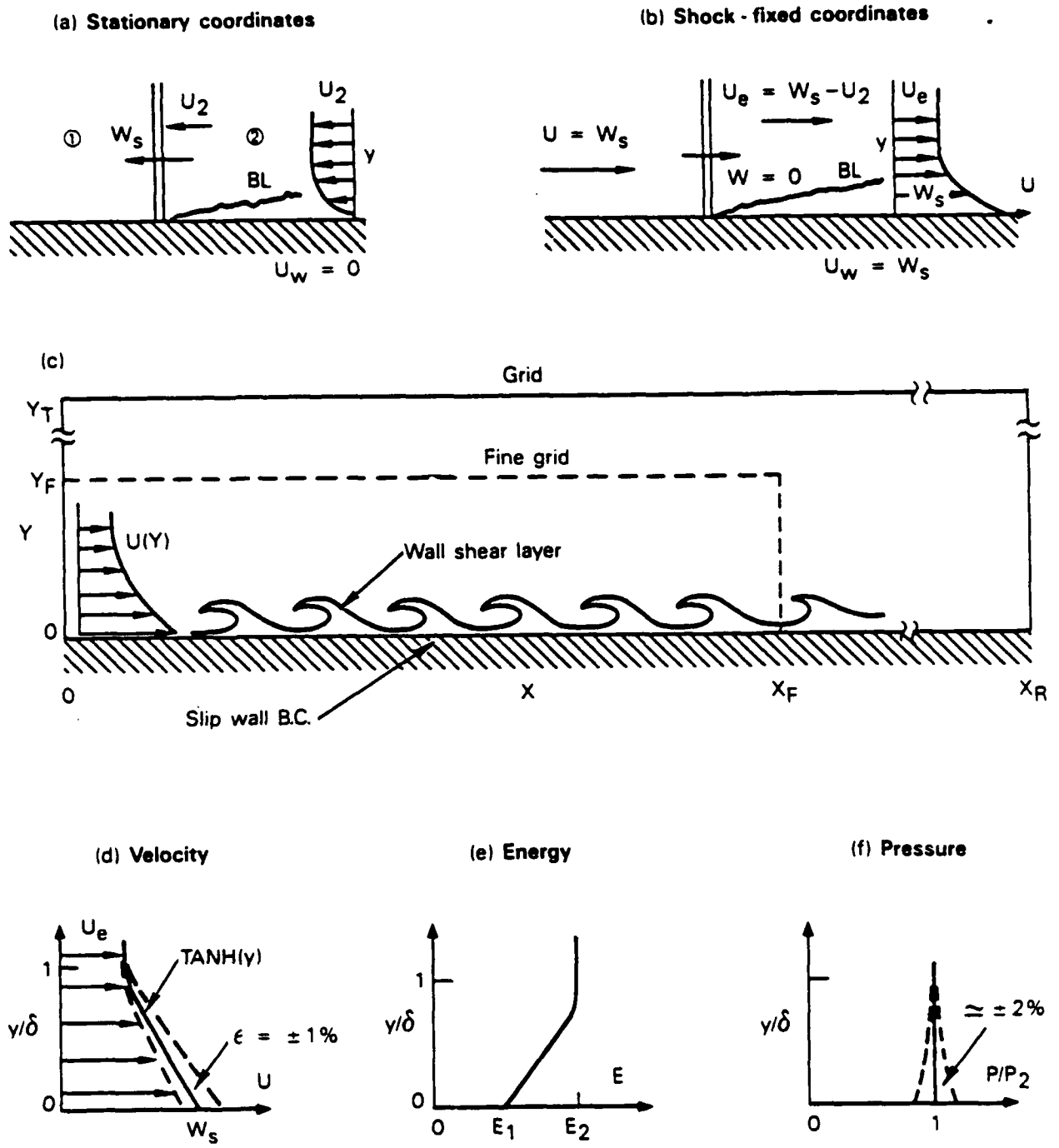

Figure 9. Schematic of the shock tube wall-shear-layer calculation: (a) and (b) shock wave and boundary layer in stationary and shock-fixed coordinates, respectively; (c) computational grid; (d), (e) and (f) wall shear layer profiles of velocity energy and pressure, respectively.

$$e(x, y, o)/e_1 = 1.22 + 0.244\ Tanh(0.5y - 1.5) \quad (22)$$

where

$$f(y) = 0.741 - 0.286\ Tanh(0.5y - 1.5) \quad (23)$$

For convenience, the flow variables were nondimensionalized by the ambient conditions denoted by subscript 1. By this formulation, $u/a_1 = M_s = 1.70$ on the wall, and $u/a_1 = 0.455\ M_s = 0.77$ in the free-stream, thereby introducing the correct amount of circulation into the flow. Similarly, $e/e_1 = 1$ on the wall and $e/e_1 = 1.46$ in the free-stream, thereby satisfying the correct temperature boundary conditions. The pressure field corresponded to the uniform state behind the shock:

$$p(x, y.o)/p_1 = 1 + (M_3^2 - 1)2\gamma/(\gamma + 1) = 3.2 \quad (24)$$

while the density profile was related to the pressure and internal energy profile by means of the equation of state:

$$\rho = p/e(\gamma - 1) \quad (25)$$

This gives a density of $\rho/\rho_1 = 3.2$ on the wall and $\rho/\rho 1 = 2.2$ in the free-stream.

The above conditions were used to initialize the flow field. The left boundary of the computational mesh was then driven with a sinusoidal perturbation on the streamwise velocity profile:

$$u(o, y, t)/a_1 = M(y, t) \qquad v(o, y, t) = 0 \quad (26)$$

$$e(o, y, t) = e(x, y, o) \qquad \rho(o, y, t) = p/e(\gamma - 1) \quad (27)$$

where

$$M(y, t) = M_S\ f(y)\left[1 = \phi(y) \sum_{n=1}^{10} \epsilon_n\ \sin \omega_n t\right] \quad (28)$$

$$\phi(y) = \begin{cases} 1 - y/\delta_o & \text{for } y \leqslant \delta_o \\ 0 & \text{for } y > \delta_o \end{cases} \quad (29)$$

By this formulation, the maximum perturbation occurs on the wall, and is zero outside the shear layer ($y > \delta_o = 7.65$) — thus modeling the physical problem as described in the previous section. The perturbation frequencies ω_n were assumed to be the same as for the free shear layer case (Eqs. 18), although it was recognized that there can be some (as yet undetermined) change in frequencies due to the influence of the wall. A maximum perturbation amplitude of $\epsilon_1 = 0.01$ (with ϵ_n from Eqs. 19), was used, corresponding to a $\pm$ 1 percent variation in shock velocity near the wall. The pressure was coupled to the local shock Mach number (Eq. 28) according to the Rankine-Hugoniot condition:

$$p(o, y, t)/p_1 = 1 + [m^2(y, t) - 1]2\gamma/(\gamma + 1) \quad (30)$$

This produced a $\pm$ 2 percent pressure perturbation near the wall.

4.3 RESULTS.

In a preliminary calculation, the inflection point was placed on the wall (y = o). After 2000 cycles, the shear layer did not roll up: instead, it merely transported the initial shear layer profile through the grid. Hence, this numerical solution satisfies the Rayleigh-Tollmien inflection point criterion which states that shear layers without an

inflection point are inviscidly stable to small perturbations.

The results of the final calculation are depicted in Figure 10. Frame (a) of that figure presents the overpressure contours near the left boundary of the mesh ($0 \leq x \leq 200$). Acoustic waves radiate from the foot of the shock, similar to those found in the experiment (Figure 8). Frames (b)-(f) depict the rollup of the shear layer into large rotational structures. The first cusp in the material interface appears between $x = 120$ and 150; by $x = 220$ the structure has rotated through one-half revolution, and a complete revolution is visible at $x = 280$. There is some evidence of incipient vortex pairing near $x = 410$, 470 and 650, but the Mode 1 response seems to predominate. By the end of the grid, the visual spreading rate is about $\delta'_{vis} = 0.015$, which agrees with the optical data of Figure 8.

Figure 11 presents a detailed view of the flow near the end of the fine-grid ($800 \leq x \leq 1000$). The material interface plot shows that the vortex cores have rotated through many revolutions. The pressure contours indicate that there is a low pressure region centered on each vortex, and a recompression region between vortices. The smoothness of the pressure contours indicates that the wall shear layer is free of shocks and basically isentropic, even though the flow is transonic. The vorticity contours show that vorticity is concentrated near the wall, but accumulated into the vortex structures. There is also a baroclinic generation of vorticity near the ends of the vortex structures, due to the entrainment of density gradient through the pressure gradient of each vortex.

The flow field along the wall ($y = 0.5$) is shown in Figure 12. The velocities and densities strongly fluctuate, even beyond the range of the wall and free-stream values. The vortices created significant pressure oscillations with peak values of as much as -22 to +8 percent of p_2.

The flow field time histories were monitored at stations $x = 400$, 600, 800 and 950. These were integrated in time over the last 1000 cycles of the calculation (about 20 periods at $x = 950$). The resulting mean-flow velocity and density profiles are depicted in Figure 13 after transformation back to laboratory-fixed coordinates (subscript o denotes free-stream conditions above the boundary layer, which correspond to state 2 behind the shock). The results have been scaled by means of the boundary thickness δ_{BL} (where $\bar{u} = 0.99\, U_\infty$):

$$\eta_{BL} = y/\delta_{BL} \qquad (31)$$

with $\delta_{BL} = 7.65$, 9.15, 10.11, 11.92 and 12.89 for $x = 0$, 400, 600, 800 and 950, respectively. This figure shows the change or evolution of the mean-flow velocity from the inflow profile (x=0) which contains an inflection point, through a transition region (x=400 to 600) where the memory of the inflow profile is fading, and finally to the asymptotic profile (x=800 and 950). This scaling seems to collapse the calculated profiles quite well in the outer region ($0.5 < \eta_{BL}$). Near the wall, the velocity in the first cell increases with increasing x. This is caused by the vortex structures which induce an enhanced velocity near the wall (even though the no-slip condition is satisfied in the initial conditions and in the boundary condition on the left of the grid). Similar comments apply to the mean density profiles. The vortices entrain hot, low density fluid near the wall, which

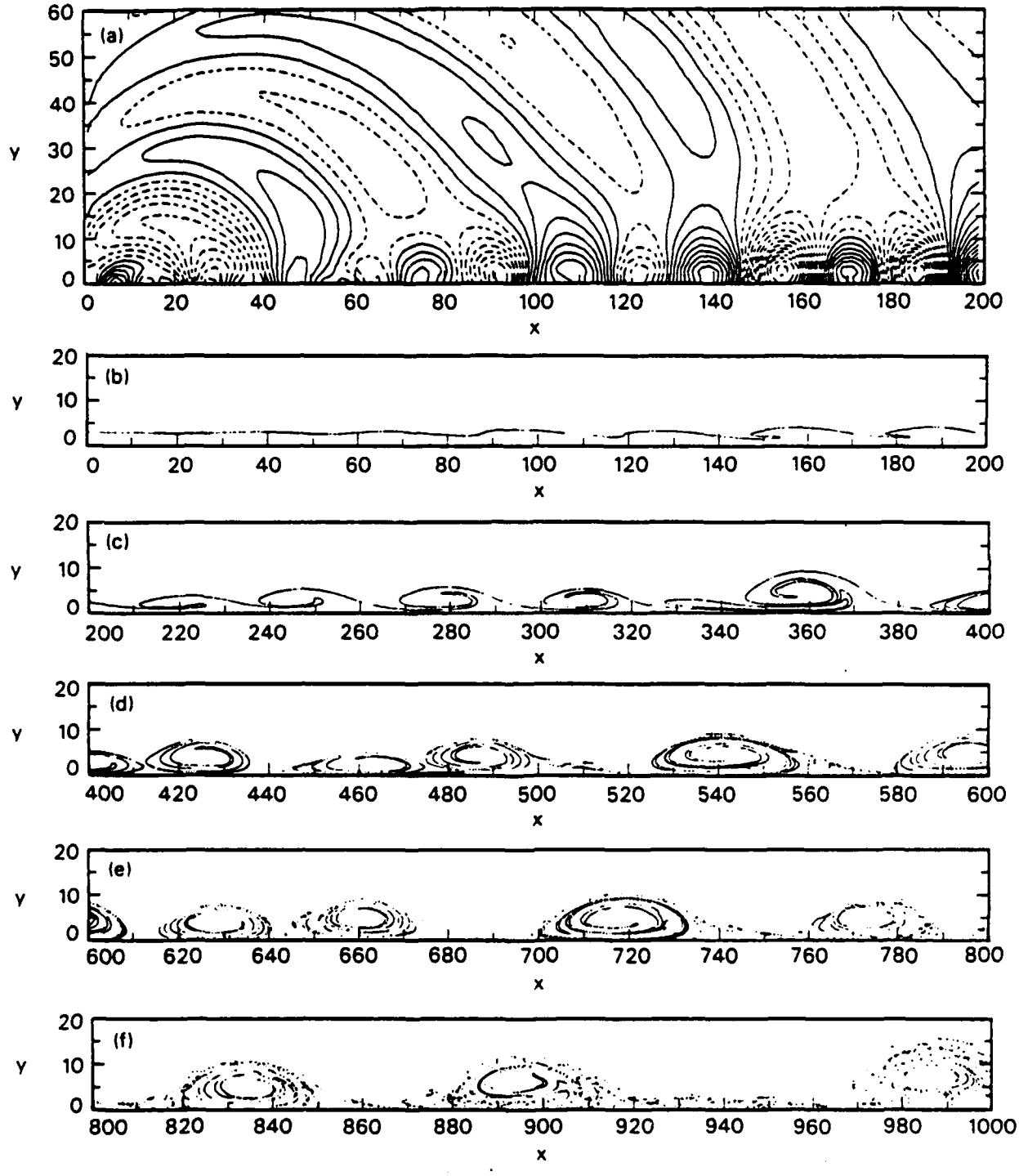

Figure 10. Calculated flow field of the development of a wall shear layer behind a shock (t = 3075): (a) Overpressure contours showing the radiation of acoustic waves from the foot of the shock (x=y=o); (b)-(f) material interface plots demonstrating the rollup of the shear layer.

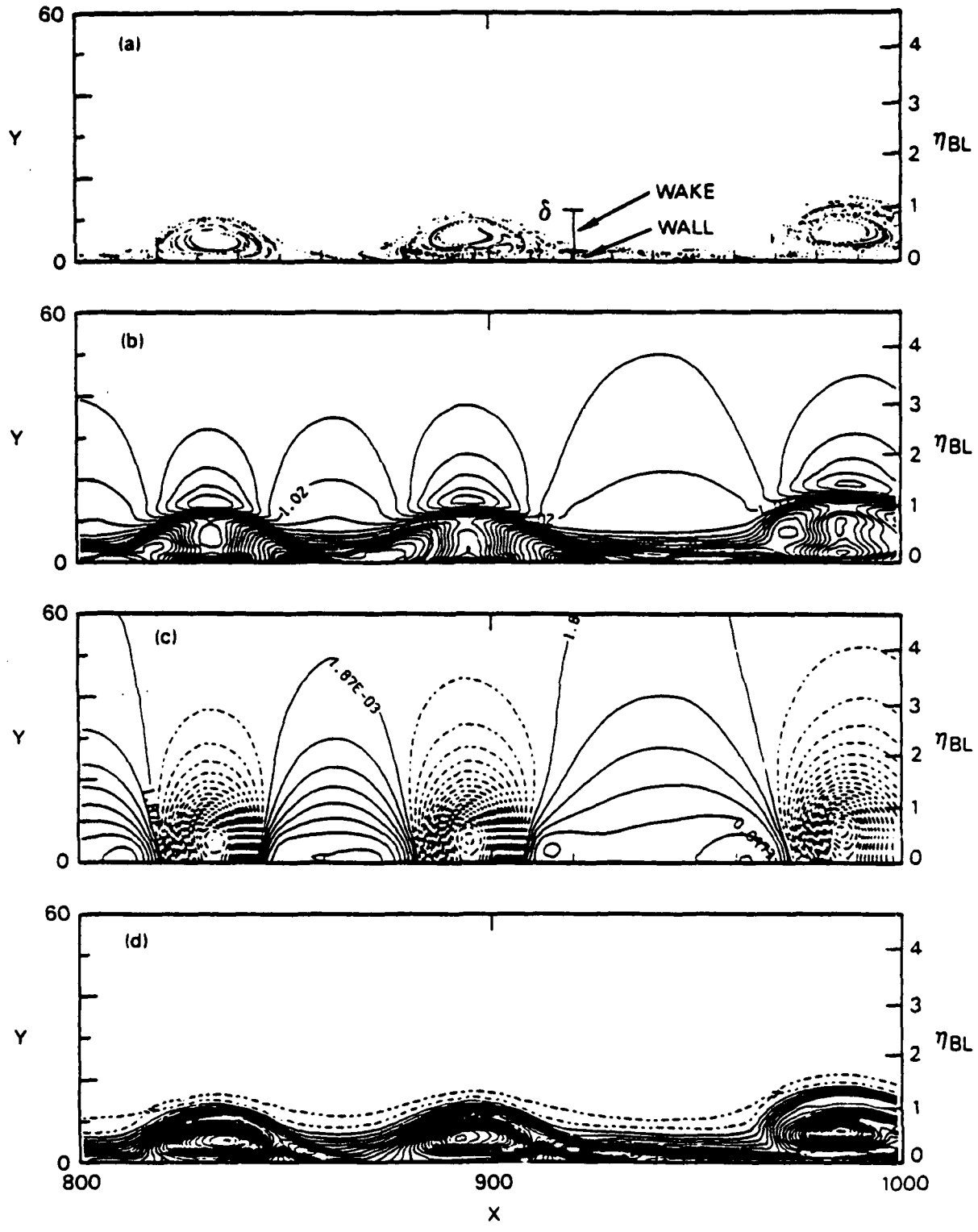

Figure 11. Expanded view of the flowfield from Figure 10 near the end of the grid: (a) material interface, showing the rollup of the layer; (b) density contours; (c) overpressure contours (solid lines correspond to positive values); (d) vorticity contours.

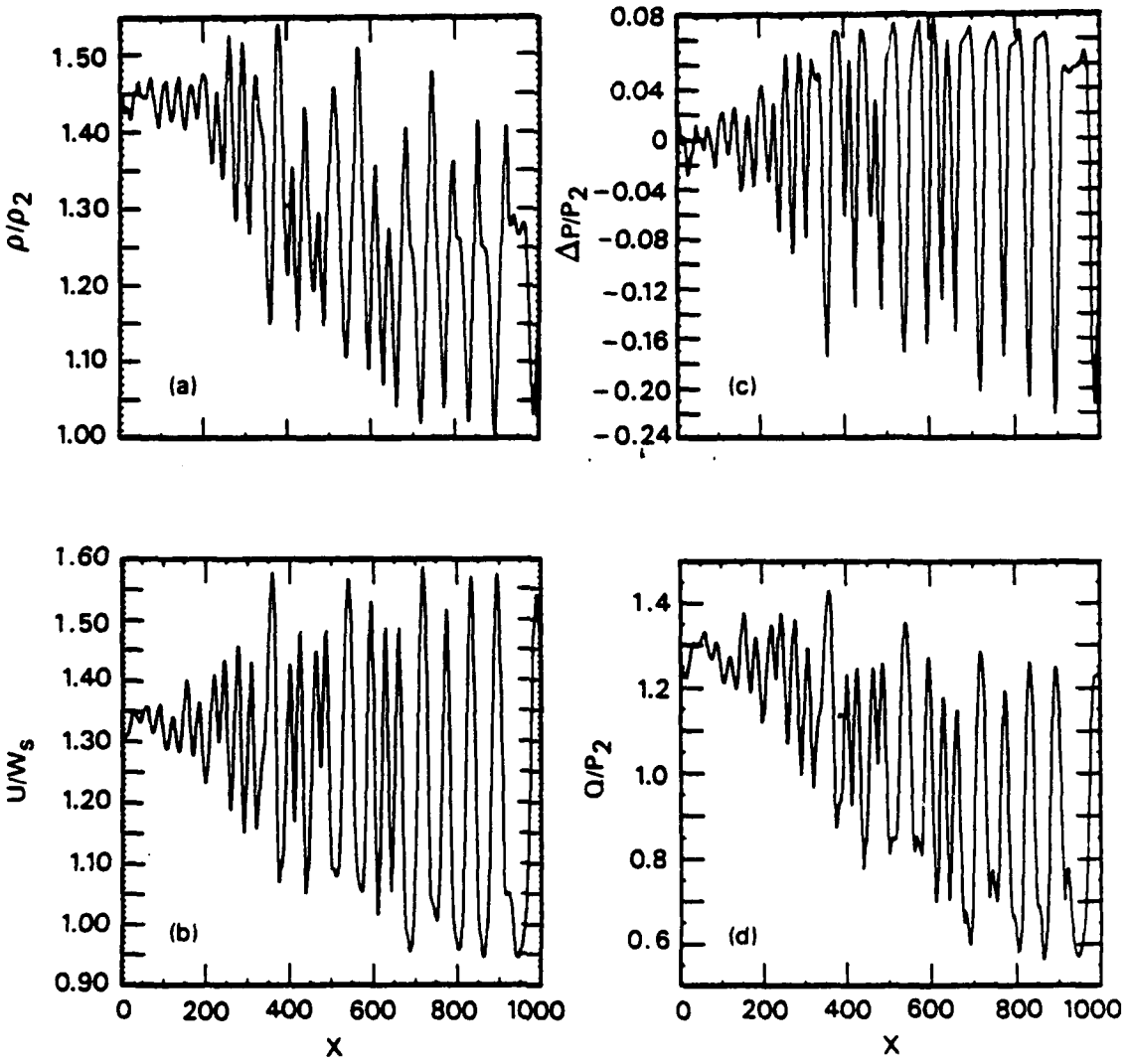

Figure 12. Flow field along the wall of the shock tube wall-shear-layer calculation at t = 3075: (a) density; (b) streamwise velocity; (c) overpressure; (d) dynamic pressure.

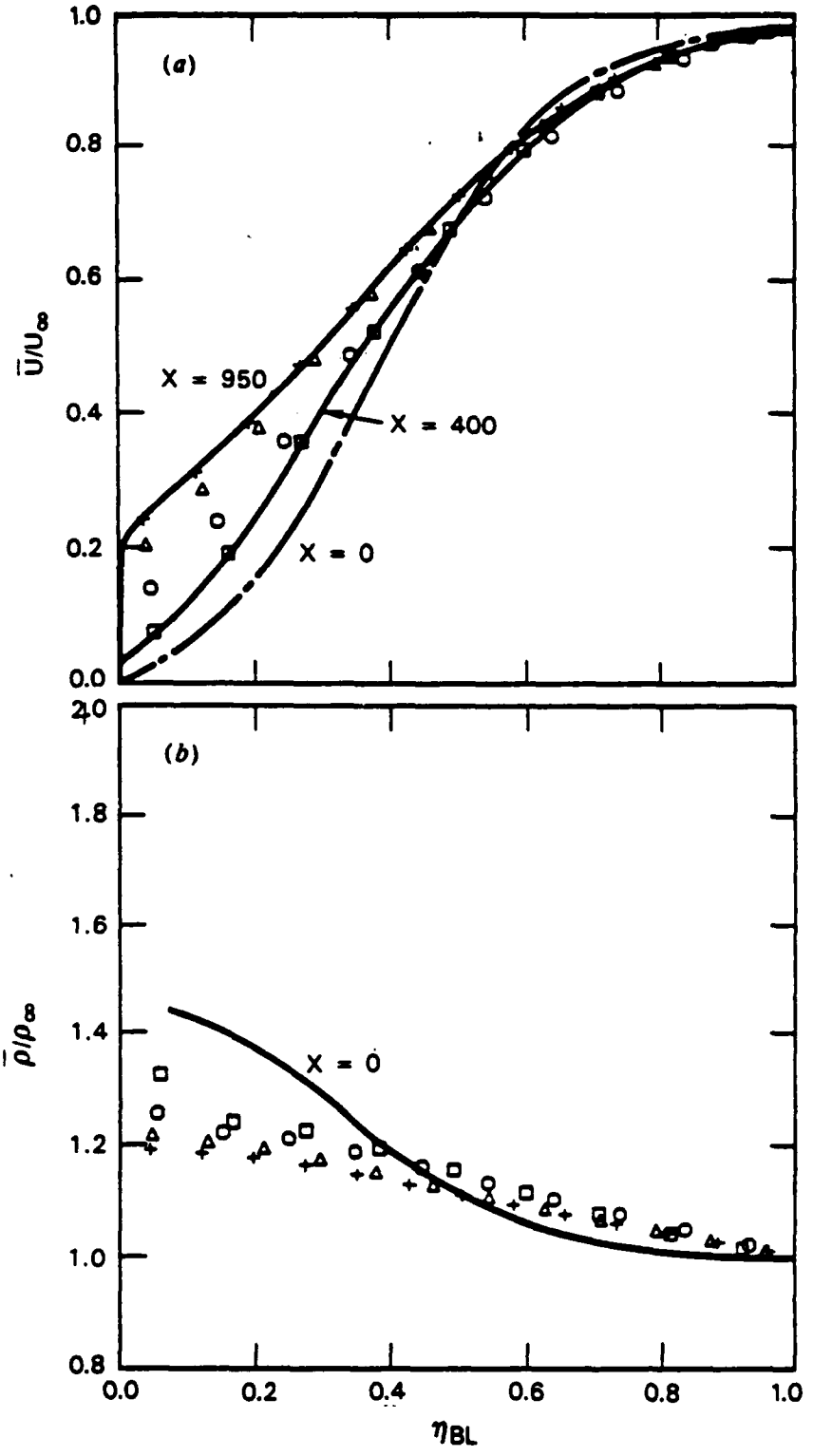

Figure 13. Mean-flow profiles of the shock tube wall-shear-layer calculation: (a) streamwise velocity profile; (b) density profile. (Symbols □, ○, Δ, and + denote stations at x = 400, 600, 800 and 950, respectively.).

causes the density in the first cell to decrease with increasing x. Clearly, to continue to satisfy the no-slip boundary condition on the wall (i.e., to accurately calculate the laminar sublayer), a viscous flow treatment with very fine zones is needed near y=o. Nevertheless, the profiles look qualitatively like a boundary layer.

Figure 14 presents the fluctuating flow profiles corresponding to Figure 13. The streamwise velocity fluctuations, u', peak near the wall and at $\eta_{BL} = 1$ (no doubt, above and below each vortex structure). The transverse velocity fluctuations, v', reach a maximum value at $\eta_{BL} \cong 0.6$ (approximately at the height of the vortex centers). Note that the fluctuating components of the flow do not approach zero at $\eta_{BL} = 1$; in fact, they extend out 3 or 4 boundary layer thicknesses. The fluctuating shear stress $\overline{u'v'}$ seems qualitatively correct, (e.g., the sign is opposite to $\frac{\partial u}{\partial y}$), and the peak value increases from station 1 to 2, and then decays at stations 3 and 4. The peak values of the fluctuating flow components are listed in Table 1. The peak density fluctuations agree very well with measurements of a hypersonic boundary layer (Owen et al., 1975). The peak shear stresses are somewhat smaller than the low-speed shear layer results.

Next, we examine whether the results of this wall shear layer calculation are consistent with known properties of turbulent boundary layers. According to experimental measurements, turbulent boundary layers may be divided into three regions: (1) a laminar sublayer, where $0 \leq \eta_{BL} < \sim 0.02$; (2) a wall region, covering $\sim 0.02 < \eta_{BL} < \sim 0.2$; and (3) a wake region extending over $\sim 0.2 < \eta_{BL} < 1$. Viscous effects play a dominant role in the laminar sublayer. In the wall region, the mean-flow velocity scales with the wall shear velocity u_τ, and has the following logarithmic dependence on y (White, 1974):

$$\bar{u}/u_\tau = \frac{1}{\kappa} \ell\eta \ (yu_\tau/\nu) + B \qquad (32)$$

where

$\kappa = 0.40$

$B = 5.5$

Note that the slope of the profile in these coordinates is related to von Karman's constant, κ. This equation may be extended to cover the wake region by adding a so-called "wake function." Coles (1956) found that a $\sin^2$ wake function gave the best correlation of a variety of turbulent boundary layer data (White, 1974); hence, Eq. (32) becomes:

$$\bar{u}/u_\tau = \frac{1}{\kappa} \ell\eta \ (yu_\tau/\nu) + B + A \sin^2 \left(\frac{\pi}{2} \eta_{BL} \right) \qquad (33)$$

where

$$A \equiv \begin{cases} 2.35 \text{ for flatplate (Schultz-Grunow, 1940)} \\ 0.65 \text{ for channel flow (Laufer, 1951)} \end{cases}$$

This formulation could not be used directly because, for example, the fluid viscosity does not exist in the present inviscid calculation. For convenience, then Eq. (33) was rescaled in terms of the free-stream velocity and η_{BL}, and the viscosity term was absorbed into constant B', yielding:

$$\bar{u}/U_\infty = m^{(\eta} \ (\eta_{BL}) + B' + A' \sin^2 \left(\frac{\pi}{2} \eta_{BL} \right) \qquad (34)$$

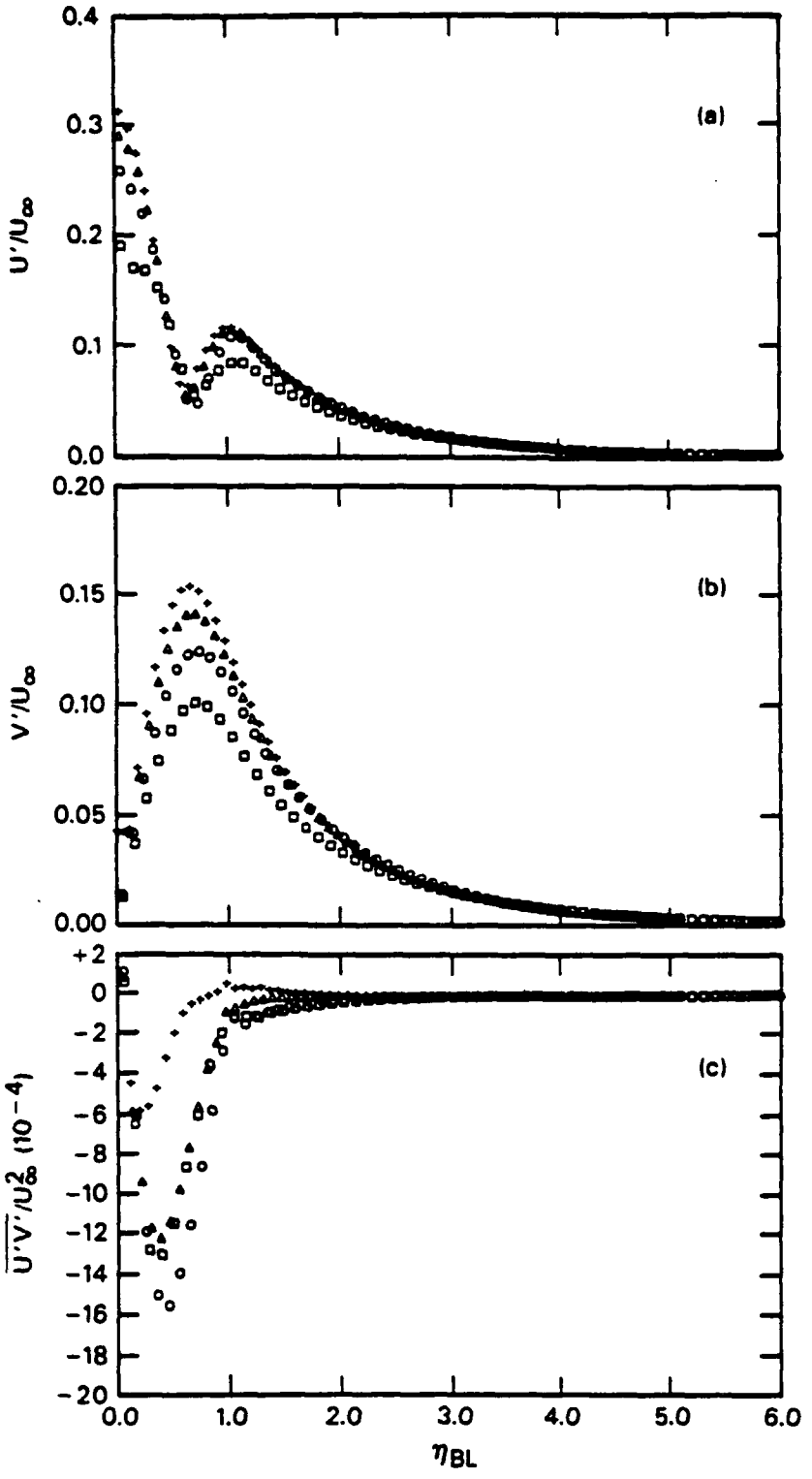

Figure 14. Time-averaged fluctuating flow profiles from the shock tube wall-shear-layer calculation: (a) streamwise velocity; (b) transverse velocity; (c) shear stress; (d) density; (e) pressure. (Symbols □, ○, Δ and + denote stations at x = 400, 600, 800 and 950, respectively.).

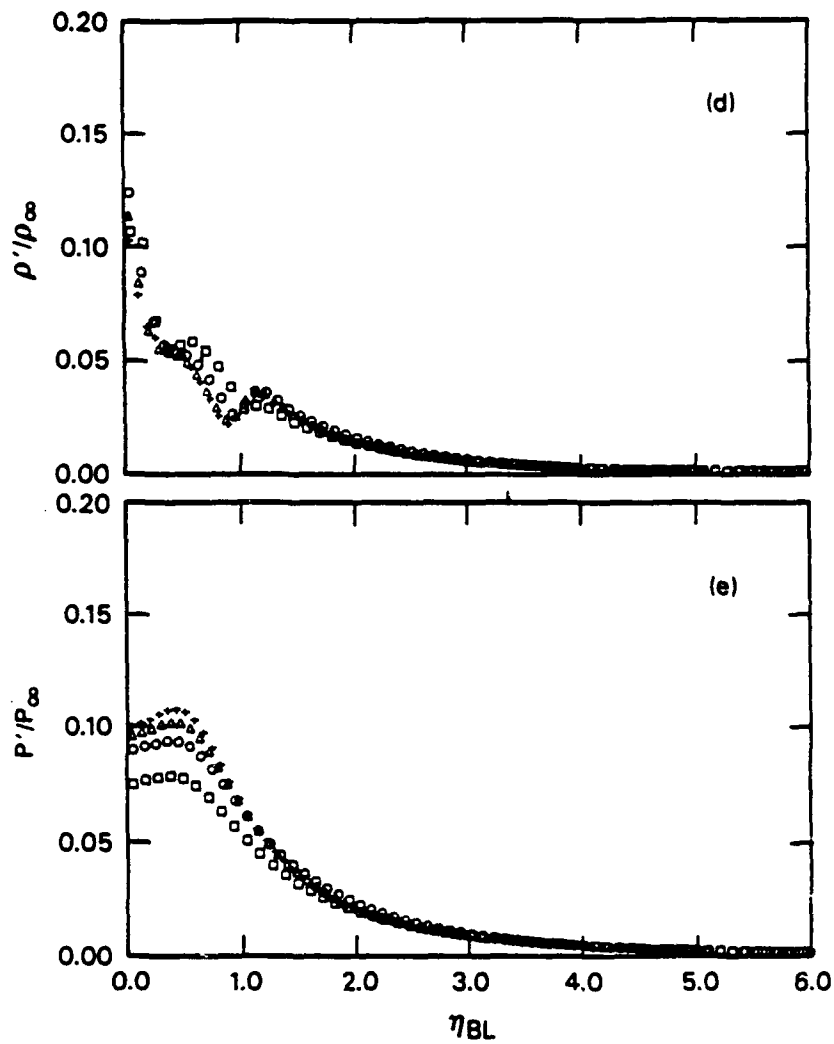

Figure 14. Time-averaged fluctuating flow profiles from the shock tube wall-shear-layer calculation: (a) streamwise velocity; (b) transverse velocity; (c) shear stress; (d) density; (e) pressure. (Symbols □, ○, Δ and + denote stations at x = 400, 600, 800 and 950, respectively.) (Concluded).

where

$$m = u_\tau / U_\infty \kappa \tag{35}$$

$$B' = \left|\frac{1}{\kappa}\right. \ell\eta(\delta u_\tau/\nu) + B\left|u_\tau/U_\infty\right. \tag{36}$$

$$A' = A u_\tau / U_\infty \tag{37}$$

Note that because of the rescaling, the profile parameters (m, B′ and A′) depend on the wall shear velocity which can vary with x. Exclusive of the viscous sub-layer, Eq. (34) should describe the mean-flow velocity profile over essentially the entire height of the boundary layer ($\sim 0.02 < \eta_{BL} \leq 1$).

For comparison purposes, the calculated mean-flow velocity profiles are replotted in Figure 15 using semi-logarithmic coordinates. In the wall region ($\eta_{BL} < 0.2$), the profiles fan out with a definite dependence on distance behind the shock. The calculated points were fit in this region with straight lines (the solid curves) shown in Figure 15, which have the logarithmic slopes m listed in Table 3.

Near the wall, it was assumed that the total shear stress was constant and equal to its peak value, hence the shear velocity u_τ can be evaluated from the definition:

$$u_\tau/U_\infty \equiv \sqrt{|\overline{u'\,v'}|_{max}/U_\infty^2} \tag{38}$$

This, in turn, can be used to evaluate the local skin friction coefficient, c_f, according to:

$$c_f = 2\left(\frac{\rho_w}{\rho_\infty}\,\frac{u_\tau}{U_\infty}\right)^2 \tag{39}$$

Table 3. Boundary Layer Parameters for the Shock Tube Case.

x	δ_{BL}	Wall Values $-\overline{u'\,v'}/U_\infty^2$	Wall Values u_τ/U_∞	Wall Values C_f (10^{-3})	Profile Parameters m	Profile Parameters B′	Profile Parameters A′	Profile Parameters κ
0	7.65	—	—	—	—	—	—	—
400	9.15	0.0013	0.0360	3.5	0.106	0.3691	0.6209	0.338
600	10.11	0.0016	0.0400	4.0	0.0910	0.3984	0.5916	0.439
800	11.92	0.0012	0.0346	2.9	0.0755	0.4336	0.5564	0.456
950	12.89	0.00059	0.0243	1.4	0.0628	0.4343	0.5557	0.387

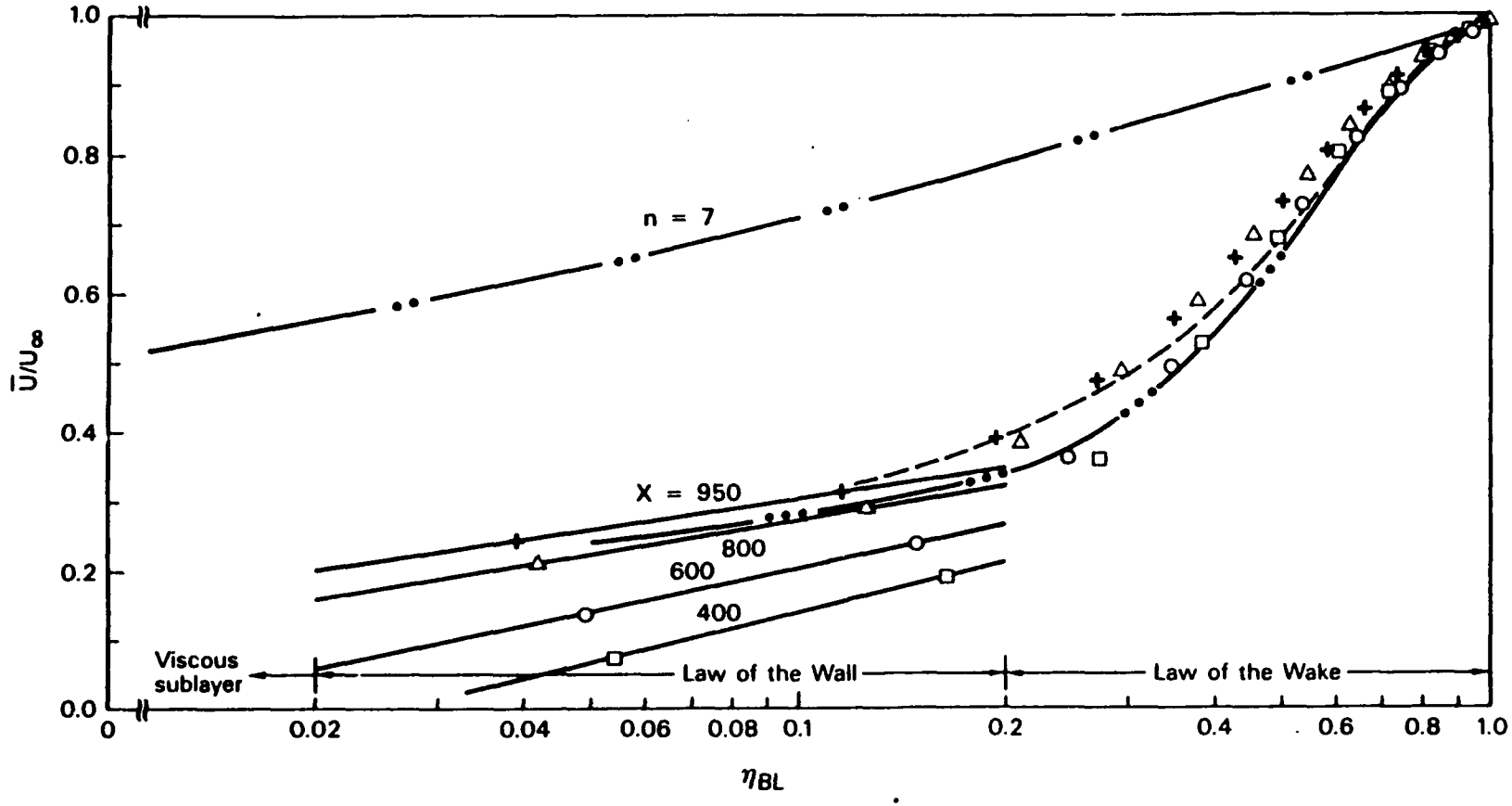

Figure 15. Mean-flow velocity profiles of the shock tube wall-shear-layer calculation, demonstrating the Law of the Wall behavior (straight lines) and the wake region (dashed curve, Eq. 34) of the profiles. (Symbols □, ○, Δ and + denote stations at x = 400, 600, 800 and 950, respectively.) The double-chain-dashed curve denotes the n = 7 power function profile for a flat plate. The triple-chain-dashed curve represents a boundary layer profile with an adverse pressure gradient, as measured by Schubauer and Spangenberg (1960).

The local skin friction coefficients evaluated from this calculation are listed in Table 3; they vary between values of 1.4 to 4 x 10^{-3} which are in excellent agreement with smooth-wall, turbulent boundary layer measurements (1.5 to 3 x 10^{-3}) of Martin (1958).

Given the logarithmic slope and the shear velocity, one can solve Eq. (35) for the von Karman constant:

$$\kappa = u_\tau / U_\infty \; m \qquad (40)$$

The "von Karman constants" so evaluated from the calculated velocity profiles are listed in Table 3. They vary between values of 0.34 to 0.46 (with a mean value of 0.405) — which is in excellent agreement with the published values of 0.40 and 0.41. In other words, the calculated mean-flow velocity profiles (specifically, the combination of the slopes of these curves and their shear velocities) are consistent with logarithmic profiles associated with turbulent boundary layers in the wall region.

Figure 15 also shows that in the outer region of the boundary layer, the calculated points tend to converge to a single profile [i.e., $\bar{u}/U_\infty = f(\eta_{BL})$] which is basically independent of distance behind the shock front. The dashed curve in that figure represents Eq. (34) for x = 950 (constants A′ and B′ were evaluated at η_{BL} = 1 and 0.1). The calculated profiles have the same shape as the wake curve, with the maximum differences being less than 8 percent. This agreement is quite good, considering that the $\sin^2$ function is an approximation to a variety of incompressible boundary layer data. In other words, the calculated mean-flow velocity profiles are consistent with the wake profiles associated with turbulent boundary layers.

According to Schlichting (1968), the mean-flow velocity profile associated with turbulent boundary layers can be approximated by a power function:

$$\bar{u}/U_\infty = 0.99(\eta_{BL})^{1/n} \qquad (41)$$

where $\eta_{BL} = y/\delta_{BL}$. The value n = 7 correlates turbulent boundary layer data for flat plates with zero pressure gradient. This profile is depicted in Figure 15 as a double-chain-dashed curve. It gives considerably fuller profiles (e.g., $\bar{u}/U_\infty \approx 0.6$) near the wall than the present calculation ($\bar{u}/U_\infty \approx 0.1$ to 0.2).

Previously Mirels (1956) reasoned that the turbulent boundary layer behind a shock wave should be similar to the turbulent boundary layer on a flat plate, and thus he *assumed* that n = 7 power function profile applied to the shock tube case. The present wall shear layer calculation, however, indicates that mean-flow velocity profile for the shock tube case does not follow this n = 7 power function — instead, it resembles the boundary layer profiles measured for cases with adverse pressure gradients. The triple-chain-dashed curve in Figure 15 represents such data of Schubauer and Spangenberg (1960), and it can be seen that present calculations are very similar to their measured profile. Hence, it is logical to ask: Which is the correct profile for a boundary layer behind a shock wave? In other words, are the profiles of the present results an artifice of the calculational method, or are they real? Accurate, experimentally-measured profiles (e.g., by means of laser-doppler velocimetry) could answer this question; unfortunately, such

data is not available.[3] Instead, we shall address this question indirectly by considering a boundary layer case that has a plethora of velocity-profile data — namely, the tripped flat plate case. This is described in the following section.

4.4 TRIPPED FLAT PLATE CASE.

Consider a two-dimensional, laminar boundary layer developing along a smooth flat plate in the absence of any external pressure gradient. The Mach number of the free-stream flow above the boundary layer is taken as $M_\infty = 0.2$, so that the flow is nearly incompressible. Then, assume that a geometric protuberance is located on the smooth wall. This protuberance causes two physical effects: (1) it creates an inflection-point in the streamwise velocity profile; and (2) the Strouhal shedding frequency of its wake perturbs the wall layer, thus leading to a "turbulent" boundary layer flow.

The development of the fluctuating flow downstream of this disturbance was simulated numerically by the high-order Godunov code. The computational grid used was identical to that of the shock tube case. The flow field was initialized with a uniform density ($\rho = 1$) and pressure ($p = 17.86$) field. The wall shear layer was modeled by a Tanh(y) streamwise velocity profile:

$$u(x, y, o)/U_\infty = f(y) \qquad (42)$$

$$= 0.5[1 + Tanh(0.5y - 1.5)] \quad v(x, y, o) = 0$$

Note that by construction, $u = 0$ on the wall thereby satisfying the no-slip condition, while in the free stream $u = U_\infty$. The pressure was chosen so that the free stream Mach number was $M_\infty = 0.2$. The inflection point and the initial tracer particles were located at $y = 3$.

The left boundary of the grid was driven with the same flow field with a sinusoidal perturbation on the streamwise velocity:

$$u\ (o, y, t)\ /U_\infty$$

$$= f\ (y)\ \left[1 + \phi(y) \sum_{n=1}^{10} \epsilon_n\ \sin\ \omega_n t\right] \qquad (43)$$

$$\phi\ (y) = |1 - f\ (y)| \qquad (44)$$

with $\epsilon_1 = 0.10$. Note that by means of Eq. (44), the perturbations reach a maximum value ($\approx 0.025\ U_\infty$) at about half the height of the shear layer and are zero outside this region.

The calculation was run 10^4 cycles to eliminate transients from the start-up process and to build up data for analyzing the mean-flow profiles. The flow field at the end of the calculation ($t = 3617$) is depicted in Figure 16. The tripped wall shear layer rolled up into large rotational structures similar to the shock tube calculation, except in this case the structures rotated in a clockwise direction. The material interface plots (Fig. 16 a,b,c) show that the first cusp appears at $x \approx 40$, and the vortex structure has rotated through one-half a revolution at $x \approx 55$. By $x \approx 90$ the vortices are well-formed and have rotated through one revolution. Two cores are seen in the vortices at $x = 210$, 320 and 430 (i.e., every other vortex), thus indicating a Mode II pairing, but multiple merging did not seem

3. Martin (1958) did report velocity profiles for a boundary layer behind a shock. However, these velocities were not measured directly but were inferred from interferometric measurements of density profiles by use of the Crocco relation. This relation is valid only along streamlines and cannot be applied in turbulent boundary layers because of the large-scale rotational structures.

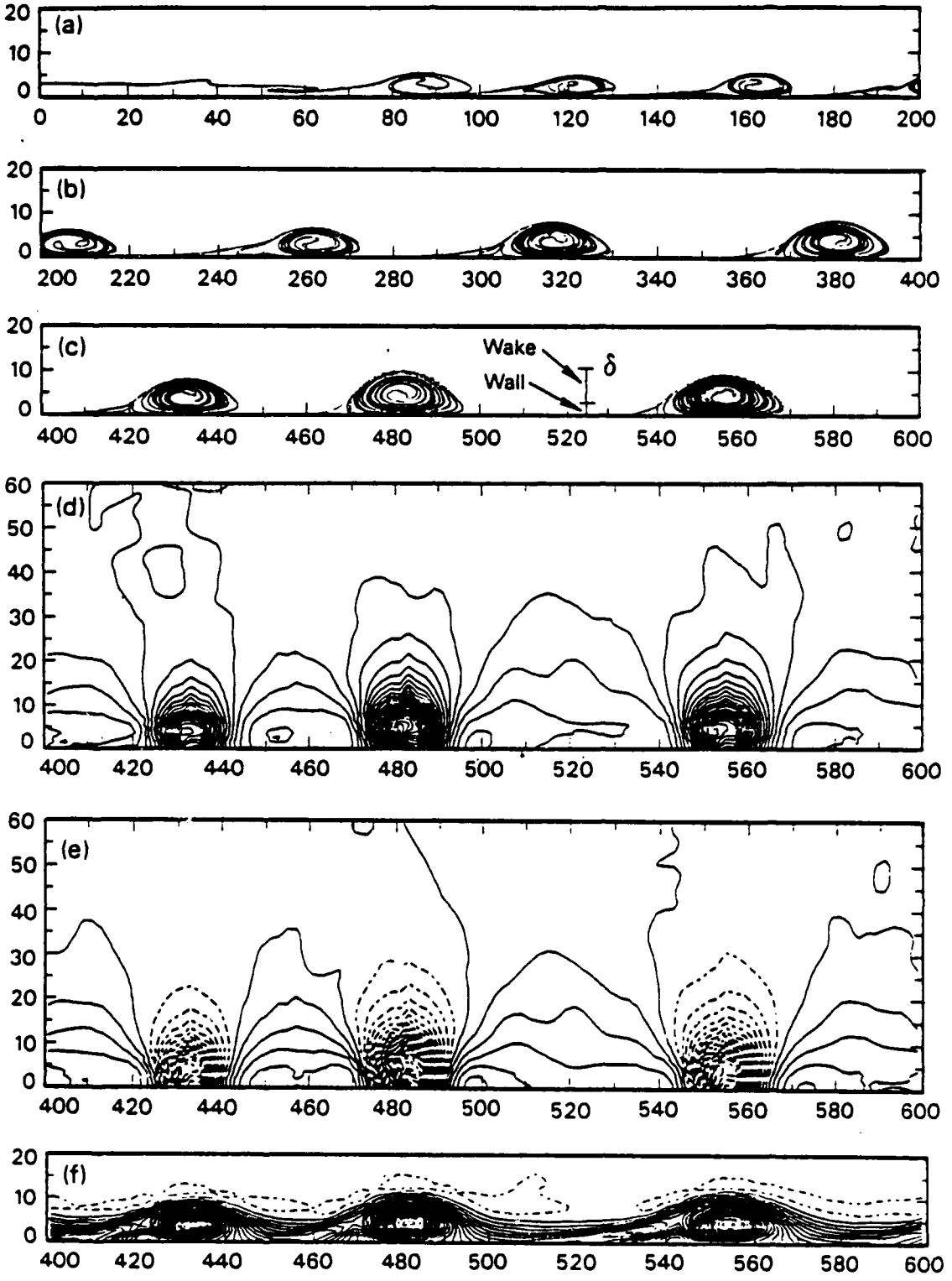

Figure 16. Flow field of the tripped flat plate calculation (t = 3617): (a), (b), (c) are material interface plots showing the rollup of the layer; (d), (e) and (f) represent contour plots of density, overpressure and vorticity, respectively.

to occur even though the first ten perturbation frequencies were used. Also shown in Figure 16d,e,f are the density, overpressure and vorticity plots corresponding to Figure 16c. The maximum pressure and density variations are less than one-half percent for this low speed flow.

Clearly, this calculation captures only the largest-scale rotational structures that are essentially independent of Reynolds number. Small-scale vortices, which should be embedded in the large rotational structures, and which are, no doubt, Reynolds number dependent (e.g., as found in the Brown and Roshko free shear experiments), are not resolved on this grid.

The flow field was monitored at stations x = 400, 600, 800, 950. This data was integrated over the last 4000 cycles to establish the time-averaged profiles. The resulting mean-flow, streamwise velocity profiles are presented in Figure 17. The profiles are qualitatively similar to the previous calculation in that they converge to a single profile in the wake region and exhibit a logarithmic behavior in the wall region. Now, however, the magnitudes of the velocity are very similar to those obtained from the n = 7 power function profile depicted as the chain-dashed curve. No doubt, the flow at station x = 400 is transitional.

The calculated profiles were fitted with the Coles boundary layer function (Eq. 34), and the profile parameters are listed in Table 4. The von Karman constants inferred from these fits ($0.37 \leq \kappa \leq 0.50$) are quite reasonable. Comparing with available experimental data (Table 4), we find that local skin friction coefficients are too small by a factor of 6, and the associated shear velocities are too small by a factor of 2.5. Wieghardt and Tillman (1944) have performed some of the most detailed and extensive measurements of mean velocity profiles for a tripped, turbulent boundary layer on a flat plate: this set of data is compiled in Coles and Hirst (1969). Two of these stations, x = 79cm (profile 1400-10) and x = 499cm (profile 1400-26), which cover the x/δ range of the numerical simulation, are shown in Figure 17. The dashed curves on that figure represent the Coles boundary-layer-function fits to that data, e.g.,

$$\bar{u}/U_\infty = 0.0779 \ln \eta_{BL} + 0.849 + 0.141 \sin^2\left(\frac{\pi}{2}\eta_{BL}\right) \quad (45)$$

for station x = 79cm. This data may be used to evaluate the accuracy of the calculation.

Comparing the solid curve of the calculation (x = 600; x/δ = 57) with the lower dashed curve (Eq. 45) representing the Wieghardt and Tillmann data (x = 79cm; x/δ = 56), one sees that the two curves are identical—except for the first calculated point. Similar conclusions apply to the two downstream stations; outside the first row of cells, the calculated velocities agree very well with the data (e.g., less than 4 percent difference). In the first row of cells, however, the calculated velocities are 7 to 14 percent too large, probably because viscous losses near the wall are not included in the calculation (e.g., the viscous sublayer extends to approximately 20 percent of the height of the first row of computational cells, and large momentum losses in this sublayer due to viscosity could decrease the cell-averaged momenta in these cells by as much as 20 percent).

The root-mean-squared flow fluctuations were also evaluated for this case. They are compared with the hot-wire anemometry measurements of Klebanoff (1955) in Figure 18 (dashed curves), and the peak

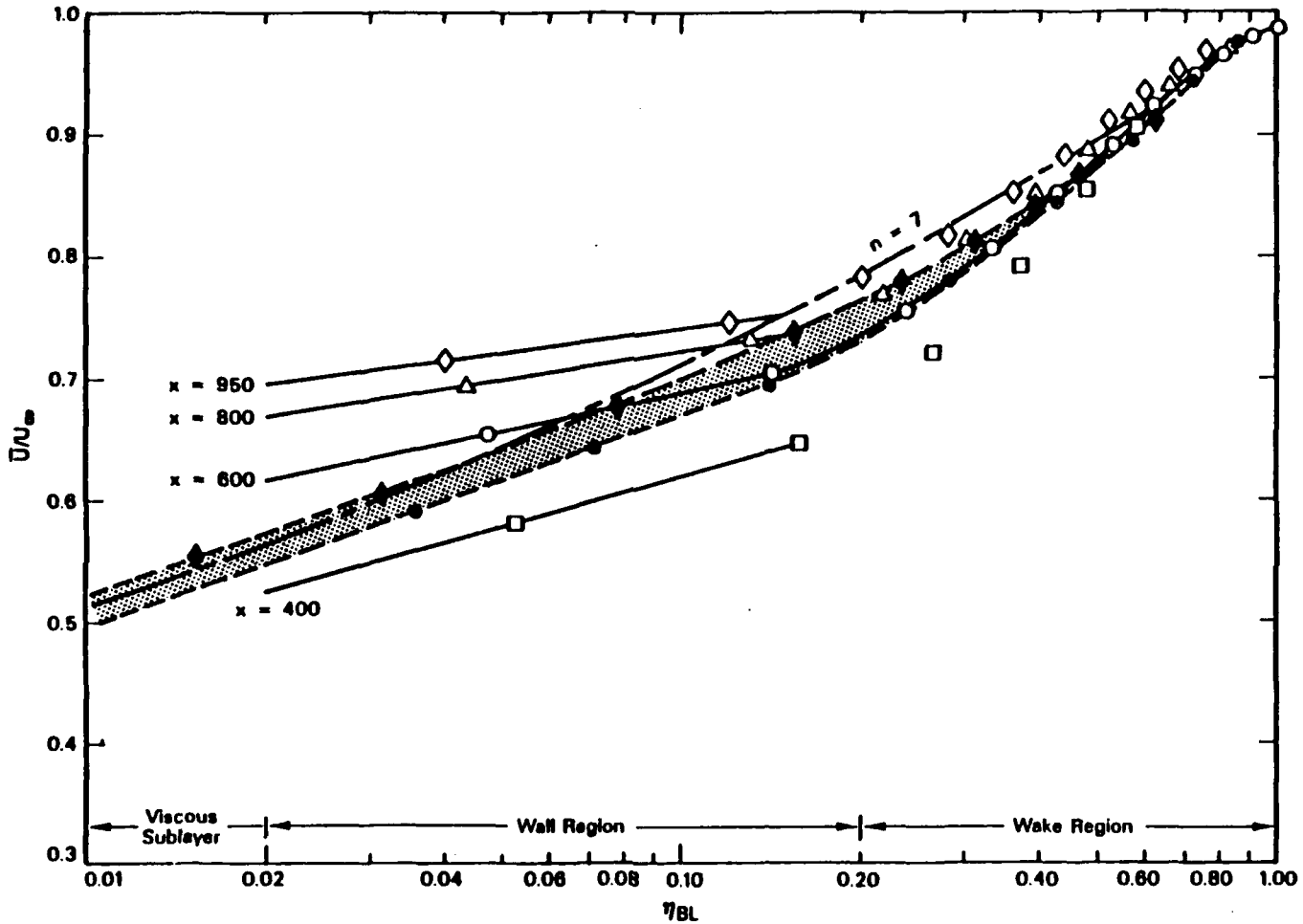

Figure 17. Mean-flow velocity profiles of the tripped flat plate case. Symbols □, ○, Δ, and ◇ denote calculation stations at x = 400, 600, 800 and 950, respectively. The chain-dashed curve represents the n = 7 power function profile (Eq. 41). The dashed curves denote the Coles function fits of the tripped flat plate data of Wieghardt and Tillmann (1944): symbols • and ◆ denote data stations at x = 79 cm (profile 1400-10) and x = 499 cm (profile 1400-26), respectively.

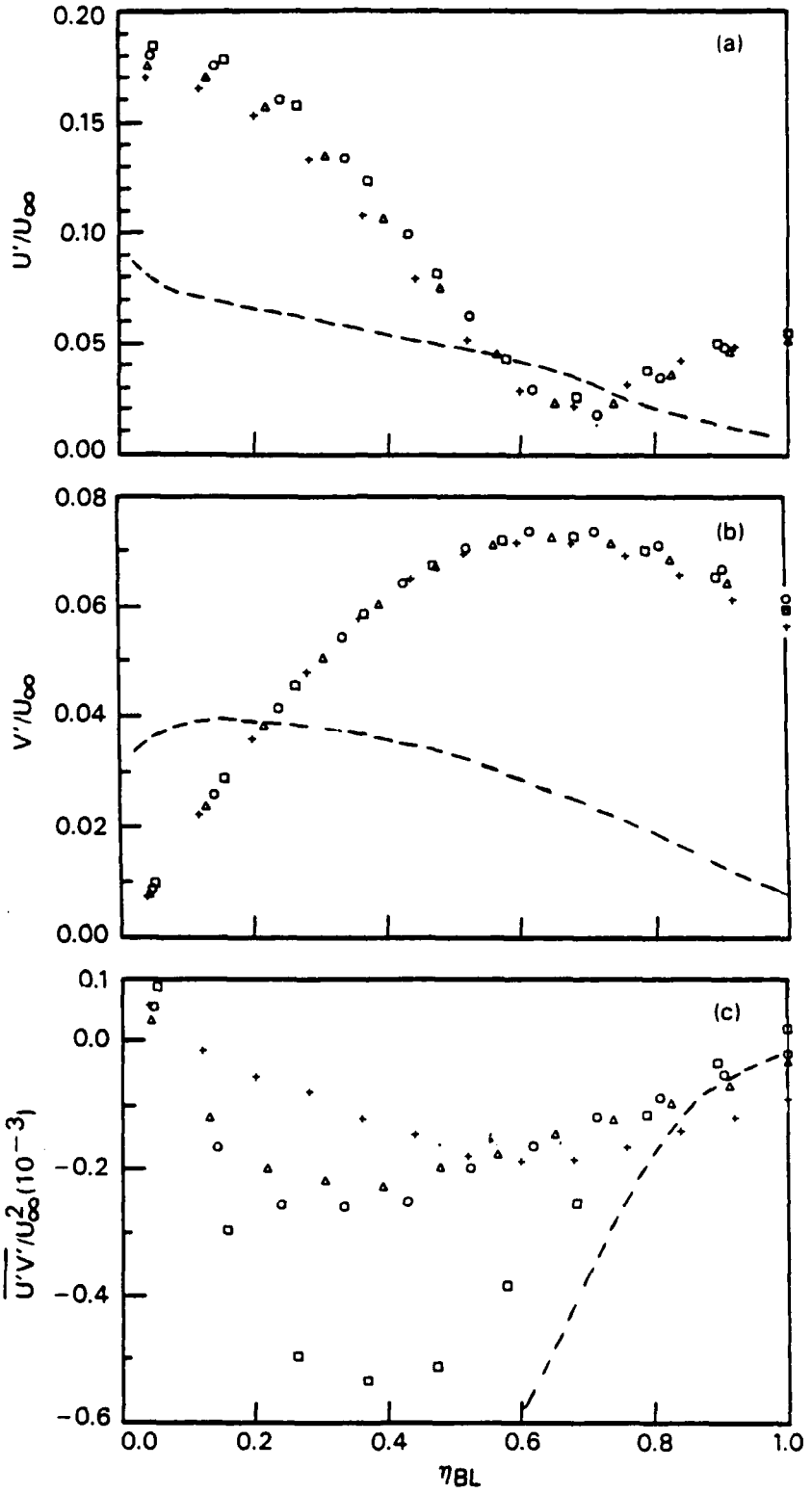

Figure 18. Time-average fluctuating flow profiles from the tripped flat plate calculation: (a) streamwise velocity; (b) transverse velocity; (c) shear stress: (Symbols □, ○, Δ, and + denote stations at x = 400, 600, 800 and 950,respectively). Dashed curves represent the data of Klebanoff (1955).

Table 4. Boundary Layer Parameters for the Tripped Flat Plate Case.

Stations			Wall Values			Profile Parameters			
x	δ	x/δ	$-\overline{u'v'}/U_\infty^2$ (10^{-3})	U_τ/U_∞	c_f' (10^{-3})	m	B′	A′	κ
Calculation									
0	7.65	0	--	--	--	--	--	--	--
400	9.5	42	0.531	0.0230	1.06	0.0619	0.763	0.227	0.37
600	10.5	57	0.259	0.0161	0.518	0.0428	0.789	0.201	0.38
800	11.5	70	0.226	0.0150	0.452	0.0319	0.797	0.193	0.47
950	12.5	76	0.186	0.0136	0.372	0.0273	0.806	0.184	0.50
Wieghardt & Tillmann(1944)									
79cm	1.41cm	56	1.59[a]	0.0398	3.17	0.0779	0.849	0.141	0.51
499cm	6.45cm	77	1.22[a]	0.0349	2.43	0.0783	0.880	0.110	0.45
Klebanoff (1955)			1.38[a]	0.0371	2.75	--	--	--	--
Schlichting (1968) (Eq. 21.12:Rex = 1.9×10^7)			1.04[a]	0.0322	2.07	--	--	--	--

[a]Evaluated from Eq. 38

values are listed in Table 1. From these comparisons it is obvious that th. r.m.s. flow fluctuations are predicted quite poorly by the present calculation, even though the mean profiles are in good agreement with the data. Presumably this is because fine-scale vortices, which should be embedded within the large rotational structures, are not resolved in this calculation and because three-dimensional effects are not included.

4.5 SUMMARY.

We conclude that this tripped flat plate calculation qualitatively simulates some of the features found in the wake region of turbulent boundary layers on flat plates. The calculated mean-flow velocity profiles agree with the data of Wieghardt and Tillmann, except for the first row of cells on the wall. This agreement with data implies that our calculated profiles are neither fortuitous nor an artifice of the numerical simulation, and that the calculation qualitatively represents the largest fluid-dynamic features resolvable on the computational grid.

The above comparisons offer aposteriori evidence that the velocity profiles of the shock tube calculation are also qualitatively

correct. The large-scale features of the flow field (e.g., the formation of discrete density and vortex structures, the generation of acoustic waves at the foot of the shock front, and the visual spreading rate) agree with the available shock tube data. The mean-flow velocity profiles exhibit a log(y) velocity distribution near the wall, while in the outer region the profiles collapse to a single curve that behaves like the wake function of a turbulent boundary layer. Hence, it appears that the turbulent boundary layer profile behind a shock (e.g., Fig. 15) is distinctly different from the flat plate case (e.g., Fig. 17). Perhaps this difference is related to the slope of the mean velocity profile ($\partial\overline{u}/\partial y$), which is negative for the shock tube case (in shock-fixed coordinates) and positive for the flat plate case.

Referring back to Figures 11a or 16c, it can be seen that the logarithmic velocity region near the wall is simply the time-averaged velocity field induced below each vortex, while the wake profile corresponds to the time-averaged velocity field within and above each vortex structure. In other words, the fluctuating flow associated with turbulent boundary layers is merely the evolution of a perturbed but unstable wall shear layer. This concept is not new; it has been expressed by Coles (1969), and others.

These wall-shear-layer calculations capture only the largest-scale, inviscid rotational structures. Small-scale vortices (which may depend on the Reynolds number) will be shed from the wall and entrained into the large rotational structures, but a much finer computational grid would be required to resolve such effects. Viscous forces must be included to correctly model the laminar sublayer. Eventually the boundary layer will develop three-dimensional vortex structures, and accurate numerical simulations must also include these effects. Nevertheless, the above agreement with data indicates that such features as the mean-flow velocity profiles are dominated by two-dimensional inviscid effects over most of the boundary layer (e.g., $0.1 < \eta_{BL} \leq 1$).

SECTION 5

WALL JET CALCULATION

The final case considered is a numerical simulation of a low-speed wall jet propagating into a quiescent fluid, similar to the water tunnel experiments of Bajura and Catalano (1975). The calculation dramatically demonstrates the strong coupling between the dynamics of the free shear layer on top of the jet and the wall boundary layer below the jet.

5.1 FORMULATION.

The calculation was performed on a grid with a fine-zoned region of 200 x-cells by 80 y-cells. ($\Delta x=\Delta y=1$), as shown schematically in Figure 19. Expanding cells were used above and to the right of the fine-zoned region, resulting in a total domain of 8500 by 1500. An inviscid (i.e., slip wall) boundary condition was employed along the wall, while an outflow boundary condition was used at the right edge of the grid.

The flow field was initialized with a wall jet velocity profile consisting of a Tanh(y) profile for the free shear layer portion and a Polhausen profile representing the wall boundary layer:

$$u\ (x, y, o)$$

$$= \begin{cases} 0.5\ U_J\ [1 - Tanh(y - 17)] & \text{for } y \geq 5 \\ 2\ U_J\ \xi\ [1 - \xi^2 + 0.5\ \xi^3] & \text{for } y < 5 \end{cases}$$

$$v(x, y, o) = 0 \qquad (46)$$

where

$$U_J = 2$$

$$\xi = y/\delta_o$$

The initial shear thicknesses were $\delta_o = 5$ and 6 on the wall and free shear layers, respectively. The center line of the free shear layer was at $y = 17$ ($\equiv H$). The jet was initialized with uniform thermodynamic properties:

$$\rho = 1;\ p = 71.4;\ e = 179.$$

The pressure was selected so that the peak value of the Mach number of the jet was $M_J = 0.2$.

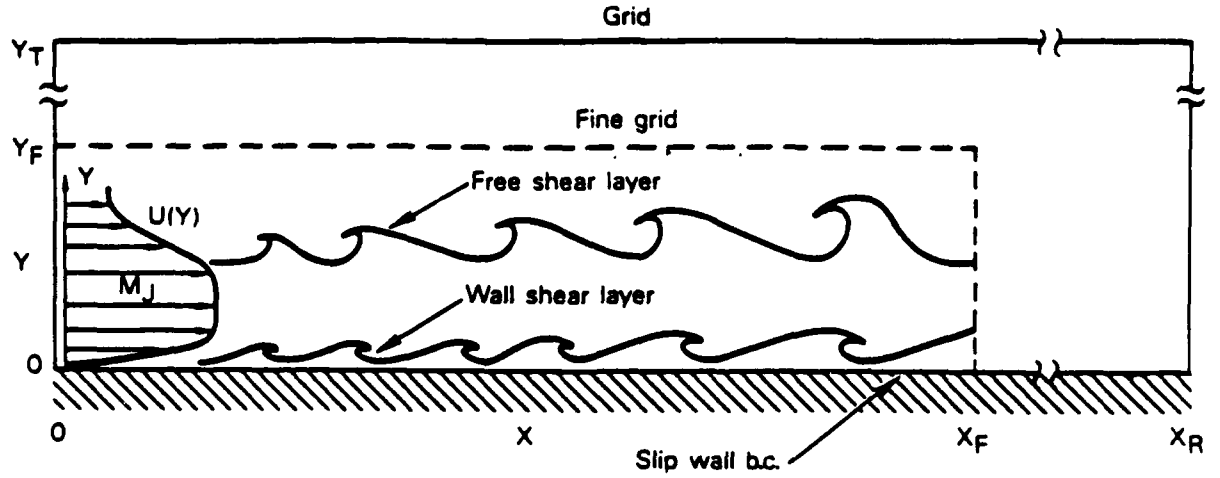

Figure 19. Schematic of the wall jet calculation.

The left boundary of the grid was driven with the same wall jet profile, using a sinusoidal perturbation on the streamwise velocity component (Eq. 15). The first ten modes were employed, with a maximum perturbation amplitude of $\epsilon_1 = 0.01$. Material lines, initially located at the inflection point of the free shear layer ($j = 17$) and in the boundary layer ($y = 2$), were tracked to follow the interactions of the two shear layers.

5.2 RESULTS.

The calculation was run 8000 cycles. Figure 20 presents a series of frames of the calculated material interface shapes covering one complete period during the calculation. The merging patterns are quite different from those found in the above-described shear layer calculations (due to differences in λ, r and λ_ρ). In general, the free shear layer becomes unstable first[4], and forms positive vortex structures (labeled sequentially with cardinal numbers). Induced velocities from these structures cause the wall shear layer to become unstable, and form negative vortex structures (labeled sequentially with capital letters), that explode off the wall. This behavior is qualitatively similar to that found in the wall jet experiments of Bajura and Catalano (1975). Large-scale structures from the two shear layers interact and pair, thus creating a von Karman-type vortex street of alternating positive and negative vortex structures.

The following is a detailed description of this process. Frames (a) through (g) of Figure 20 show the formation of structure 1-2-3-4. Vortices 1 and 2 pair and merge, and induce the rollup of vortex A on the wall (frames a and b). Structure 1-2 entrains vortex 3 from below (frames c and d). Vortex 4 triggers the creation of vortex B on the wall (frames d and e). Then structure 1-2-3 entrains vortex 4 from below, which causes the merger of wall vortices A-B (frames e and f). Finally, the large-scale structure 1-2-3-4 interacts with the structure A-B, causing it to explode off the wall (frame g). These structures (1-2-3-4 and A-B) then interact to form the first pair of a von Karman-type vortex street which passes off the grid. The creation of structure 1-2-3-4 is here labeled a *Sequential Merger* of four vortices.

Meanwhile, vortices 5 and 6 have paired, inducing the rollup of vortex C on the wall (frames d and e); also vortices 7 and 8 have paired, inducing the rollup of vortex D on the wall (frames f and g). Then the pair 5-6 merges with pair 7-8, forcing wall vortices C-D to merge (frames h and i). Finally, the large-scale structure 5-6-7-8 interacts with structure C-D, causing it to explode off the wall (frames i and j). These structures (5-6-7-8 and C-D) then interact to form the second pair of a von Karman-type vortex street (frames k and l) which passes off the grid. The creation of the large-scale structure 5-6-7-8 is here labeled a *Paired Merger* of four vortices.

This *Paired Merger* process is repeated creating large-scale structures 9-10-11-12 and E-F which form the third pair of a von Karman-type vortex street (frames o and p) that passes of the grid.

This is followed by a *Sequential Merger* of vortices 13,14,15 and 16 (frames l through p) and the creation of the wall structure

4. *Preliminary calculations used a Tanh(y) profile with an inflection point off the wall in place of a Pollhausen profile. These results also showed that the free shear layer became unstable first. Hence, the results were insensitive to the profile used for the wall shear layer.

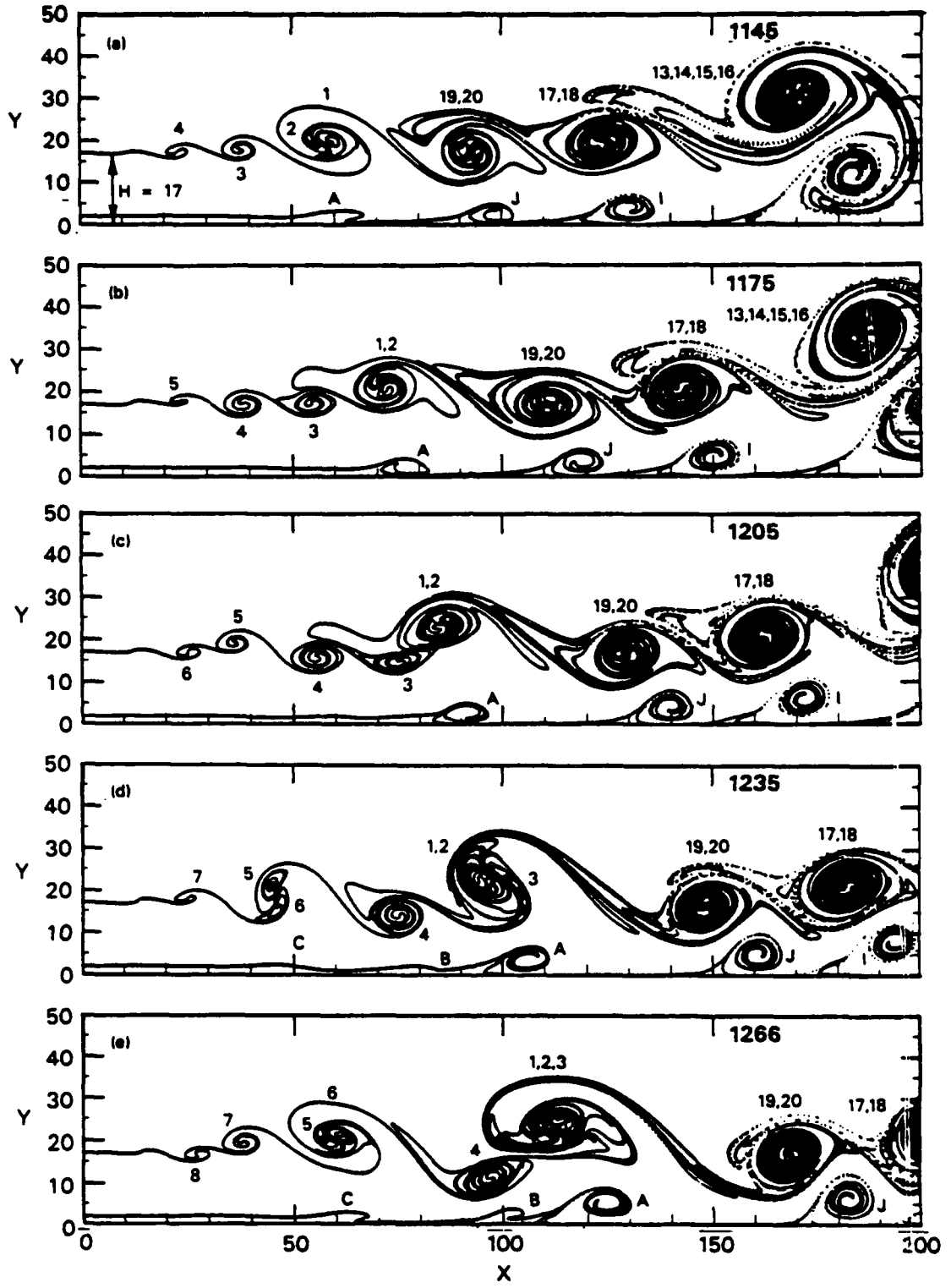

Figure 20. Numerical simulation of a wall jet (λ = -1, r = ∞, λ_p = 0). The figures depict the evolution of the material interfaces over one period of the flow. Vortices forming on the free shear layer are labeled sequentially with cardinal numbers, while those forming on the wall layer are denoted by capital letters.

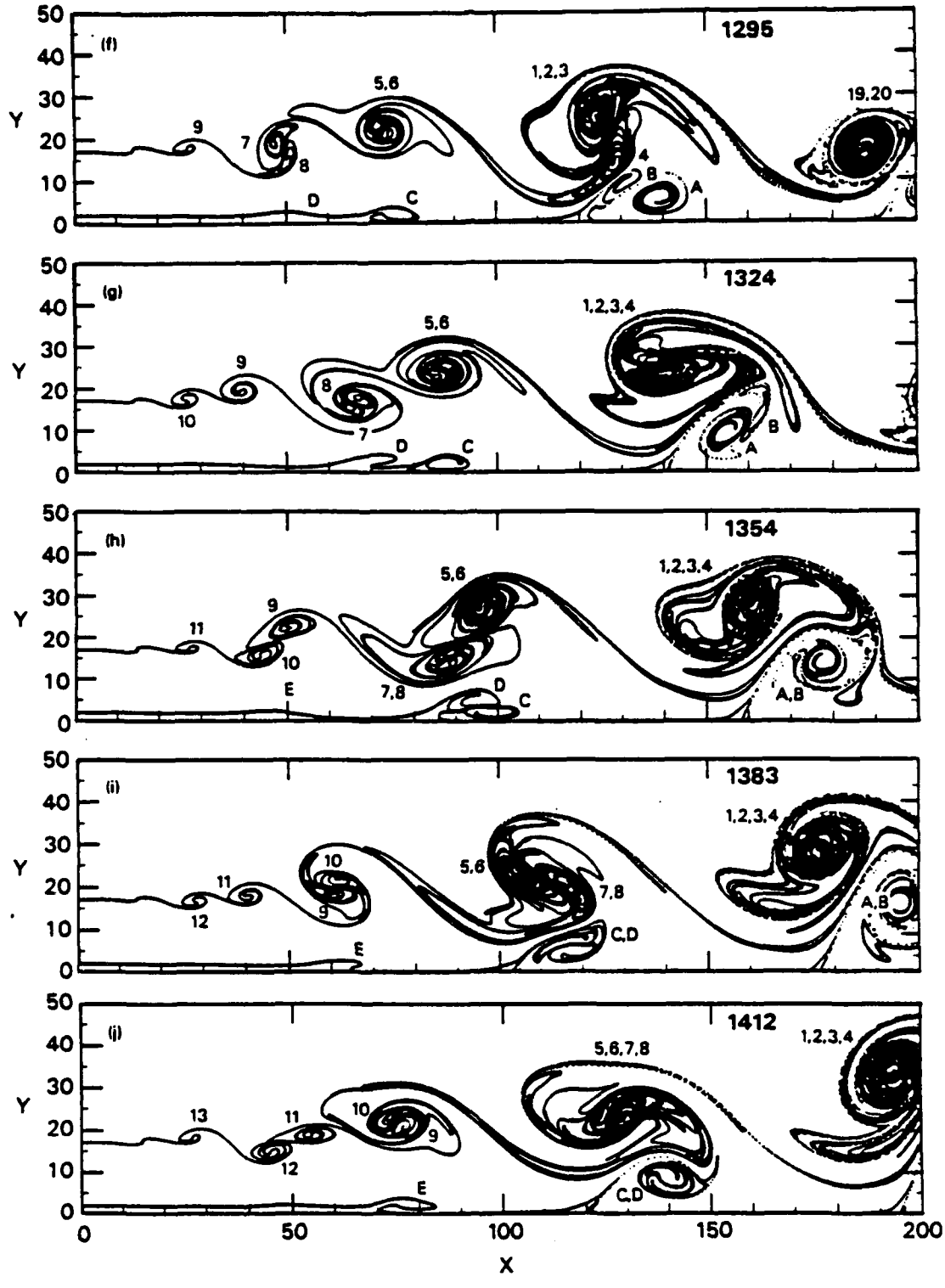

Figure 20. Numerical simulation of a wall jet ($\lambda = -1$, $r \to \infty$, $\lambda_\rho = 0$). The figures depict the evolution of the material interfaces over one period of the flow. Vortices forming on the free shear layer are labeled sequentially with cardinal numbers, while those forming on the wall layer are denoted by capital letters (Continued).

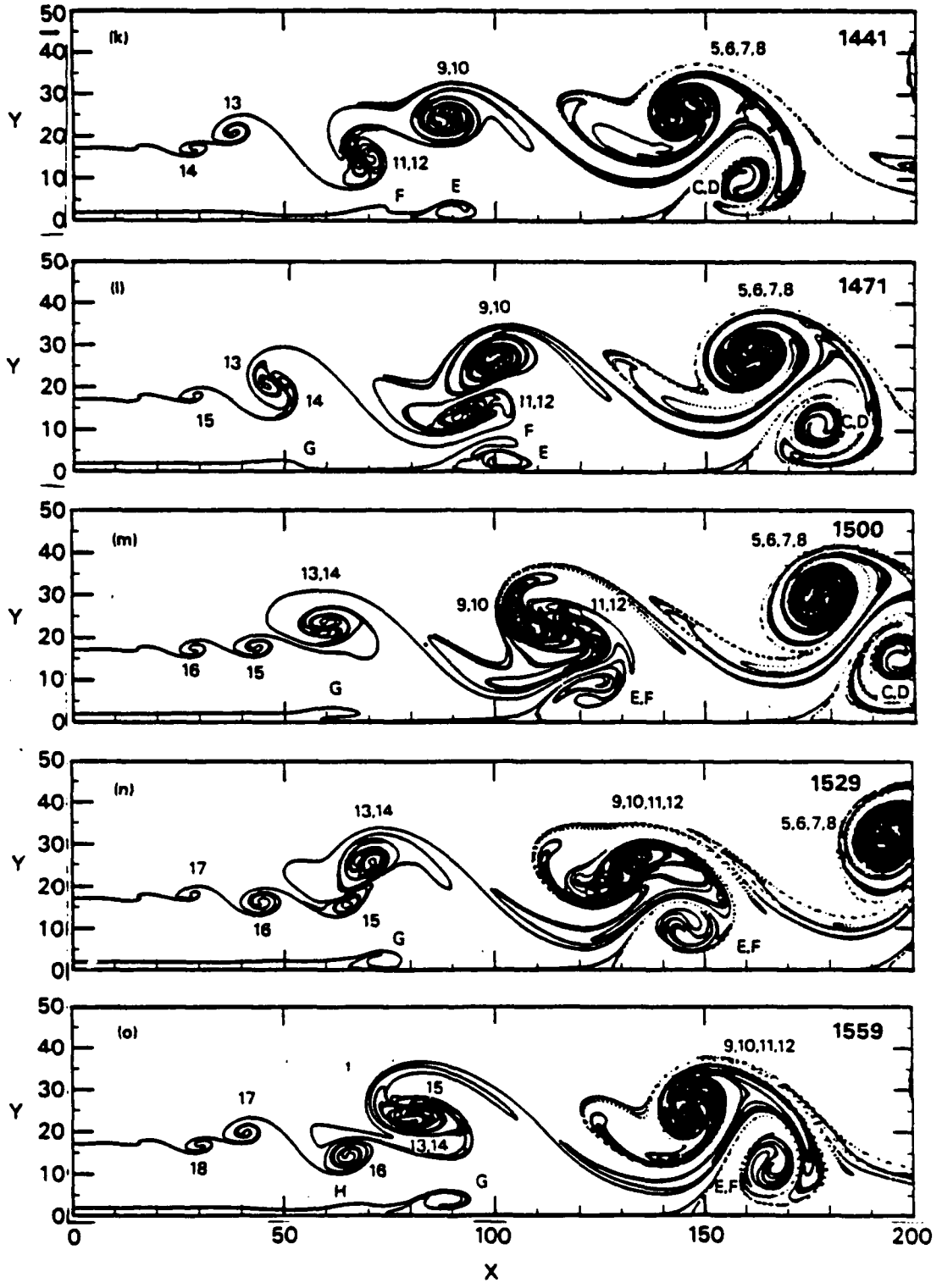

Figure 20. Numerical simulation of a wall jet (λ = -1, r = ∞, λ_ρ = 0). The figures depict the evolution of the material interfaces over one period of the flow. Vortices forming on the free shear layer are labeled sequentially with cardinal numbers, while those forming on the wall layer are denoted by capital letters (Continued).

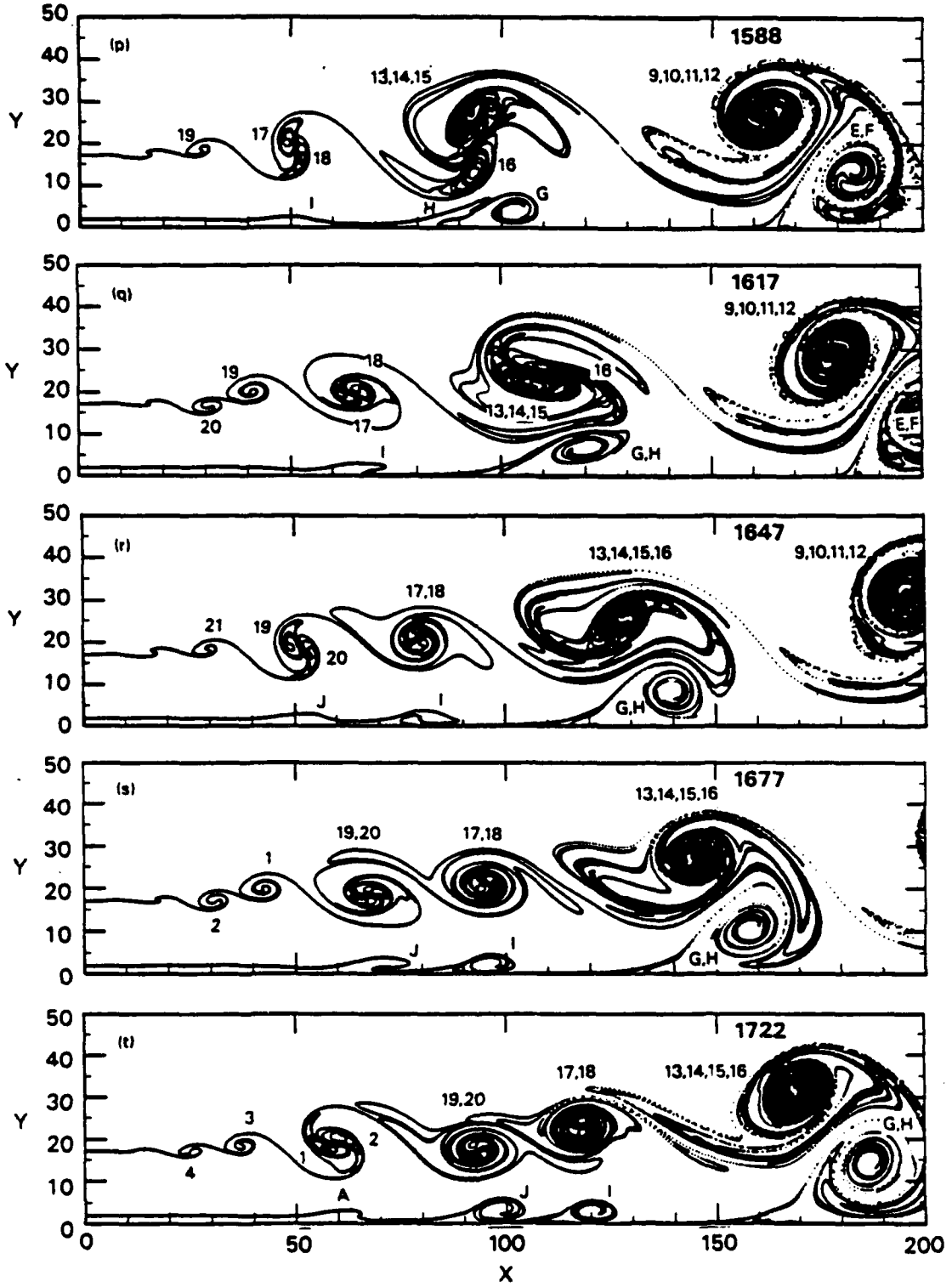

Figure 20. Numerical simulation of a wall jet (λ = -1, r = ∞, λ_0 = 0). The figures depict the evolution of the material interfaces over one period of the flow. Vortices forming on the free shear layer are labeled sequentially with cardinal numbers, while those forming on the wall layer are denoted by capital letters (Concluded).

G-H. These structures interact to form the fourth pair of a von Karman vortex street (frames s and t) that passes off the grid.

Meanwhile, vortices 17 and 18 have paired (frames p and q) creating wall vortex I; vortices 19 and 20 have paired (frames r and s) creating wall vortex J; and vortices 1 and 2 have paired (frame t) creating wall vortex A. Note that the interface shape in frame (t) is essentially identical to that of frame (a). Hence, the whole process is then repeated. Also note that the vortex pair 17-18 and the pair 19-20 pass off the grid without merging (frames a through f).

In summary, the vortex merging on the free shear layer of the wall jet follows this sequence:

- 1 *Sequential Merger* (1-2-3-4)
- 1 *Paired Merger* (5-6-7-8)
- 1 *Paired Merger* (9-10-11-12)
- 1 *Sequential Merger* (13-14-15-16)
- 1 *Pairing* (17-18)
- 1 *Pairing* (19-20)

and then the sequence repeats. The *Sequential Mergers* correspond to a Mode IV response, while the *Paired Mergers* correspond to two Mode II responses followed by a Mode IV response. Evidently the higher modes did not directly couple into the dynamics for these flow lengths.

Figure 21 depicts the flow field contours corresponding to the last frame of Figure 20. The vorticity on the free shear layer rapidly accumulates into the large structures as a result of the first pairing of vortices, and thus, the braid regions are essentially devoid of vorticity. A low pressure region is formed in the center of each vortex structure due to the rotational flow, while a recompression is created in the braid region between structures. The vorticity in the wall shear layer accumulates but it remains near the wall until the wall vortex structures are entrained into the von Karman vortex street.

The flow field time-histories were monitored at stations x = 85 and 170 (corresponding to 5H and 10H). These were integrated in time over the last 4000 cycles of the calculation (with about 8 large-scale structures passing station 170). The resulting mean velocity profiles are presented in Figure 21. The results have been scaled by the jet thickness δ_J (where $\bar{u} = 0.5\ \bar{u}_{max}$):

$$\eta_J = y/\delta_J \qquad (47)$$

where δ_J = 17, 21.7 and 31.2 for x = 0, 85 and 170, respectively. Figure 22 demonstrates that the mean velocity $\bar{u}$ profiles at x = 85 and 170 are considerably different than the inflow profile (shown as a solid curve). The peak value of $\bar{u}$ decays with distance, indicating that the streamwise momentum is spread laterally due to large-scale mixing. The shear layer portion of the profiles ($0.5 < \eta_J$) at the two stations collapses quite well with this scaling. The wall layer portion of the u profiles ($\eta_J < 0.5$) is significantly modified by the vortex structures of the free shear layer. By x = 170, a separated flow profile has developed. The large-scale structures induce a mean transverse velocity $\bar{v}$ across the entire width of the grid.

Figure 23 presents the fluctuating flow profiles (corresponding to Figure 22), while the peak values are listed in Table 1. The streamwise velocity fluctuations peak near the wall (η_J = 0.2) and near the free shear layer (η_J = 0.75), similar to the results of Bajura and Catalano (1975). The calculated

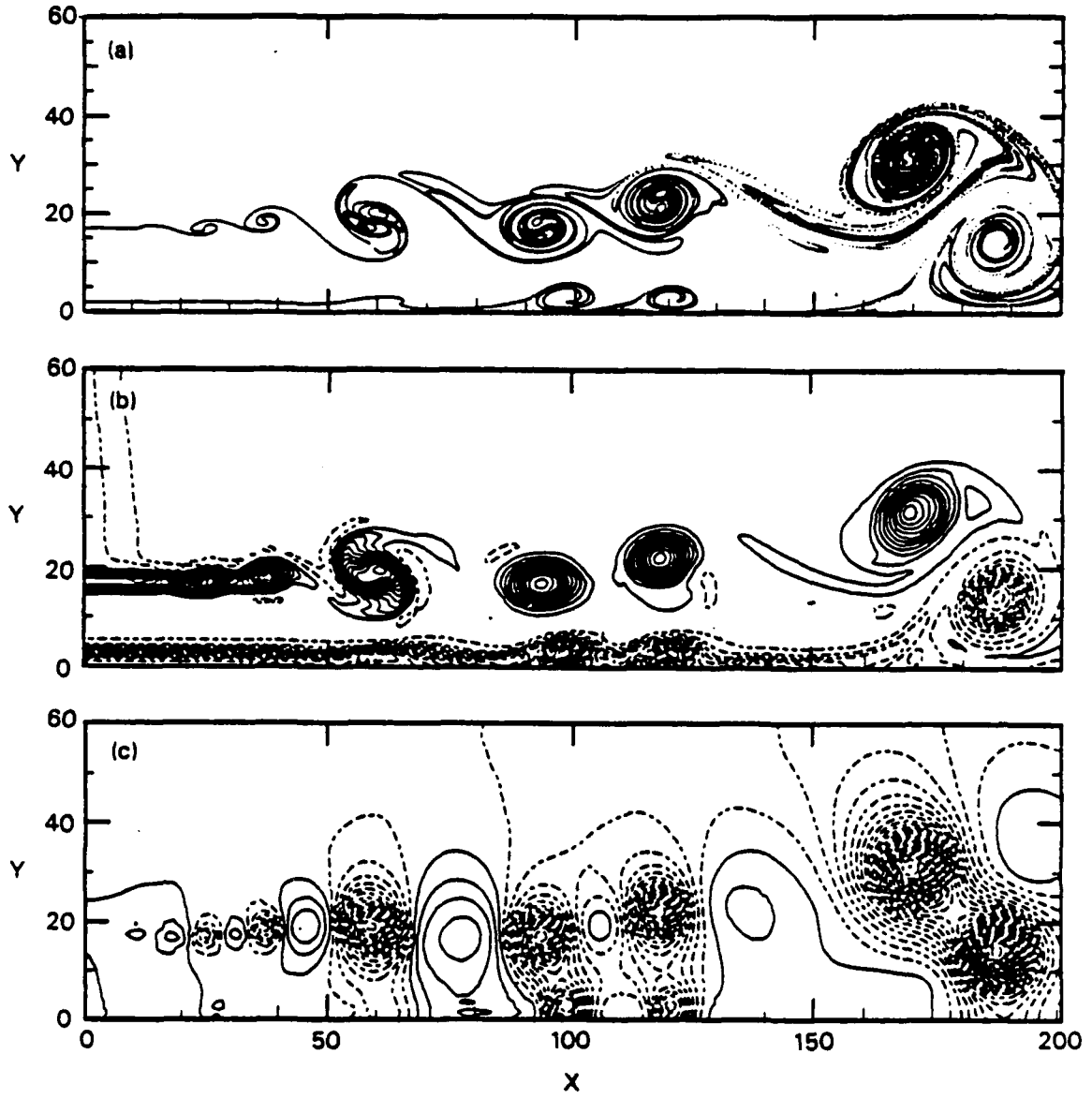

Figure 21. Flow field of the wall jet calculation at t = 1722: (a) material interfaces; (b) vorticity contours (solid lines correspond to positive values, while dashed lines denote negative values); (c) overpressure contours (solid lines correspond to positive values).

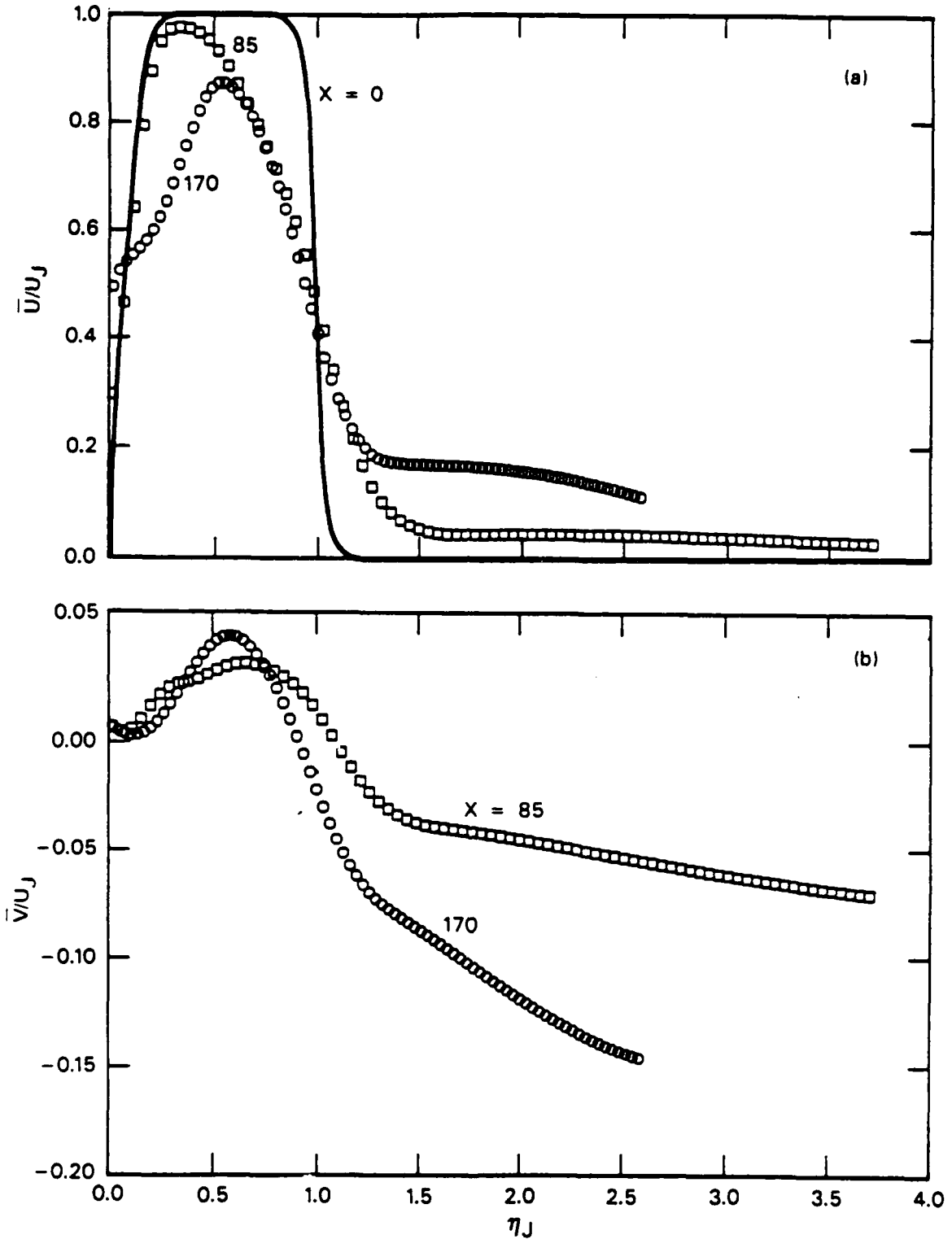

Figure 22. Mean-flow velocity profiles of the wall jet calculation: (a) streamwise component; (b) transverse component. (Symbols □ and ○ denote stations at x = 85 and 170, respectively).

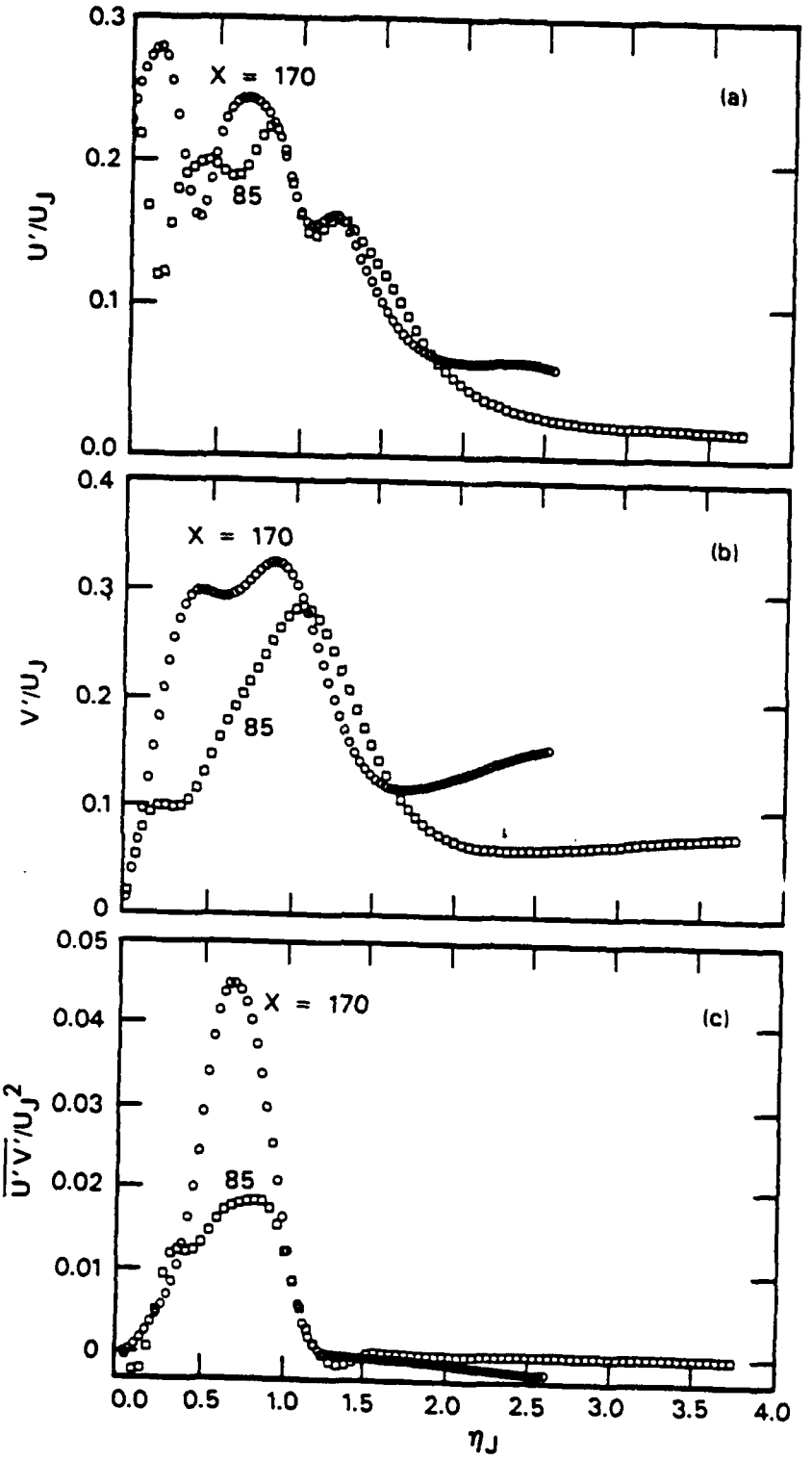

Figure 23. Time-averaged fluctuating flow profiles from the wall jet calculation: (a) streamwise velocity; (b) transverse velocity; (c) shear stress. (Symbols □ and ○ denote stations at x = 85 and 170, respectively.).

peaks, however, are an order of magnitude larger than the data, presumably due to the much larger shear used in the calculation. (Their experiments had an exit Reynolds number of only 445.) The transverse velocity fluctuations also have two peaks, one at $\eta_J = 0.5$ and the other at $\eta_J = 1$, at the last station. The fluctuating shear stresses are positive and have a single peak at $\eta_J = 0.75$, indicating that the structures on the shear layer are controlling the mixing process.

5.3 SUMMARY.

The dynamics of the wall jet was considerably different than the previously described cases. The free shear layer on top of the jet reacted first by forming discrete vortex structures which paired and merged. The merging patterns consisted of both paired and sequential merging of four vortices, corresponding to both Mode II-type and Mode IV-type response — even though the first ten subharmonics were used to perturb the jet.

The merging was faster than in the spreading shear layer calculation because of the larger absolute shear and it was smoother and more periodic because the uniform density assumption of the wall jet calculation virtually eliminated any baroclinic generation of vorticity. Vortex pairing on the free shear layer triggered instabilities in the wall shear layer which rolled up into a vortex directly underneath each large structure on the free shear layer. Merging of these latter structures caused the wall vortices to merge. In the final stage of interactions, the large-scale structures from the two shear layers paired, forming a von Karman-type vortex street. In this way, fluid from the wall layer of the jet was mixed across the free shear layer, and vice versa. In effect, the rotational structures on the free shear layer caused the wall layer to periodically explode off the wall, thus creating a separated flow profile. These results are qualitatively similar to the wall jet experiments of Bajura and Catalano (1975). Peak velocity fluctuations, however, are larger in this calculation because of the faster merging and larger absolute shear.

SECTION 6

CONCLUSIONS AND GENERALIZATIONS

The present inviscid calculations seem to duplicate quite well the major flow features that have been observed in experiments. These include the formation and growth of large rotational structures, the visual spreading rates, and the mean-flow profiles. Presumably, these features are dominated by two-dimensional effects. The fluctuating components of the flow agree qualitatively with the available experimental data, however, peak fluctuations such as u' or v' can be 1.5 to 2 times larger than the data because of the two-dimensional flow approximation.

It is now clear that the fluctuating, time-dependent flow variations associated with these "steady" shear layer problems are caused by the dynamic evolution of unstable shear layers. By taking into account one more degree of freedom (time) in these "steady" shear layer calculations, one can determine not only the mean flow but also the fluctuating flow field without any turbulence modeling. Since the present calculations are in good agreement with the available experimental data, we conclude that the evolution of these unstable shear layers is dominated by inviscid flow effects. The calculations also point out the importance of accurately evaluating the convective derivatives. Viscous forces and molecular diffusion are too small (relative to convective effects) to significantly affect the dynamics of such large-Reynolds-number flows. Molecular effects are then relegated to the relatively minor role of de-singularizing the inviscid problem by spreading the shear over a small but finite volume of fluid, and they create additional vorticity at wall boundaries.

In fact, molecular transport effects such as fluid diffusivity and viscosity are inherently diffusional effects. They correspond to fluctuations on a molecular scale, but on a macroscopic scale they can only produce smoothing — that is, they can never by themselves create the self-organized behavior such as the large-scale rotational structures presented here. Consequently, the macroscopic fluctuations of the flow are caused exclusively by inviscid, convective flow effects — that is, by the nonlinear dynamics of unstable shear layers.

The calculations presented here show that the fluid-dynamic response of three fundamentally different shear layers is quite similar in that they roll up into large-scale rotational structures which grow by interactions and merging. There are five features which these shear layers have in common, namely:

1. The flows contain an initial tangential velocity change (i.e., a shear layer).
2. The initial shear layer thickness is non-zero (i.e., the problem is desingularized).
3. The velocity profiles are unstable to infinitesimal perturbations.
4. Perturbations exist in the flow (either from external sources, or from internal sources such as the growth of molecular fluctuations).
5. The Reynolds number of the flows are large (i.e., the convective flow velocities are orders of magnitude larger than any molecular diffusion velocities).

These five common features seem to be responsible for the development of the organized rotational structures in these (and probably other) shear layers.

Successful numerical simulations of such fluctuating flows have numerical requirements which parallel the above features, namely:

1. They contain the correct amount of circulation, by means of initial and boundary conditions.

2. The initial shear layer is resolved on the computational mesh.

3. The initial velocity profile contains an inflection point, hence the flow is unstable.

4. The shear layers are perturbed with a spectrum of frequencies.

5. The numerical Reynolds number of the finite difference solution is large so that convective flow effects are accurately evaluated (i.e., the algorithm is nondiffusive enough to allow the instabilities to grow, and not be artificially damped by numerical diffusion).

Accurate numerical simulations have two additional requirements:

6. The calculations must be at least two-dimensional and time dependent, even for problems which are steady in the mean or time-averaged sense.

7. The computational grid must be fine enough to resolve the rotational structures.

Feature 6 implies a direct numerical simulation of the conservation equations, without modeling the fluctuating flow components. Fortunately, feature 7 can be satisfied because these structures are large and can be resolved on computational grids that are orders of magnitude coarser than those needed to resolve molecular transport effects.

Shear layers occurring in most practical applications will experience three-dimensional perturbations, and eventually the fluctuating kinetic energy will be shared over all of these dimensions. Hence, the principal limitation of the present calculations is the two-dimensional flow approximation.

Nevertheless, the present large-Reynolds-number approach (i.e., the direct solution of the conservation laws of gas dynamics) offers one technique for extending the numerical simulations of fluctuating shear layers to the nonsteady, compressible flow regime. Such numerical solutions are valuable for at least three reasons: (1) they provide idealized solutions against which to compare real flows; (2) the problem parameters (e.g., initial and boundary conditions) can be controlled more easily than in experiments; (3) the flow field can be sampled nonintrusively and easily analyzed. Such comparisons between idealized calculations and experimental data cannot help but increase our understanding of the fluid dynamics of such complex flows.

In closing, it should be pointed out that the organized structures of the shear layer flows presented here can be viewed as noteworthy examples of self-organized response of nonequilibrium systems as described by Nicolis and Prigogine (1977) and Prigogine (1980). Whereas low-Reynolds-number shear layers smooth out tangential velocity discontinuities by molecular diffusion, large-Reynolds-number

shear layers remove the velocity nonequilibrium by forming large-scale rotational structures. The initial and boundary conditions of the problem (i.e., shear flow) place the system in a state corresponding to the nonlinear range of nonequilibrium dynamics. The system is unstable, and the flow evolves to a new, more stable state which is considerably more complex yet self-organized.

SECTION 7

LIST OF REFERENCES

Ashurst, W.T., Turbulent Shear Flows I (1979) ed. by F. Durst, et al., Springer-Verlag, Berlin, pp. 402-413.

Bajura, R.A., and Catalano, M.R. (1975) Transition in a Two-Dimensional Plane Wall Jet. *J. Fluid Mech.*, Vol. 70, pp. 773-799.

Bergh, H. (1958) A Method for Visualizing Periodic Boundary Layer Phenomena, *IUTAM Symposium "Boundary Layer Research,"* Ed. by H. Gortler, Berlin, pp. 173-178.

Brown, G.L. and Roshko, A. (1974) On Density Effects and Large Structure in Turbulent Mixing Layers, *J. Fluid Mech.*, Vol. 64, 775-816.

Chien, K.Y., Ferguson, R.E., Collins, J.P., Glaz, H.M., Kuhl, A.L., (1987) A Study of Mixing in Forced Shear Layers with an Euler Code, *AIAA* 87-1318.

Chorin, A.J. (1973) Numerical Studies of Slightly Viscous Flow, *J. Fluid Mech.* 57, pp. 785-796.

Chorin, A.J. (1986) Vortex Methods for the Study of Turbulent Combustion at a Low Mach Number. *10th Int. Colloq. on the Dynamics of Explosions and Reactive Systems. Prog. in Astronautics and Aeronautics* Vol. 105, 14-21.

Colella, P. and Glaz, H.M. (1985) Efficient Solution Algorithms for the Riemann Problem for Real Gases, *J. Fluid Mech.* 59(2), 264-289.

Colella, P. Ferguson, R.E., Glaz, H.M., Kuhl, A.L. (1985) Mach Reflection from an HE-Driven Blast Wave. *Dynamics of Explosions, Prog. Astro. and Aero.* Vol. 106; Bowen, Leyer and Soloukhin, editors, pp. 388-421.

Coles, D.E. (1956) The Law of the Wake in the Turbulent Boundary, *J. Fluid Mech.* Vol. 1, pp. 191-226.

Coles, D.E. (1969) A Young Persons Guide to the Data, *Proceedings, Computation of Turbulent Boundary Layers-1968.* AFOSR-IFP Stanford Conference, Vol. 2 compiled data. Edited by D.E. Coles and E.A. Hirst, Stanford Univ. Press, Stanford, California, p. 3.

Corcos, G.M. and Sherman, F.S. (1984) The Mixing Layer: Deterministic Models of a Turbulent Flow. Part 1. Introduction and the Two-Dimensional Flow: *J. of Fluid Mech.*, Vol. 139, pp. 29-65.

Davis, R.W. and Moore, E.F. (1985) A Numerical Study of Vortex Merging in Mixing Layers. *Physics of Fluids*, Vol. 28, pp. 1626-1635.

Gad-el-Hak, M., Blackwelder, R.F., Riley, J.J. (1984) On the Interaction of Compliant Coatings with Boundary Layer Flows. *J. Fluid Mech.*, Vol 140, pp. 257-280.

Ghoniem, A., Chorin, A., Oppenheim, A.K. (1982) Numerical Modeling of Turbulent Flow in a Combustion Tunnel, *Philos. Trans. R. Soc. London, Ser. A 304*, pp. 303-325.

Glaz, H.M., Colella, P., Glas, I.I. and Deschambault, R.L. (1985) A Numeri-

cal Study of Oblique Shock-Wave Reflections with Experimental Comparisons. *Proc. Royal Soc. London, Ser. A.*, Vol. 398, pp. 117-140.

Glowacki, W.J., Kuhl, A.L., Glaz, H.M. and Ferguson, R.E. (1986) *Shock Waves and Shock Tubes*, ed. by D. Bershader and R. Hanson, Stanford University Press, Stanford, CA, pp. 187-194.

Grinstein, F.F., Oran, E.S., Boris, J.P. (1986) Numerical Simulations of Asymmetric Mixing in Planar Shear Layers, *J. Fluid Mech.* Vol. 165, 201-220.

Ho, C.M. and Huang, L.S. (1982) Subharmonics and Vortex Merging in Mixing Layers. *J. Fluid Mech.* Vol. 119, 443-473.

Inoue, O. (1985) Vortex Simulation of a Turbulent Mixing Layer, *AIAA Journal*, Vol. 23, pp. 367-373.

Inoue, O. (1987) 3D Vortex Simulation of a Plane Mixing Layer. *6th Symp. on Turbulent Shear Flows*, Toulouse, France.

Klebanoff, P.S. (1955) Characteristics of Turbulence in a Boundary Layer with Zero Pressure Gradient. NACA Report 1247.

Konrad, J.H. (1977) *An Experimental Investigation of Mixing in Two-Dimensional Turbulent Shear Flows with Applications to Diffusion-Limited Chemical Reactions*, Ph.D. Thesis, California Institute of Technology, Pasadena, California.

Kuhl, A.L., Colella, P., Berger, M., Glaz, H.M., Ferguson, R.E., (1987) Unstable Wall Jet Evolution for a Double-Mach Stem Flow, *ICDERS-11*.

Laufer, J. (1950) Some Recent Measurements in a 2-Dimensional Turbulent Channel Turbulent Channel. *J. Aeronaut. Sci.*, Vol. 17, pp. 277-287.

Leonard, A. (1980) Vortex Methods for Flow Simulation. *J. Comp. Phys.* Vol. 37, pp. 289-335.

Martin, W.A. (1958), An Experimental Study of the Turbulent Boundary Layer Behind the Initial Shock Wave in a Shock Tube. *J. Aerospace Science*, Vol. 25, pp. 644-652.

McInville, R.M., Gatski, T.B., Hassan, H.A. (1985), "Analysis of Large Vortical Structures in Shear Layers." *AIAA* Vol. 23, pp. 1165-1171.

Michel, F. (1932) *Larm und Resonanzschwingungen im Kraftwerksbetriels* (Noise and Resonant Vibrations in Power Plants). Berlin VDI-Verlag. (from L. Prandtl's *private library*).

Mirels, H. (1956) Boundary Layer Behind Shock or Thin Expansion Wave Moving into Stationary Fluid, NACA TN 3712.

Monkewitz, P.A. and Huerre, P. (1982) Influence of the Velocity Ratio on the Spatial Instability of Mixing Layers. *Phys. of Fluids* Vol. 25, 1137-1143.

Nicolis, G. and Prigogine, I., (1977) *Self Organization in Nonequilibrium Systems* (From Dissipative Structures to Order through Fluctuations), Wiley, New York.

Oppenheim, A.K. (1986) The Beauty of Combustion Fields and Their Aerothermodynamic Significance. *10th Int. Colloq. on the Dynamics of Explosions and Reactive Systems. Prog. in Astronautics and Aeronautics* Vol. 105, 3-13.

Owen, F.K., Horstman, C.C., Kussoy, M.I. (1975) Mean and Fluctuating Flow

Measurements of a Fully-Developed, Non-Adiabatic, Hypersonic Boundary Layer. *J. Fluid Mech.* Vol. 70, pp. 393-413.

Oster, D. Wygnanski (1982). The Forced Mixing Layer Between Parallel Streams, *J.Fluid Mech.*, Vol. 123, p. 91-130.

Prandtl, L. (1933) Neuere Ergebnisse der Turbulenzforschung. Z. VDI 77, pp. 105-114.

Prigogine, I., (1980) *From Being to Becoming* (Time and Complexity in the Physical Sciences), Freeman, New York.

Rayleigh, Lord, Robert John Strutt (1887). On the Stability Instability of Certain Fluid Motions. II. Scientific Paper Vol. III, No. 144, p. 17-23. (Originally from the Proceedings of the London Mathematical Society, Vol. 19, pp. 67-74.)

Reichenbach, H. (1987) Ernst Mach Institut, Freiburg, Germany, (private communication).

Riley, J.J. and Metcalfe, R.W. (1980) *AIAA Paper No.* 80-0274.

Schlichting, H. (1968) *Boundary Layer Theory*, McGraw-Hill, New York, N.Y., p. 445.

Schubauer, G.B. and Spangenberg, W.G. (1960) Forced Mixing in Boundary Layers, *J. Fluid Mech. 8*, pp. 10-32.

Schultz-Grunow, F. (1938) Der Hydraulische Reibungswiderstand von Platten mit mabig rauher Oberflache, insbesondere von Schiffsoberflachen. *Schiffbautech. Ges. Jahrb.*, Vol. 39, pp. 176-198.

Spina, E.F., Smits, A.J. (1987) Organized Structures in a Compressible Turbulent Boundary Layer. *J. Fluid Mech.* Vol. 182, pp. 85-109.

Tollmien, W. (1935) Ein allgemeines Kriterium der Instabilitat laminarer Geschwindigkeits-verteilungen. Nachr. Ges. Wiss. Gottingen, Math. Pys. Klasse, Fachgruppe I, 1, 79-114; see also in NACA TM 792 (1936).

Van Dyke, M. (1982) *An Album of Fluid Motion*. Parabolic Press, Stanford, California.

White, F.M. (1974) *Viscous Fluid Flow*, McGraw-Hill, N.Y. p. 480.

Wieghardt, K., Tillmann, W. (1944) Zur turbulenten Reibungs-schicht bei Druckansteig, ZWB.KWI. U and M 6617, trans. On the Turbulent Friction Layer for Rising Pressure. NACA TM 1314 (1951).

DISTRIBUTION LIST

DNA-TR-89-6

DEPARTMENT OF DEFENSE

AFSOUTH
ATTN: U S DOCUMENTS OFFICER

ASSISTANT TO THE SECRETARY OF DEFENSE
ATOMIC ENERGY
ATTN: EXECUTIVE ASSISTANT

DEFENSE INTELLIGENCE AGENCY
ATTN: DB-6E
ATTN: RTS
ATTN: RTS-2B

DEFENSE NUCLEAR AGENCY
ATTN: OPNS
ATTN: SPWE
4 CYS ATTN: TITL

DEFENSE NUCLEAR AGENCY
ATTN: TDNM
2 CYS ATTN: TDTT W SUMMA

DEFENSE TECHNICAL INFORMATION CENTER
2 CYS ATTN: DTIC/FDAB

FIELD COMMAND DEFENSE NUCLEAR AGENCY
ATTN: FCPR
ATTN: FCT COL J BOYCE

JOINT STRAT TGT PLANNING STAFF
ATTN: JKC (ATTN: DNA REP)
ATTN: JKCS, STUKMILLER

THE JOINT STAFF
ATTN: J-5 NUCLEAR & CHEMICAL DIV

UNDER SECRETARY OF DEFENSE
ATTN: J THOMPSON
ATTN: STRAT & THEATER NUC FORCE

DEPARTMENT OF THE ARMY

DEP CH OF STAFF FOR OPS & PLANS
ATTN: DAMO-NCZ

HARRY DIAMOND LABORATORIES
ATTN: SLCHD-NW-TS

U S ARMY MATERIAL TECHNOLOGY LABORATORY
ATTN: DRXMR-HH

U S ARMY MATERIEL COMMAND
ATTN: AMCCN

U S ARMY STRATEGIC DEFENSE CMD
ATTN: CSSD-H-SA

U S ARMY STRATEGIC DEFENSE COMMAND
ATTN: ATC-D (WATTS)

DEPARTMENT OF THE NAVY

NAVAL RESEARCH LABORATORY
ATTN: CODE 2627 (TECH LIB)
ATTN: CODE 4040 D BOOK

NAVAL SEA SYSTEMS COMMAND
ATTN: SEA-0351

NAVAL SURFACE WARFARE CENTER
ATTN: CODE K82

OFC OF THE DEPUTY CHIEF OF NAVAL OPS
ATTN: OP 654

DEPARTMENT OF THE AIR FORCE

AIR UNIVERSITY LIBRARY
ATTN: AUL-LSE

BALLISTIC SYSTEMS DIVISION
ATTN: CC
ATTN: CV
ATTN: ENSR
ATTN: MGET

STRATEGIC AIR COMMAND/XRFS
ATTN: XRFS

WEAPONS LABORATORY
ATTN: NTED J RENICK
ATTN: NTED R HENNY
ATTN: NTEDA
ATTN: NTES
ATTN: SUL

WRIGHT RESEARCH & DEVELOPMENT CENTER
ATTN: AFWAL/MLP
ATTN: AFWAL/MLTM

DEPARTMENT OF ENERGY

LAWRENCE LIVERMORE NATIONAL LAB
ATTN: D BURTON
ATTN: J CAROTHERS
ATTN: G GOUDREAU
ATTN: S SACKETT
ATTN: H KRUGER
ATTN: P CHRZANOWSKI

LOS ALAMOS NATIONAL LABORATORY
ATTN: M T SANDFORD
ATTN: R WHITAKER

SANDIA NATIONAL LABORATORIES
ATTN: A CHABAI DIV 9311
ATTN: D J RIGALI
ATTN: R G CLEM

OTHER GOVERNMENT

CENTRAL INTELLIGENCE AGENCY
ATTN: OSWR/NED

DEPARTMENT OF THE INTERIOR
ATTN: D RUDDY

DEPARTMENT OF DEFENSE CONTRACTORS

ACUREX CORP
ATTN: C WOLF

AEROSPACE CORP
ATTN: H MIRELS

APPLIED RESEARCH ASSOCIATES, INC
ATTN: C J HIGGINS

APPLIED RESEARCH ASSOCIATES, INC
ATTN: S BLOUIN

BDM CORPORATION
ATTN: J MERRITT

CALIFORNIA RESEARCH & TECHNOLOGY, INC
ATTN: M ROSENBLATT

CALIFORNIA RESEARCH & TECHNOLOGY, INC
ATTN: J THOMSEN

INFORMATION SCIENCE, INC
ATTN: W DUDZIAK

KAMAN SCIENCES CORP
ATTN: L MENTE
ATTN: R RUETENIK

KAMAN SCIENCES CORP
ATTN: DASIAC

KAMAN SCIENCES CORPORATION
ATTN: DASIAC

MAXWELL LABORATORIES, INC
ATTN: J MURPHY

PACIFIC-SIERRA RESEARCH CORP
ATTN: H BRODE

R & D ASSOCIATES
2 CYS ATTN: A KUHL
ATTN: C K B LEE
2 CYS ATTN: H M GLAZ
ATTN: J LEWIS
2 CYS ATTN: K Y CHIEN
2 CYS ATTN: P COLELLA
ATTN: P RAUSCH
2 CYS ATTN: R E FERGUSON
ATTN: T MAZZOLA

R & D ASSOCIATES
ATTN: P MOSTELLER

R & D ASSOCIATES
ATTN: J WALTON

S-CUBED
ATTN: A WILSON

SCIENCE APPLICATIONS INTL CORP
ATTN: H WILSON

SCIENCE APPLICATIONS INTL CORP
ATTN: R WESTERFELDT

SCIENCE APPLICATIONS INTL CORP
ATTN: J COCKAYNE
ATTN: W LAYSON

SCIENCE APPLICATIONS INTL CORP
ATTN: G BINNINGER

TRW SPACE & DEFENSE SYSTEMS
ATTN: D M LAYTON
ATTN: OUT6/W WAMPLER

VITRO CORP
ATTN: H BRIGHT

WEIDLINGER ASSOCIATES, INC
ATTN: P WEIDLINGER

DIRECTORY OF OTHER

MARYLAND UNIVERSITY OF
ATTN: H GLAZ MATH DEPT